UNIVERSITA' DEGLI STUDI DI MILANO-BICOCCA

Facoltà di Scienze Matematiche, Fisiche e Naturali
Department of Material Science
PhD School in Nanostructures and Nanotechnologies
XXV Cycle

Polymer Nanocomposites for Illumination: Toward Warm White Light

Supervisor: Prof. Roberto SIMONUTTI

PhD Coordinator: Prof. Gianfranco PACCHIONI

PhD thesis of:

Luca De Trizio

Academic Year 2011-2012

A Claudia,

che il tuo ricordo possa correre per sempre con noi!

My heart leaps up when I behold
A rainbow in the sky:
So was it when my life began,
So is it now I am a man,
So be it when I shall grow old
Or let me die!
The Child is father of the Man:
And I could wish my days to be
Bound each to each by natural piety.

(William Wordsworth)

Index

Chapter 1: Introduction

Chapter 2: Colloidal Shynthesis of Nanocrystals

Chapter 3: Characterization of Nanocrystals

Chapter 4: *Warm White Light* Project

Chapter 5: Indium Phosphide/Zinc Sulfide (InP/ZnS) Core-Shell QDs

Chapter 6: Size-tunable, hexagonal plate-like Cu_3P and Janus-like Cu-Cu_3P nanocrystals

Chapter 7: Strongly Fluorescent Quaternary Cu-In-Zn-S Quantum Dots

Introduction

1.1 Motivations

Nanoscience has emerged replacing the "old" science of bulk materials and becoming one of the most exciting areas of research today. For the last 30 years, the synthesis of crystals with sizes ranging from few to hundred nanometers has been intensively developed both for scientific interest and for their many technological applications. There are at least two major reasons why the nanomaterials are extremely important: the significant fraction of atoms on the surface of nanocrystals, as compared to that found in the corresponding bulk materials, and the restriction of charge carriers into a very small volume. For these reasons, in the nanometer size regime new mesoscopic phenomena characteristic of this intermediate state of matter, found in neither bulk nor molecular systems, develop. NCs melt at much lower temperatures than those required for bulk systems and can be easily obtained in crystalline phases that are often forbidden in the bulk. In semiconductors, once an extremely small size is reached, quantum confinement can lead to a widening of the band gap and of the level spacing at the band edges. In noble metals, the decrease in size below the electron mean free path leads to localized surface plasmon absorption that originates from the collective oscillations of the free electrons on the particle surface. Finally, magnetic NCs behave as single magnetic domains whose magnetization can be easily influenced by thermal fluctuations of the local environment, depending on the particle size and on a variety of surface effects.

Since the material properties can be finely tuned by varying the size and shape, a high control over the synthesis of such systems is of key importance to fully exploit the potential of those systems. There are two different approaches to create nanocrystals: the top-down physical processes and the bottom-up chemical methods. The physical processes can produce large quantities of nanocrystals, whereas the synthesis of uniformly sized nanocrystals and their size-control are very difficult to achieve. On the other hand, colloidal chemical synthetic methods can be used to synthesize uniform nanocrystals with a controlled particle size. Furthermore, various shaped nanocrystals can be synthesized by varying the reaction conditions. In devising the synthetic schemes for nanocrystals, we have to consider two aspects: the synthetic chemistry and the formation kinetics of nanocrystals. Needless to say, they are closely related to one another, making it hard to establish a general synthetic method that is widely applicable to various materials.

Recent efforts have been directed toward the fabrication of polymer nanocomposites containing nanometric sized crystals because their potential application as high technology materials. In nanocomposites, the organic polymer can not only stabilize the NCs in a solid matrix, but also sums the peculiar features of organic and inorganic components. In this way the optical and mechanical properties of the polymers are combined with the specific features of the NCs. The solid matrices retain their shapes and the polymeric nanocomposites can be processed into thin films or bulk sheets, and can be stretched or oriented opening new perspectives to a number of original applications. The incorporation of optically active materials such as NCs into polymers has found multitude of applications in optical amplification, photovoltaic, photodetection, sensing, and plasmonics. For example, the incorporation of fluorescent semiconductor NCs within a bulk polymer structure has lead to high performing nanocomposites for illumination. [1-4, 12]

1.2 Nanocrystals

Nanocrystals constitute a major class of nanomaterials. Nanocrystals are zero-dimensional crystalline systems, possessing nanometric dimensions that can vary from one to hundreds nanometers. Small nanocrystals of a few nanometers exhibit unusual features that are different from those of their bulk counterpart. Large nanocrystals (>20-50nm), on the other hand, would have properties similar

to those of the bulk. The size-dependent properties of nanocrystals include electronic, optical, magnetic and chemical characteristics. There are basically two types of size-dependent effects: smoothly scalable ones which are related to the fraction of atoms at the surface, and quantum effects which show discontinuous behaviour due to completion of shells in systems with delocalized electrons. [2,5]

1.3 Surface Effects in Nanocrystals

The dimensions of nanocrystals are so small that an unusually high fraction of the total atoms would be present on their surfaces [2]. The fraction of atoms at the surface is called dispersion F, and it scales with surface area divided by volume. The size dependence of dispersion is illustrated in figure 1.1 for cubic structures. A cube has n atoms along an edge and a total of $N = n^3$ atoms, where the number of atoms at the surface is 6n corrected for double counts at the 12 edges and for reinstalling the 8 corners. For large N the edge and corner corrections become negligible:

$$F = \frac{6n^2 - 12n + 8}{n^3} = \frac{6}{N^{1/3}}\left(1 - \frac{2}{N^{1/3}} + \frac{8}{6N^{2/3}}\right) \approx \frac{6}{N^{1/3}}$$

Atoms at the surface have fewer direct neighbours than atoms in the bulk. Therefore, particles with a large fraction of atoms at the surface have a low mean coordination number.

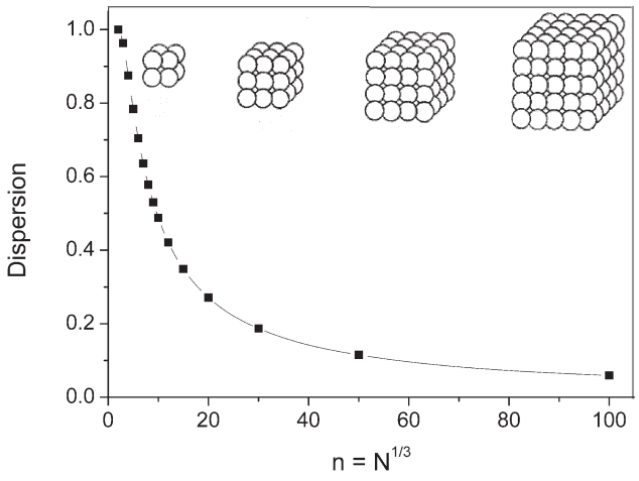

Figure 1.1 Plot of the dispersion as a function of n for cubic clusters. The schematic illustration of the first four clusters is represented too.[5]

We see that the fraction of surface atoms becomes less than 10% (F<0.1) only when the total number of atoms is more than of the order of 10^6 which for a typical metal would correspond to a crystal diameter >100 nm. Atoms at the surface have fewer direct neighbors than atoms in the bulk. For this reason the atoms at the surface have a lower cohesive energy and hence a low stabilization. The lower stabilization of atoms or molecules at the surface leads to a lower melting point of surface layers. This has been known since 1871 when W. Thomson described how the melting point, T_m, of a particle depends on its radius, r, as:

$$\frac{T_m - T_m^*}{T_m} = -\frac{2V_m(l)\gamma_{sl}}{r\Delta H_m}$$

where T^*_m is the melting temperature of the bulk material, $V_m(l)$ is the molar volume of the liquid phase, γ_{sl} is the interfacial tension between the solid and the liquid phases and ΔH_m is the bulk latent heat of melting. Moreover, the latent heat of melting shows a size-scaling behavior similar to that of the melting point, and some experiments have also determined a significant size dependence of the interfacial tension. As an example the melting point of 2.5 nm gold particles was reported to be about 930 K, much lower than its bulk value of 1336 K and even lower than the value calculated from the Thomson's equation. [5]

1.4 Quantum Confinement

To better understand the potentialities of a nanoscale material it's necessary, at first, to comprehend how the properties of such a material are modified confining its crystalline structure in one, two or three dimensions as it happens in nanocrystalline materials [6]. In fact, if we think about the electronic structure of nanocrystals, for example, this is something intermediate between the discrete energy levels of an atomic system and the band structure of the bulk material, as depicted in figure 1.2.

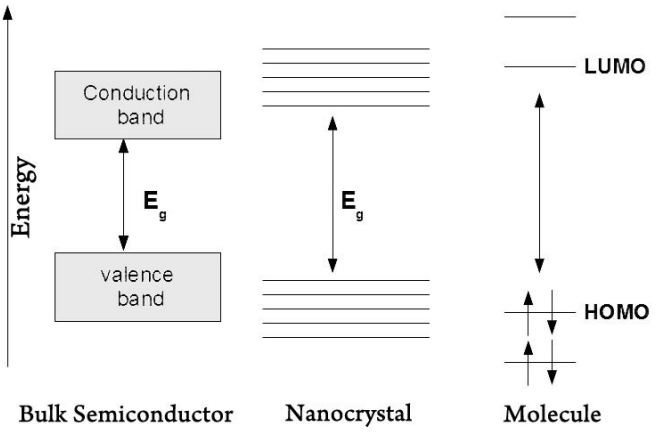

Figure 1.2 Schematic representation of the energy levels in a bulk semiconductor, a nanocrystal with quantum confinement and in a molecule.

To predict and understand such changes in the electronic structures of a nanoscale material, quantum mechanics is a very powerful tool. In the case of a bulk material with size d_x, d_y and d_z the electrons can be considered, as a first approximation, free non interacting carriers moving in 3 dimensions. Due to the analogy with gas molecules the model is often referred as "free electron gas". In this model the energy of a single electron with mass m and velocity $\bar{v} = (v_x, v_y, v_z)$ can be described just with its kinetic energy $E = \frac{1}{2} m\bar{v}^2$. The wavevector $\bar{k}$ linked to the momentum $\bar{p}$ through the relation $\bar{p} = m\bar{v} = \frac{h}{2\pi}\bar{k}$, where h is the Plank constant, is commonly used to refer to the electron's states. The wavelength λ associated with an electron in the solid is directly calculable from the wavenumber $|\bar{k}| = \frac{2\pi}{\lambda}$. To calculate the energy levels in a bulk material we can imagine it as if it was an infinite solid ($d_x = d_y = d_z \rightarrow \infty$). In this approximation, the solutions of the Schröedinger equation for the electrons can be written as a product of three independent functions (one for each dimension x, y and z) $\Psi(x,y,z) = \Psi(x)\,\Psi(y)\,\Psi(z) \propto e^{ik_x x} e^{ik_y y} e^{ik_z z}$ and $k_{x,y,z} = \pm n \frac{2\pi}{d_{x,y,z}}$ where n is an integer number. Each possible level $\bar{k}$ can be occupied by two electrons (Pauli's exclusion principle) with opposite spin ($m_s = \pm\frac{1}{2}$) up to the highest energy level that at 0K is called Fermi energy E_F ($\propto k_F^2$). Since the possible energy states in k-space are spaced by $\Delta_k = \pm n \frac{2\pi}{d_{x,y,z}}$ and $d_x = d_y = d_z \rightarrow \infty$ we can imagine the electrons in the bulk material filling quasi-continuously the sphere of states of radius k_F (at 0K).

Defining D(k) the density of k states per unit of wavenumbers we can directly calculate the number of electrons N(k) whose state is included between k and $k+\Delta_k$. In the k space we can visualize the states from k to $k+\Delta_k$ as a spherical shell of radius k and thickness Δ_k which volume is therefore proportional to $k^2\Delta_k$. In approximation of infinite solid ($\Delta_k \to 0$) the density of state can be then expressed as: $D(k) = \frac{d\,N(k)}{dk} \propto k^2$. Converting from k to E ($E \propto k^2$) we are finally able to define the density of states in a bulk material as $D(E) \propto \sqrt{E}$. So in approximation of infinite material and free electron gas the energy levels are found to be quasi-continuous and the density of states is proportional to $\sqrt{E}$ (see figure 1.3a)

The situation changes when the solid we are considering is not infinite anymore along the three dimensions x, y and z. If we consider, in fact, a material which dimensions along x and y are infinite and d_z is just few nanometers (an "infinite sheet"), its electrons will be able to move along the xy plane as free electrons but the possible energy states along the z direction will be limited due to quantum confinement effects. To clarify this concept we can model the behavior of the electrons along the z axis as particles in a box of infinite potential. The solutions of the Schröedinger equation are in this case standing waves $\Psi(z) \propto \sin(k_z z)$ with $k_z = \frac{n\pi}{d_z}$ where n is a integer number. While in the x-y plane the energy levels are still quasi-continuous, since d_z is not infinite anymore, the possible electron states along the z direction are now quantized and their spacing is inversely proportional to the thickness of the material. For such a system the calculated density of state in k space is found to be $D(k) \propto k$ and, therefore $D(E) \propto 1$.

The density of states in a 2D material can be described as a step function where for a given n_z (each step) the energy levels are found to be quasi-continuous (so they don't depend on E anymore). It's easily understandable that the reduction of one dimension of a solid produces a drastic change of the electronic structure of the material itself (see figure 1.3b)

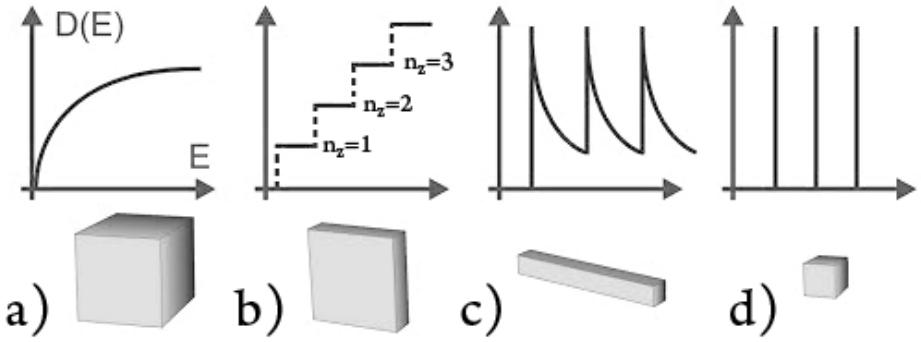

Figure 1.3 Figure x. Density of states for an electron gas in a bulk material (3D) (a), infinite sheet (2D) (b), quantum-wire (1D) (c) and quantum-dot (0D) (d).

Shrinking our imaginary solid along a second direction (y for instance) we obtain a so called quantum-wire, a system in which the electrons are free to move along just one direction (x) and constrained along the other two. Again the electron will have a quasi-continuum distribution of states along the x axis while quantized states along y and z. The density of states in k space is found to be $D(k) \propto 1$ and, therefore $D(E) \propto \frac{1}{\sqrt{E}}$ (figure 1.3c). For each given k_z and k_y we have a hyperbole containing a quasi-continuous distribution of k_z states.

At last, confining a solid along all the three dimensions produces systems that are normally called quantum dots (QD). In these structures the electrons are confined in all the directions and so the possible k states allowed are discrete. The density of states therefore appears as delta-peaks for the allowed energy levels (figure 1.3d).

1.5 Colloids

To speak about colloidal NCs we have first to introduce colloidal systems. Colloids consist of at least two phases and the dimension of the dispersed phase, consisting of particles, is typically submicroscopic down to the nanometetric scale [7]. The particle size is similar to the range of the repulsive or attractive forces existing among them. When we look at a colloidal solution at the microscope (when possible) we can observe that the particles move around in a random way, called *Brownian motion* (figure 1.4).

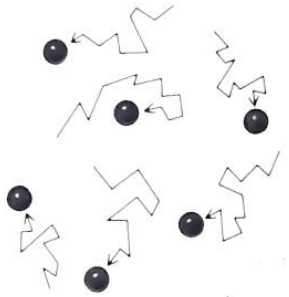

Figure 1.4 Figure x: Sketch of the random Brownian motion of colloidal particles.

The cause of this motion is due to the molecules forming the suspending liquid ("solvent"). All of the molecules are in random or thermal motion so that at any given instant the local concentration of a small volume element of the fluid will be either higher or lower than the mean concentration. The thermal motion of the colloidal particles tends, in general, to the direction of the lower molecular densities. Since the molecules move randomly so do the colloidal particles and their velocity is governed by the hydrodynamic drag. Since the diffusion tends to move the particles from high concentration zones to low concentration ones, if we have a high concentration of particles then there will be a directional drift away from this region. If we consider now a sphere, the so called Stokes drag factor, s_v, can be written as function of the radius of the sphere, R, and the viscosity of the fluid, η :

$$s_v = 6\pi\eta R$$

Since the motion is random we can write the net velocity, v, as the average distance moved x in the time t: $v=x/t$. The work done in moving the particle is simply the hydrodynamic force $f_v=vs_v$ multiplied by the average displacement x. Since this work is made possible only thanks to the thermal energy that is k_BT, where k_B is the Boltzman constant and T is the absolute temperature we can write:

$$k_B T = x v f_v$$

With a simple substitution we can express the self diffusion coefficient, D_s, as:

$$D_s = \frac{x^2}{t} = \frac{k_B T}{6\pi\eta R}$$

This is the Stokes-Einstein equation for the diffusion coefficient that is fundamental for many analysis of colloidal systems. We can also derive a characteristic timescale for this diffusive motion if we, for example, calculate the time a particle takes to move a distance equal to its radius:

$$t = \frac{6\pi\eta R^3}{k_B T}$$

That is known as the Einstein-Smoluchowski equation. For an isolated particle of 1μm in water a 20°C it takes about 0.5 sec to diffuse of one radius. The presence of other particles, in concentrated systems, introduces specific interactions as hydrodynamic, electrostatic or van der Waals' forces that slow down the diffusive motions.

Depending on the phase or the nature of the species forming the colloidal solution several kind of different colloidal dispersions can be distinguished (see table 1.1):

		Dispersed Medium		
		Gas	**Liquid**	**Solid**
Continuous Medium	**Gas**	/	Liquid Aerosol *(mist)*	Solid aerosol *(smoke)*
	Liquid	Foam *(shampoo)*	Emulsion *(mayonnaise)*	Sol *(ink)*
	Solid	Solid Foam *(packaging)*	Gel *(butter)*	Solid sol *(stained glass)*

Table 1.1 Types of colloidal dispersions. Some examples are reported in brakets.

Depending upon how different substances forming colloidal solution acquire the size of particles, colloidal solutions may be classified into the following three categories: (a) Multimolecular colloids, (b) Macromolecular colloids and (c) Associated colloids. When a large number of atoms or small molecules (having diameters of less than 1nm) of a substance combine together in a dispersion medium to form aggregates having size in the colloidal range, the colloidal solutions thus formed are called multimolecular colloids. The species (atoms or molecules) constituting the dispersed particles in multimolecular colloids are normally held together by Vander Waals' forces. . Certain substances form large molecules whose dimensions are comparable to those of colloidal particles. Such

molecules have very high molecular masses and are termed as macromolecules (as polymers). When such substances are dispersed in suitable dispersion medium, the resulting colloidal solutions are known as macromolecular colloids. Thus, in macromolecular colloids, the dispersed particles are themselves large molecules having very high molecular masses. Lastly, associated colloids are formed by aggregated particles made of amphiphilic molecules. The aggregated particles are also called micelles. The associated colloids are usually formed by surfactants (surface active agents) like soaps and synthetic detergents. These agents form micelles when present in solution at a concentration greater than critical micellization concentration (CMC).

1.6 Interactions in Colloidal Solutions

1.6.1. Intermolecular Attraction

The origin of the attraction between colloidal particles originates from weak interactions that are often referred to as van der Waals interactions. To describe such attractive forces one has to take into account several interactions that can occur which are electrodynamics in origin. These can be described separating them in three distinct forms. [7]

Molecules having a strong permanent dipole moment exhibit dipole-dipole interactions also called *Keesom interactions*. We can write the interaction free energy at the distance r, $u(r)_K$ as:

$$u(r)_K = -\frac{C_K}{r^6}$$

where C_K is a constant that depends on the molecules considered. For example two identical molecule of dipole μ have $C_K \propto \mu^4$.

The interaction between a polar molecule and a non polar one is called *Debye interaction*. The polar molecule can polarize the electron cloud of the non polar molecule. The interaction between the original dipole and the induced one can be described in a similar way to the dipole-dipole one. In this case the polarizability of the non polar molecule is a key feature. The Debye interaction free energy $u(r)_D$ can be written:

$$u(r)_D = -\frac{C_D}{r^6}$$

Where the constant C_D for a system consisting in two different molecules "1" and "2" has the following dependence: $C_D \propto (\alpha_1\mu_1^2+\alpha_2\mu_2^2)$.

The attraction between two non polar molecules, at last, is described by the *London or Dispersion interactions*. It is originated by the movement of the electron cloud around the atomic nucleus resulting in a dipole fluctuation. When two atoms get close the temporary dipoles become aligned to minimize the interaction energy. The free energy of this kind of interaction $u(r)_L$ can be expressed as:

$$u(r)_L = -\frac{C_L}{r^6}$$

where C_L is the London constant, that, for two similar atoms, is proportional to the ionization energy of the outer electrons, $h\nu_I$, where h is the Plank constant, and the polarizability, α, as follows:

$$C_L \propto h\left(\frac{\nu_{I1}\nu_{I2}}{\nu_{I1}+\nu_{I2}}\right)\alpha_1\alpha_2$$

This kind of interaction has a particular importance because it's much stronger than the Keesom of Debye contributions in nearly all cases of colloidal materials (for the exception of water based systems).

Similarly to small molecules, nanocrystals dispersed in solution are subjected to two major types of attractive forces: van der Waals and dipolar interactions. In the absence of the dipolar interactions, large isotropic van der Waals interactions induce formation of spherical aggregates. For weak van der Waals interactions, the strength of the dipolar moments controls the formation of chain-like structures. Chain-like structures have been directly observed experimentally. The influence of the van der Waals, dipolar and also nanocrystal–substrate interactions on the nanocrystals organization at a mesoscopic scale is a key issue, not only for practical applications but also for fundamental understanding.

1.6.2. **Steric Repulsion**

In colloidal synthesis the surfactants adsorbed on the surface of inorganic nanocrystals prevent the aggregation of the system by keeping the surfaces apart. For this to be effective, the molecules must be not only strongly bound to the surface of the NCs but also extended into the solution so that the surfaces cannot approach too closely, and this gives the term "steric interaction". Let's consider two crystals completely covered by many layers of surfactants. As the surfaces of the two approach, the outer molecules interpenetrate resulting in an increase of the free energy. At closer approach a further decrease in entropy (and so the free energy increases) occurs due to the "compression" of the organic chains, that is, there are even fewer possible configurations available to each molecule. Anyways this extreme case is not occurring when considering good steric stabilizers as we shall see that the repulsion becomes very large before such close approach is attained. [7]

For colloidal nanocrystals we can imagine their surface as covered by a uniform layer of surfactants. This layer has a constant concentration profile with a short-range reducing profile due to the variation in chain length. The steric interaction is zero until the outer "organic shell" of one particle comes into contact with that of an adjacent particle (the organic chains start to mix). The concentration of chains is thus higher in the overlap volume resulting in an osmotic pressure that tends to separate the particles. If the thickness of the organic layer is δ, the interaction occurs when the particle surfaces are at distances $<2\delta$. If the separation becomes $<\delta$, a second effect has to be modeled. The surface of the second particle further restricts the possible chain conformations of the surfactants, giving rise to an additional contribution to the interaction energy. This volume restriction term won't be taken into account since this "extreme" overlap of layers doesn't normally occur as only a small degree of overlap is sufficient to produce potentials much greater than k_BT. In figure 1.5, the overlap between adsorbed layers of thickness δ, uniform concentration, c, and surface-to-surface separation, h, is depicted for two different geometries.

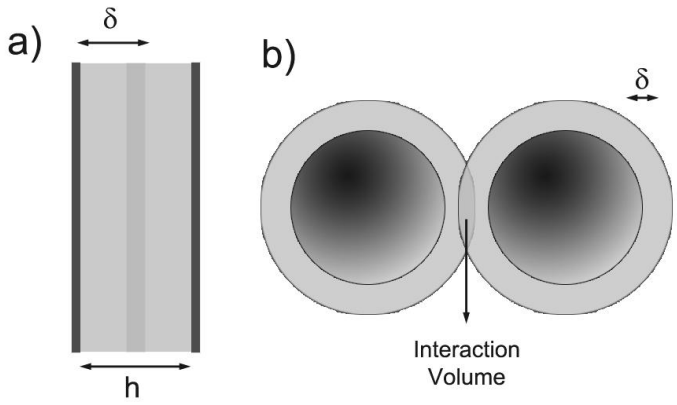

Figure 1.5 Schematic representation the steric interaction between two approaching a) plates and b) particles surrounded by an organic layer of thickness δ.

In the interaction volume the total concentration is two times higher (2c) and so the corresponding osmotic pressure, P_E, will tend to separate the particles. In order to calculate interaction energy, V_S, it's necessary to integrate the repulsion force (that is equal to the pressure multiplied for the area, A, of interaction) over the distance between the particles:

$$V_S = \int_{2\delta}^{h} -P_E A \, dx$$

The integration of the area over the distance x gives the interaction volume that we can call v_0. The Flory-Huggins model of polymers in solution gives us the osmotic pressure of a polymer solution as a function of its concentration:

$$P = \left(\frac{RTc}{M} + BRTc^2 + \cdots\right)$$

Where M is the number average molecular weight of the polymer and B is the second virial coefficient:

$$B = \left(\frac{\bar{v}_2}{M}\right)^2 \frac{1}{\bar{v}_1}(0.5 - \chi)$$

Where v is the molar volume, "1" and "2" referring to the solvent and polymer species, respectively and χ is the "Flory-Huggings interaction parameter". This last term represents the variation of internal energy, U, per segment on mixing divided for the thermal energy as:

$$\chi = \frac{\Delta U z}{k_B T}$$

Where z is the coordination number for the lattice contacts. We can now write the interaction energy as:

$$V_s = -(2v_0 P_{x=2\delta} - v_0 P_{x=h})$$

And so:

$$V_s = \left\{\left[\frac{RT2c}{M} + RTB(2c)^2\right] - 2\left(\frac{RTc}{M} + RTBc^2\right)\right\} v_0$$

Which gives:

$$V_s = 2RTBc^2 v_0$$

$$V_s = \frac{2RT}{\overline{v_1}}\left(\frac{c\overline{v_2}}{M}\right)^2 (0.5 - \chi) v_0$$

The overlap volume, v_0, in the geometries considered can be written:

Plate-plate $v_0 = 2\delta - H$

Sphere-sphere $v_0 = \frac{2\pi}{3}(\delta - H/2)^2(3a + 2\delta + H/2)$

What we can extract from these equations is that the interaction energy has a strong dependence on the temperature, concentration of surfactants and there is an increase in repulsion as the separation decreases. The biggest problem in calculating the repulsion energy relies in a detailed description of the concentration profile in the early overlap regime. This is the point at which polydispersity of surfactants is really controlling the softness of the interaction.

1.7 Colloidal Nanocrystals

1.7.1. Introduction

Colloidal NCs a specific kind of NCs that are chemically synthesized in a liquid solution containing some stabilizing organic molecules, broadly termed as surfactants. As extracted from their growing medium, they are typically made of a

crystalline core with the desired chemical composition and a monolayer surface shell of tightly coordinated surfactants that provide them with solubility and, hence, with colloidal stability. Without the ligands the particles would tend to aggregate forming bulky aggregates that flocculate or settle down in the medium. Depending on the dispersion medium, the ligands stabilize the solutions in two different ways, as we will discuss more deeply later on. Generally, in an polar solvent coulomb interactions between charged ligand species provide a repulsive force to counter the attractive van der Waals force between the nanocrystals (see figure 1.6a). In an organic medium, the steric repulsion of ligands attached to the surfaces of the NCs provides the necessary repulsive force (see figure 1.6b). These particles are chemically robust and thus amenable to be further processed after the synthesis to achieve disparate purposes, such as their integration with existing devices, or their incorporation into biological environments without substantial loss of the original properties. [2-3]

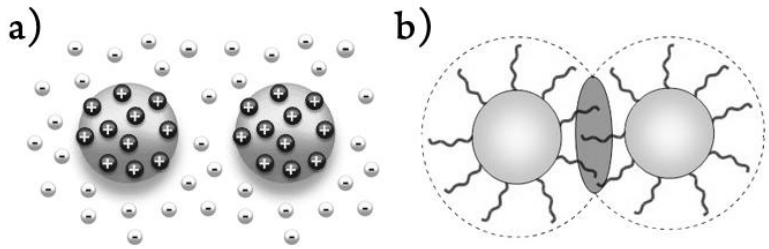

Figure 1.6 Schematic illustration of a) charge and b) sterically stabilized nanocrystals in colloidal solution.

1.7.2. Semiconductor Nanocrystals: Quantum Dots

Colloidal nanocrystals with a semiconductor as the inorganic material are commonly called quantum dots (QD). If the size of the NCs is smaller than the Bohr radius of the corresponding bulk exciton, the electronic excitations are strongly confined in all the three dimensions. The photoexcitation of such a system creates an electron-hole pair that is confined to and delocalized over the volume of the NC. Each carrier can be treated as a particle in a sphere bound at the NC surface by an infinite potential. So, the electron and the hole can be described by hydrogenic wavefunctions and occupy discrete electronic energy levels. For this reason quantum dots are often referred to as "artificial atoms". Three-dimensional confinement effects collapse the continuous density of states of the bulk solid into the discrete electronic states of the NC. The finite size of the NC quantizes the allowed k values: decreasing the NC diameter the separation between the permitted energy states increases. In other words the quantum

confinement modifies the band structure producing a widening of the band gap (E_g) that is inversely proportional to the size of the nanostructures (see fig 1.7). [3, 6, 11]

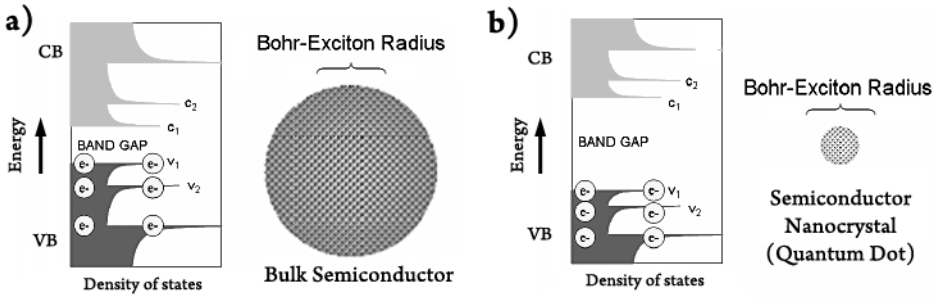

Figure 1.7 Schematic representation of the effect of quantum confinement in quantum dots. Valence (VB) and conductance (CB) bands are blue and red, respectively. Energy levels in a) a bulk semiconductor crystal and b) a quantum dot (of the same chemical composition). Lowering the size of a semiconductor the band structure is modified and the resulting bandgap widens.

The optical and electrical properties, that are intimately connected to the electronic structure of the material, are therefore modified too. In fact, since the energy to create an electron-hole pair (that is equal to E_g) rises as an effect of the confinement, the corresponding absorption edge of the material shifts to higher energies (blue-shift). The photo excited electron-hole pairs (also called excitons) have a finite time before recombining inside the material. One way for the system to relax is to emit a photon, thus losing its energy (another method would be the loss of heat energy); in this case the radiative decay is called photoluminescence (PL). The excitons normally lose some energy (in a non radiative way) before relaxing to the ground state, so the emitted photons have less energy than the absorbed one: this energy difference is the Stokes shift. In colloidal systems one has also to consider that the absorption and the PL of the sample depend on the size of the QDs in the solution: the larger is the size distribution the wider is the PL peak. As a result the position and the width of the PL peak of a colloidal solution of QDs can be used to estimate the polydispersity and mean size of the nanocrystals.

An important parameter that characterizes these systems is called quantum efficiency or quantum yield (QY). The fluorescence QY is defined as the ratio of the number of photons emitted to the number of photons absorbed. It is normally expressed as a percentage, the higher is the QY the more efficient these QDs are in terms of fluorescence.

1.7.3. **Core-Shell QDs**

The nanometric crystal size of QDs results in a very high surface/volume ratio. That's why QDs typically exhibit surface related trap states acting as fast non-radiative de-excitation channels for photogenerated excitons, thereby reducing the fluorescence quantum yield. An important strategy to passivate QDs' surface is the overgrowth of a shell of a second semiconductor. In this way, the fluorescence efficiency and the stability to photo-oxidation of various types of semiconductor NCs have seen significant improvement. [8]

Depending on the electronic levels and the bandgaps of the core-shell semiconductors, the shell can have different functions in CS NCs. In function of the band alignments of the bulk materials (which are mostly used in NC synthesis) three configurations can be distinguished: type-I, type-II and reverse type-I (figure 1.8).

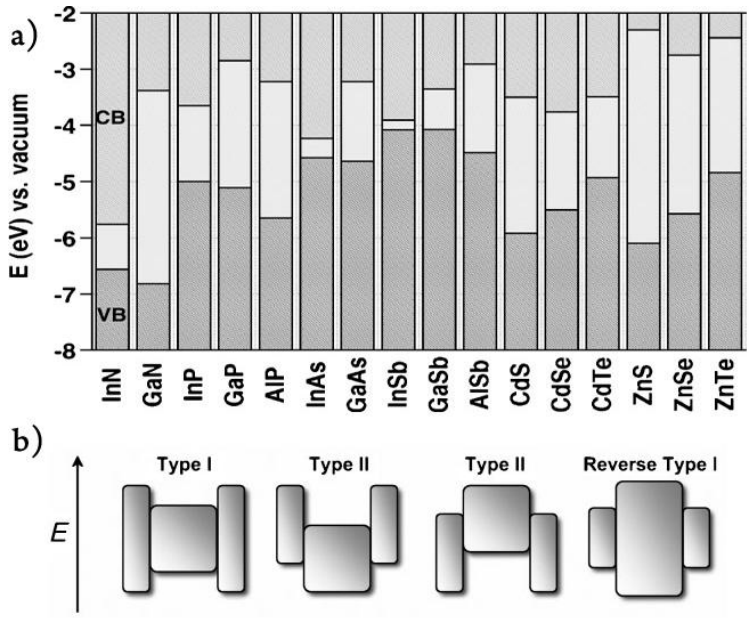

Figure 1.8 a) Energy levels of the mostly used III–V and II–VI semiconductors (VB: valence band, CB: conduction band). b) Representation of the possible bandgap alignment in different core-shell systems. The upper and lower edges of the rectangles correspond to the positions of the conduction- and valence-band edge of the core (center) and shell materials, respectively.[8]

In type-I core-shell systems the bandgap of the shell material is larger than that of the core, so that the photoexcited excitons are confined in the core. In reverse type-I alignment, the bandgap of the shell material is smaller than that of the core and, depending of the thickness of the shell, the holes and electrons are

partially or completely confined in the shell. Finally in type-II heterostructures, the valence band offset or the conduction band inset of the shell is located in the bandgap of the core. Upon excitation of the NC the electron-hole couple is spatially separated in different regions of the composite structure. In type-I CS NCs, the shell is used to passivate the surface of the core with the goal to improve its photoluminescence. The shell acts as a barrier between the surface of the optically active core from its surrounding medium. Consequently, the sensitivity of the optical properties to changes in the local environment of the NCs' surface, induced, for example, by the presence of oxygen or water molecules, is reduced. Moreover core-shell systems, compared to bare NCs, exhibit enhanced stability against photodegradation. At the same time, the shell growth reduces the number of surface defects, which can act as trap states for charge carriers and thereby reduce the fluorescence QY.

In reverse type-I systems, a material with a smaller bandgap is grown onto the core (with higher bandgap) so that, upon excitation, the charge carriers formed are partially delocalized in the shell. In these systems the emission wavelength can be tuned controlling the shell's thickness. The resistance against photobleaching and the fluorescence QY of these systems can be improved by growing a second shell of a larger-bandgap semiconductor on the core/shell NCs.

In type-II systems, the emission wavelength of the overall NC is significant red-shifted in respect to the core itself. The staggered band alignment, in fact, leads to a smaller effective bandgap than each one of the constituting semiconducting materials. The interest of these systems is the possibility to manipulate the emission through the shell thickness towards spectral ranges, which are normally difficult to obtain with just one material. Due to the smaller energy transitions obtainable type-II NCs have been developed in particular for near-infrared emission, using for example CdTe/CdSe or CdSe/ZnTe. In contrast to type-I systems, the PL decay times are longer in type-II NCs due to the lower overlap of the electron and hole wavefunctions. As for the reverse type-I systems a further shell can be overgrown onto type-II CS NCs to improve the fluorescence QY and photostability.

1.7.4. Plasmonic Nanocrystals

Colloid metal-like nanocrystals can exhibit optical absorption spectra similar to colloidal semiconductor NCs. Anyways, this absorption does not originates from transitions among quantized energy states or either from a

bandgap transition. In conductive NCs the collective coherent oscillations of the free electrons, also called surface plasmons, can be excited at a specific wavelength. A schematic illustration of the electric field component of an incoming light wave inducing a polarization of the free electrons is shown in figure 1.9. [2,9]

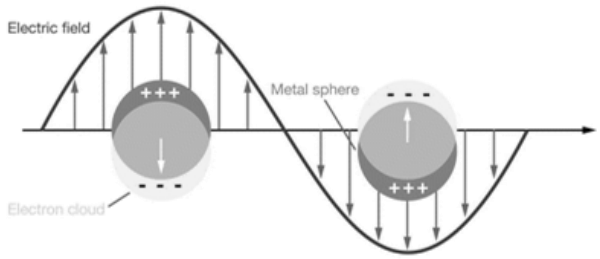

Figure 1.9 Schematic illustration of the excitation of surface plasmons by the electric field component of the electromagnetic radiation. The dipolar oscillation of the free electrons has the same frequency of the incident light.

The peak in the absorption spectrum corresponds to the resonance frequency of the generated surface plasmons. This frequency mainly depends on the density of free electrons in the material but it can be related also to the size of the NCs. Most metals exhibit plasmon resonances in the UV region, but for noble metals (e.g. Ag and Au) and Cu there is a d → s interband transition that can mix with the plasmon resonance shifting it to the visible region

The theory of optical absorption from metallic nanoparticles was proposed by Mie in 1908. The solutions he found for describing the light-nanoparticles interaction solving the Maxwell's equations leaded to a series of multipole oscillations of the extinction cross-section (C_{ext}) while the scatter contribution can be considered negligible (due to the small size of the NCs):

$$C_{ext} = \frac{2\pi}{k^2}\sum_{n=1}^{\infty}(2n+1)Re(a_n + b_n)$$

Where $k = \frac{2\pi\sqrt{\epsilon_m}}{\lambda}$, ϵ_m is the dielectric constant of the surrounding medium, a_n and b_n are Ricatti-bessel functions that depend of the wavelength and the NC radius (R). For nanocrystals the higher order extinction terms can be considered negligible so that it can be written:

$$C_{ext} = \frac{24\pi^2 R^3 \epsilon_m^{3/2}}{\lambda} \frac{\epsilon_2}{(\epsilon_1 + 2\epsilon_m)^2 + {\epsilon_2}^2}$$

Where ϵ_1 and ϵ_2 are the real and imaginary part of the frequency-dependent dielectric constant ϵ of the material. The Drude model relates the dielectric constant to the bulk plasmon frequency, ω_p and the dampening frequency ω_d:

$$\omega_p = \frac{N_e e^2}{m_e^* \epsilon} \quad ; \quad \omega_d = \frac{V_f}{L}$$

Where N_e is the concentration of free electrons, m_e^* is the effective mass of the electrons, V_f the velocity of the electrons at the Fermi level and L is the mean free path. If the diameter of a particle is comparable with the mean free path of an electron, the effective mean path (L_{eff}) becomes dependent on the radius R of the NC as:

$$\frac{1}{L_{eff}} = \frac{1}{2R} + \frac{1}{L}$$

Dispersions of metallic nanoparticles in solution show characteristic colors depending on the size of the NCs and on the dielectric constant of the solvent. The prediction of such a color can be predicted from the C_{ext} knowing R and calculating the absorbance maximum (that occurs for $\epsilon_1 = -2\epsilon_m$).

1.7.5. Doped Nanocrystals

Doping is critical for semiconductors, which would otherwise be electrically insulating. Impurities can strongly modify electronic, optical, and magnetic properties of bulk semiconductors. A substitutional impurity, with one more valence electron than the host cation that replaces, can be ionized by thermal energy and donate its extra electron to the semiconductor (n-type doping). Similarly, an impurity with one less valence electron can provide an extra hole (p-type doping). For nanocrystals, where applications often require thin conducting films, the ability to introduce these carriers is essential. Dopants in nanocrystals lead to phenomena not found in the bulk because their electronic states are quantized. For example, n-or p-type dopants can auto-ionize without thermal activation. This occurs because a carrier inside the crystallite must occupy one of the confined electronic states. Below a critical radius, the confinement energy

exceeds the Coulomb interaction between the ionized impurity and the carrier, which then automatically occupies a nanocrystal state. A typical nanocrystal, 5 nm in diameter consists of a few thousand atoms. Adding a single impurity implies a dopant concentration of the order of 10^{-3} (or 10^{19} cm^{-3}). Considering that in a bulk semiconductor the dopant concentration is normally not more than 10^{17} cm^{-3}, in NCs we can speak about extremely heavy doping. [10]

In colloidal synthesis doped NCs are made by combining molecular precursors that contain the constituent elements. However the resulting nanocrystals must be carefully characterized to determine whether the impurity has been incorporated. To date, only a few analytical techniques have shown the ability to distinguish impurities on the surface from those inside. Electron paramagnetic resonance (EPR) is able to reveal spin interactions that are sensitive to the local environment of the impurity and so it's often used for this purpose.

Since in colloidal synthesis the thermodynamic equilibrium is not established, then kinetic factors such as activation barriers will control the doping process. The impurity must adsorb on the surface of the nanocrystal and then be covered by additional material (see figure 1.10).

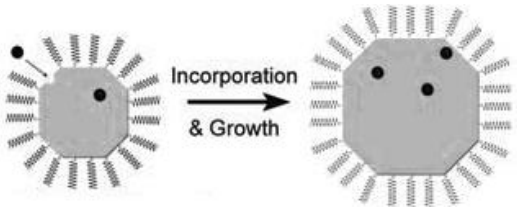

Figure 1.10 Schematic representation of the formation of a doped nanocrystal in colloidal solution, where the thermodynamic equilibrium is not reached.[10]

For this to occur, the surface must be favorable for impurity binding. Since the nature of the surface depends on the crystal structure and lattice plane exposed by the NC, these two factors can affect doping. Moreover, in colloidal synthesis, surfactants don't have to bind the surface or the impurity too strongly. Lastly, additional material must adhere so that, in the absence of diffusion, the impurity becomes trapped.

1.8 References

[1] Soon Gu Kwon and Taeghwan Hyeon, Chemical Synthesis and Formation Kinetics of Uniformly Sized Nanocrystals of Metals, Oxides, and Chalcogenides, *Accounts of Chemical Research*, **2008**, Vol. 41, No. 12, 1696-1709

[2] C.N.R. Rao, P. John Thomas, G.U. Kulkarni, Nanocrystlas: Synthesis, Properties and Applications, *Springer*, **2007**.

[3] Cozzoli PD, Manna L., Synthetic strategies to size and shape controlled nanocrystals and nanocrystal heterostructures, *Adv Exp Med Biol.*, **2007**,620 ,1-17.

[4] C. B. Murray, C. R. Kagan and M. G. Bawendi, Synthesis and characterization of monodisperse nanocrystals and close-packed nanocrystals assemblies, *Annu. Rev. Mater. Sci.,* **2000**. 30:545–610

[5] Emil Roduner, Size matters: why nanomaterials are different, *Chem. Soc. Rev.,* **2006**, 35, 583–592.

[6] Editor: Günter Schmid, Nanoparticles: From Theory to Application, *John Wiley & Sons,* **2010.**

[7] Jim Goodwin, Colloids and Interfaces with Surfactants and Polymers, *John Wiley & Sons, **2004***.

[8] P. Reiss, M. Protiere and L. Li, Core/Shell Semiconductor Nanocrystals, *small*, **2009**, 5, No. 2, 154–168

[9] Charina L. Choi and A. Paul Alivisatos, From Artificial Atoms to Nanocrystal Molecules: Preparation and Properties of More Complex Nanostructures, *Annu. Rev. Phys. Chem.*, **2010**, 61, 369–389

[10] David J. Norris, Alexander L. Efros, Steven C. Erwin, Doped Nanocrystals, *Science,* **2008**, vol 319.

[11] Yoffe A. D., Semiconductor quantum dots and related systems: electronic, optical,luminescence and related properties of low dimensional systems, *Advances in Physics*, **2001**, vol.50, n.1, 1- 208.

[12] Guozhong Cao and Ying Wang, Nanostructures and Nanomaterials: Synthesis, Properties, and Applications, *World Scientific*, **2010,** 2nd ed.

Colloidal Shynthesis of Nanocrystals

2.1 Introduction

Colloidal nanocrystals (NCs) are synthesized through wet chemical procedures and can be visualized as nanocrystals embedded in organic ligands growing in the solution media. The liquid reaction is typically constituted of a solvent, surfactants (also called capping agents) and reactants. Upon heating at high temperature (150-400°C) the reactants (also called precursors), containing the atomic species that will form the NC, decompose thermically or chemically forming the building blocks (monomers) necessary for the nucleation and growth of the nanocrystals. On the other side the surfactants are molecules stable at high temperature and capable of binding to the surface of the growing crystals regulating their growth and shape while preventing their aggregation. The capping agents are normally amphiphilic molecules composed of a metal coordinating "head", that binds to electron-poor metal atoms (e.g. adatoms) at the surface of the nanocrystal, and a non-polar "tail" compatible with the solvent determining the solubility of the nanocrystals. Typical surfactants used in colloidal synthesis are thiols, amines, carboxylic acids, phosphonic acids and phosphines. The choice of the appropriate surfactant for a given crystalline structure is still empirical.[1-2]

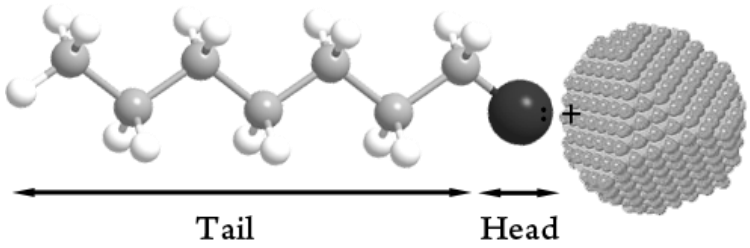

Figure 2.1 Schematic representation of a surfactant linked to a NC surface. As depicted, the head of a capping agent is typically an electron-donating group that can link to the metal atoms on the surface.

The formation of nanocrystals involves two steps: nucleation and growth. In the first step the precursors form the monomers that rapidly react forming the nuclei of nanocrystals. These nuclei if stable can grow by the addition of the remaining monomers. The final product is a stable colloidal solution of nanocrystals covered by organic molecules dispersed in the starting organic solvent.

The reaction temperature plays a fundamental role on the synthesis of colloidal nanocrystals. The atoms in the forming crystals, in fact, need to have enough thermal energy to rearrange in ordered structures. Luckily, lower temperatures, in respect to bulk systems, are needed since in nanometric scale the melting temperature for a material is strongly reduced as a thermodynamic size effect.[3] It is important to consider also that the surfactants not only bind to the surface of the NCs, but also form complexes with the precursors used. The thermal stability of these complexes and the affinity of the surfactant to the surface are parameters that strongly depend on the temperature too. A high reaction temperature leads to less stable complexes, higher reactivity of the monomers (increased diffusion rate) and weaker binding of the capping agent to the NC surfaces. So working at too high temperatures could lead to very big particles with poor control over the size and the shape or often to aggregated systems. Choosing a suitable reaction temperature is consequently extremely important for controlling the size and the shape of colloidal NCs.

The nature of the surfactant is another key parameter to regulate the synthesis of the colloidal NCs. High coordinating ligands can hinder the nucleation and/or growth of the NCs while weak surfactants cannot prevent the aggregation of the forming particles. Different surfactants can bind preferentially to different lattice planes of a crystal structure. A smart choice of specific surfactants can lead to NC with specific shapes (e.g. platelets, rods, spheres etc.).

Post-synthesis surfactant exchange can be performed in order to stabilize the NCs in the desired solvents or to give specific functionalities to their surface. The possibility of combining the properties of inorganic solids with the low-cost high-volume processing of their colloidal solutions is nowadays extremely important for their development in the industrial world.

2.2 Growth of Colloidal Nanocrystals

A big challenge in the synthesis of colloidal NC is the control over the size distribution. To understand how to tune the size of growing NCs we have to consider how the surface energy of a NC changes in function of the size. When a NC is very small a high fraction of its atoms is present on the surface. The surface energy of such a small NC is so high that the crystal cannot be stable and consequently its growth rate is negative (left part of the graphs in figure 2.2). When the size of a NC crosses the so called "critical size" (at which the growth rate is equal to zero) the surface energy gets small enough to allow the growth of the crystal itself. The concentration of monomers plays a key role in the synthesis: the higher is the concentration of monomer the lower is the critical size of the NCs (figure 2.2). The concentration of initial precursors is fundamental for a complete control over the synthesis of colloidal NCs.[2,4]

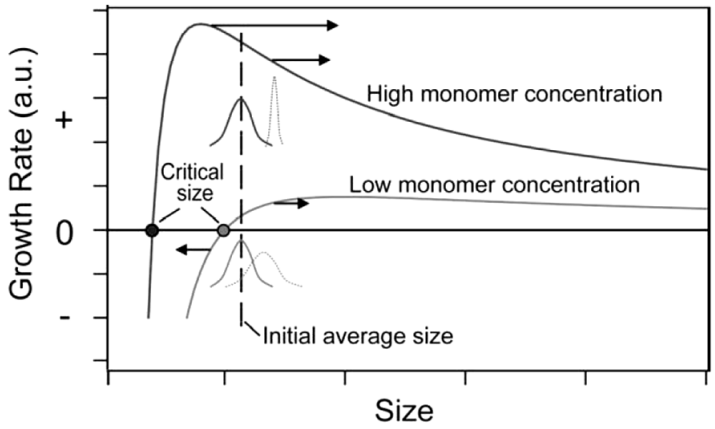

Figure 2.2 Grow rate of colloidal nanocrystals in function of their size. Depending on the monomer concentration the growth process can vary. If the concentration of monomer is high the critical size is small: small nanocrystals are stable and can grow faster than larger ones. This case is also known as "focusing" process and monodisperse systems can be obtained as a result of it. When the concentration of monomer is below a certain threshold, small nanocrystals are not stable anymore so that they are consumed during the growth of bigger NCs. The size distribution in this case gets broader and the process is called "defocusing".

Working at slow growing rate (low monomer concentration) to obtain good cristallinity and spherical crystals has, therefore, undesired consequences in the size distribution (see figure 2.2). In this regime, that is well known as Ostwald ripening, big nanocrystals grow consuming the small nanocrystals (that are less stable and consequently tend to dissolve) leading to a polydisperse sample.

A common wise method to avoid this problem is to use multiple additions of precursor. During the growth of nanocrystals the concentration of monomers lowers so that the product could be made of both small and big particles. At this point the addition of "new" precursors can change immediately the "critical" size promoting the growth of smaller nanocrystals. A weighted choice of the amount of monomers to add the reaction is essential to narrow (or "focus") the size distribution. This procedure has been experimentally shown to be a valid way to have a kinetic control over the reaction having the advantage to produce large quantities of NCs with a narrow size distribution.

Another interesting way to get kinetic control over the production of NC is to separate the nucleation event from the growth step. This can be achieved when the nucleation occurs on a short time scale and the growth can proceed over the rest of the synthetic time. For this purpose precursors are rapidly injected into the reaction flask at high temperature in order to induce a so called "nucleation burst". A fast nucleation burst can rapidly consume the precursors shifting the concentration of monomers below the nucleation threshold. The remaining monomers in solution will only add to the existing nuclei. In some cases nucleation and growth can proceed in similar time scales so that a focusing procedure remains necessary to get a monodisperse product. In other cases some time is necessary for the precursors to evolve (through intermediate steps) to active monomers that are able to react. A hot injection in this case is cannot lead to a quick nucleation burst. In general the hot injection method has several intrinsic limitations. First of all, a highly reactive precursor is not available for many materials. Second, extremely vigorous reactions at high temperature can become very dangerous. Third, it is not easy to adapt this method for the large scale synthesis of uniformly sized nanocrystals because it is very difficult to keep a uniform temperature profile in a large-scale reactor.

2.3 Shape Control of Colloidal Nanocrystals

While "spherical" (or cubic) crystals are normally stable because their surface energy is minimized, anisotropic systems are metastable due to their higher surface/volume ratio (aspect ratio). To avoid the formation of thermodynamic stable shapes with a low aspect ratio a kinetic growth regime is necessary. When the growth rate is high enough a broad variety of different shapes can be achieved.[2]

In general the growth rate of a crystal surface depends exponentially on its surface energy, so that at high growth rates, in a kinetically controlled growth regime, high-energy facets will faster than low-energy facets. Surfactants in this case play a fundamental role. As already mentioned these organic molecules are capable of binding the inorganic nanocrystals in a dynamic way so that during the NC growth they are continuously exchanging on the crystals surfaces. Depending on the nature of a certain surfactant the exchange rate on the different crystal planes is not always constant. One surfactant can bind preferentially a specific lattice plane lowering therefore the energy of such a plane. The effect is that the growth of the NC along that direction is slowed down (see figure 2.3a)).

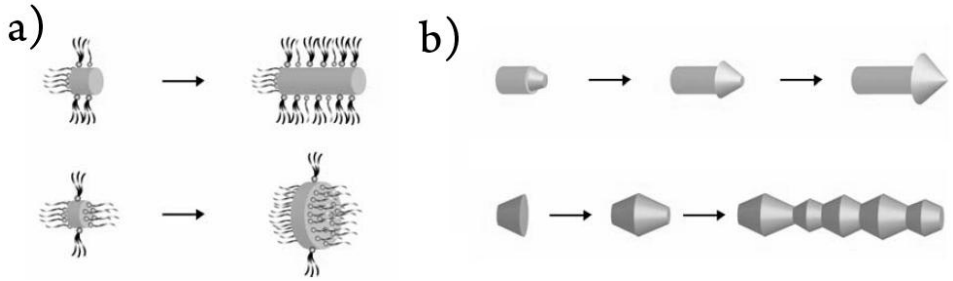

Figure 2.3 Schematic illustration of different shape evolutions. a) Growth of high energy facets in kinetic regime mediated by specific surfactants. The effect of using different organic molecules that bind to preferential crystal planes can lead to the formation of rod or platelet shaped NCs. b) Complex structures can be obtained a result of competing facets with different surface energies.

2.3.1. Complex shapes

Considering that in a crystal there are different facets with different surface energy more complex shapes can be produced in kinetic growth regime. In the simplest case a high energy surface grows fast than all the others and eventually disappears so that the crystal is basically terminated by low energy facets. Let's consider a case in which we have three different facets in which one grows very

fast, a second one that is slightly slower and a third one that is extremely slow. The highest energy facet in this case can grow so fast that its growth doesn't follow layer by layer steps but atoms are added so fast that an intermediate more stable face (the second one we considered) can form. At this point this second facet will persist, replacing the first high-energy facet and, of course, growing faster than the most stable one. Very complex structures can be the effect of these competing crystal planes like arrow shaped CdSe or zigzag shaped TiO_2 NCs (see figure 2.3b).[2]

Another interesting way to achieve more complex structures is the so called "oriented attachment". This process involves the coalescence of two (or more) different formed nanocrystals in order to eliminate the facets with higher energies. The mechanism of this phenomenon that occurs in many different systems is still unclear but it oriented attachment remains unclear. The most frequent products of oriented attachment are rods and wires but also more complex branched systems [2,5].

2.4 Hybrid Nanocrystals

The most recent developments of colloidal syntheses involve the fabrication of more elaborate hybrid nanocrystals (HNCs). Such nanostructures are made of different materials fused together in a single particle without bridging molecules. These nanoparticles can posses multiple functionalities and multiple chemical-physical properties coming from each componing material. For instance hybrid NCs based on combinations of semiconductors, metals and oxides. In core-shell (CS) type configuration can exhibit improved behavior as compared to a single individual component: such as enhanced plasmon absorption, photoluminescence, magnetic behaviour and improved photocatalytic and photoelectrochemical responses. HNCs made of distinct inorganic domains attached together one next to each other, the properties inherent to each domain, such as magnetism, plasmon absorption or fluorescence, can be altered because of the contact junction with the other material. In semiconductor heterostructures, for example, depending on the relative band gap alignment of the two domains, the charge carriers can be either localized preferentially in one domain or separated more efficiently, which can have important implications in optoelectronic and photovoltaic applications.[1]

The synthesis of these complex colloidal systems relies on a simple principle deriving from the classical nucleation theory: the activation energy to generate new nuclei in solution (homogeneous nucleation) is usually higher than the energy required to enlarge pre existing NCs (heterogeneous nucleation). The technique adopted to create such a systems is called "seeded growth". Preformed NCs of one material (called the "seeds") are inserted into a solution containing the monomers to build a second different material which prefers to heterogeneously grow onto the seeds rather than nucleating in new NCs. The final 3D configuration of the HNCs is hard to predict because it depends on many factors such as the lattice mismatch, the crystal miscibility and on the specific surface energies of the facet exposed by the initial seeds.

2.4.1. Core-Shell Nanocrystals

A particular kind of heterostructures is represented by Core-Shell NCs in which a large interface is shared between two materials. In these systems the initial NCs seeds are uniformly covered by a second (or even more) crystalline material forming an onion-like hybrid nanostructure (figure 2.4a). Techniques to overcoat NCs with an inorganic shell are remarkably general with only a few modest constraints: (a) The respective lattice constants do not differ significantly, (b) the existing NC seeds must be stable in the synthetic conditions used to grow the second phase, (c) the surface energies of the two phases must be sufficiently similar so that the heterogeneous nucleation is preferred to the homogeneous one, and (d) the seed NC and the overcoat material must not readily interdiffuse under the deposition condition. The typical synthesis of these structures consists in the dropwise addition of the shell molecular precursors to a solution containing the nanocrystalline cores at relatively low temperatures. Low concentration of shell monomers and low temperatures are crucial parameter to prevent homogeneous nucleation of the second material. More complex techniques have been also adopted to grow metal, semiconductor, magnetic or oxide material shells: a) co-reaction of all the necessary molecular precursors, b) alternate deposition of monolayers of each atomic species that will compose the shell (figure 2.4a 1-3), c) modification of the external layer/s of a core NC through redox reactions (figure 2.4b) and (d) thermal annealing an initially amorphous and/or discontinuous shell (figure 2.4c). [1,6]

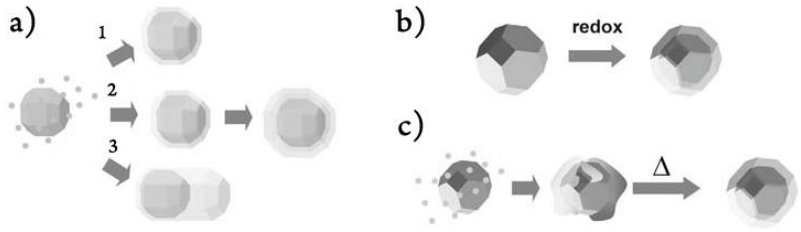

Figure 2.4 Schematic representation of possible mechanisms leading to core-shell nanocrystals. a1) Growth of a monolayer or a2) multilayer and a3) asymmetric shell on a NC core. B) Creation of a shell via redox reactions that involve the outer layers of the initial NC core. c) Uniform shell formation upon thermal annealing of an initially amorphous and/or discontinuous coating.[1]

2.5 Post Synthetic Purification of NCs

NCs are stable with respect to aggregation only if the capping groups provide a repulsive force of sufficient strength and range to counteract the inherent van der Waals attraction between NCs. The stabilization provided by the surfactants is strongly dependent on their affinity to the solvent used. In washing procedures the introduction of a non-solvent, miscible with the original dispersing solvent, is used to destabilize the NC dispersions. The NCs then aggregate and precipitate leaving many of the synthetic by-products in the liquid phase. After a short centrifugation it is possible to physically separate the inorganic powder from the rest. If the capping groups are well bound to the surface of the NCs, the resulting powders are redispersible in a variety of solvents normally compatible with common surfactants used in colloidal synthesis: alkanes, aromatics, long-chain alcohols, chlorinated solvents, and organic bases. Repeated flocculation and redispersion of the NCs in fresh solvents allow the isolation of powders composed of the desired NCs and their intimate organic capping layer. [6]

A straightforward extension of this precipitation process allows the isolation of size-selected fractions of NCs. Size-selective precipitation usually involves the titration of a non-solvent into the dispersion. Since the largest NCs in the size distribution exhibit the greatest attractive van der Waals forces, they tend to aggregate first excluding, at the same time, smaller NCs which remain soluble. Working in this way it's possible to achieve a partial flocculation of the NCs. The centrifugation of such a dispersion produces a precipitate enriched in the larger NCs and leaves the smaller NCs dispersed in the supernatant. The precipitate and the supernatant can be then treated and washed separately as two different

samples made of NCs with different size. Repeated cycles of selective precipitation can be performed on a same sample to further narrow the size distribution.

2.6 Ligand Exchange

Stabilizing agents must be present during growth of colloidal NCs to prevent aggregation and to achieve the desired shapes. But the surface properties of the obtained systems are often not ideal for post processing steps in which the nanocrystals need to be characterized or better used in a specific way. The ability to engineer surface properties of nanocrystals is important for various applications, as many of the physical and chemical properties of nanoscale materials are strongly affected by the surface chemistry.[6]

NCs' surface can be modified by ligand exchange techniques. Exposing the NCs to an excess of a competing capping group a surfactant exchange occurs driven by a mass action. This approach is effective in capping NCs with a wide range of chemical functionalities, even if the binding of the new cap is less favorable than the original.

A general route that has been lately developed is a "sequential surface functionalization". The first step is called ligand stripping because the original ligands are actually stripped from the surface using specific salts like $NO^+BF_4^-$ or Meerwein's salt ($Me_3O^+BF_4^-$) (see figure 2.5). The process involves the transfer of the NCs from an organic phase (hexane) to an "aqueous" phase (dimethylformamide) capable of stabilizing the bare nanocrystals. The choice of one salt in respect to the other depends on the NCs capacity of withstanding the attack of the oxidative cationic group XO^+ (where X is N or Me_3). In the second step the NCs can be re functionalized with the desired capping agent just exposing them again to an organic solution containing the surfactants. (see figure 2.5).

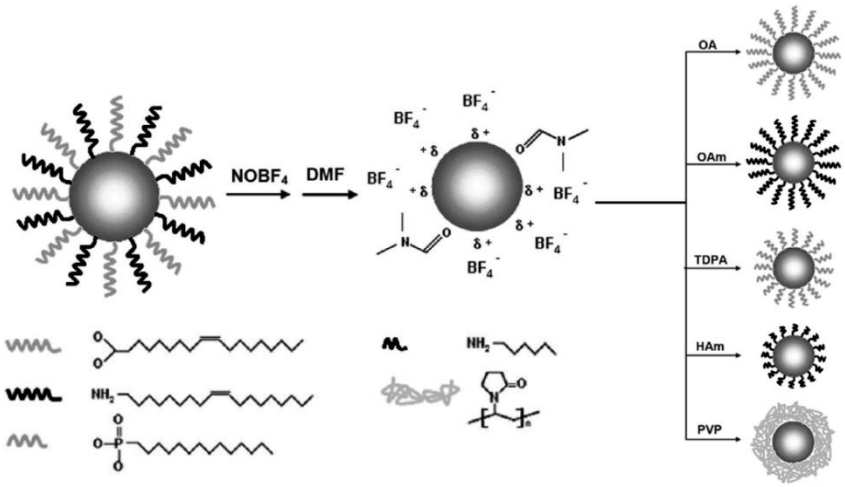

Figure 2.5 Schematic illustration of the ligand-stripping process with $NOBF_4$ and the secondary ligand-exchange process, showing the surface functionalization of the NCs by various capping agents: oleic acid (OA), oleyilamine (OAm), tetradecylphosphonic acid (TDPA), hexylamine (Ham), poly vinyl pyrrolidone (PVP). [7]

2.7 Cation exchange

A typical problem associated with the colloidal synthesis NCs is the difficulty in producing particles with the same size but different compositions. Even though the size can often be tightly controlled for an individual colloidal system, it is challenging to fine-tune the size so that a very close match will be achieved for colloidal NCs of different compositions.[8-11]

Cation exchange reactions are very attractive to this end because the morphology of the starting materials can be preserved during the exchange process. Just like organic molecules inorganic nanocrystals may also undergo chemical transformations. Simple substitution reactions of cations inside the crystal lattice highlight the ability of nanocrystals to transform as molecular entities. It is generally assumed that during such an exchange, the anionic framework of the crystal is conserved, while the cations, due to their relatively smaller size and higher mobility, undergo replacement. It has been also shown that cation exchange reactions are possible in nanocrystalline samples because the effective reaction barrier is much lower than in larger systems thanks to an enhanced surface access and lower activation barriers to diffusing ions. Example of cation exchange are getting more common everyday and the mechanism as been show to work for many different NCs. Cations including Ag^{+}, Sb^{3+}, Bi^{3+},

and Cu^{+} have been used to replace Cd^{2+} in thin films of CdSe and CdS. Cation exchange reactions between Cu^{2+} and Cd^{2+} can lead to the transformation of CdS nanocrystals into CuS. Moreover, the ZnS can be converted into Ag_2S, Cu_2S, and Bi_2S_3 with conservation of the original morphology. Some experimental results are shown in figure 2.6.

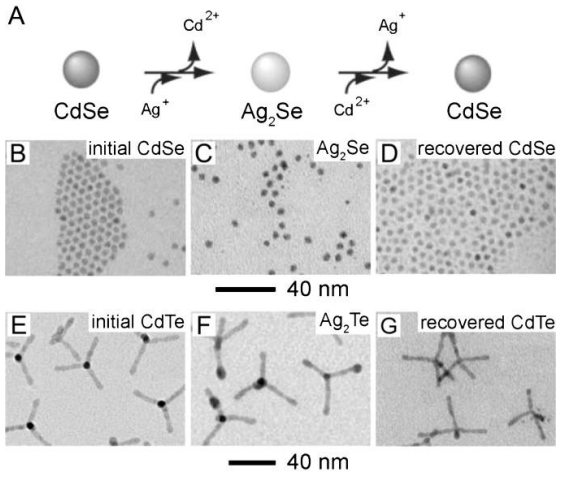

Figure 2.6 (A) Schematic showing the cation exchange between CdSe and Ag_2Se. (B–D) TEM images of the initial CdSe nanocrystals, Ag_2Se derived via a forward cation exchange reaction (C), and CdSe nanocrystals recovered using a reverse cation exchange reaction (D). (E–G) TEM images of the initial CdTe tetrapods (E), Ag_2Te tetrapods produced from cation exchange of CdTe (F), and CdTe recovered through a reverse cation exchange reaction (G).[11]

The cation exchange reactions are often carried out in solutions containing the respective salt precursors. In these reactions, a large difference in solubility provides the driving force for the ion replacement. Generally, the starting material present in a solution containing an appropriate precursor will spontaneously undergo cation exchange to yield the product with a lower solubility. On the other hand, when the solubility of the desired product is higher than the solubility of the precursor material, new strategies are needed. An extra molecule/ligand can be added to the solution to modify the equilibrium. The new added ligand can bind to NCs' cations forming intermediate complexes to facilitate the cation exchange by allowing the association of the cations in solution with the anion sublattice.

The interesting fact is that in cation exchange reactions the shape is completely preserved while the composition is completely modified leading to totally different semiconductor material. This observation suggests that cation exchange is a valid alternative route toward the synthesis of nanocrystals with complex compositions of just difficult to synthesize by colloidal routes.

2.8 References

[1] Cozzoli PD, Manna L., Synthetic strategies to size and shape controlled nanocrystals and nanocrystal heterostructures, *Adv Exp Med Biol.*, **2007**,620 ,1-17.

[2] Jim Goodwin, Colloids and Interfaces with Surfactants and Polymers, *John Wiley & Sons, **2004**.*

[3] Buffat, P. & Borel, J-P., Size effect on the melting temperature of gold particles, *Phys. Rev. A,* **1976**, 13, 2287–2298.

[4] Soon Gu Kwon and Taeghwan Hyeon, Chemical Synthesis and Formation Kinetics of Uniformly Sized Nanocrystals of Metals, Oxides, and Chalcogenides, *Accounts of Chemical Research*, **2008**, Vol. 41, No. 12, 1696-1709

[5] R. Buonsanti et al, Hyperbranched Anatase TiO2 Nanocrystals: Nonaqueous Synthesis, Growth Mechanism, and Exploitation in Dye-Sensitized Solar Cells", *J. Am. Chem. Soc.*, **2011**, 133, 19216.

[6] C. B. Murray, C. R. Kagan and M. G. Bawendi, Synthesis and characterization of monodisperse nanocrystals and close-packed nanocrystals assemblies, *Annu. Rev. Mater. Sci.,* **2000**. 30:545–610

[7] Angang Dong et al., A Generalized Ligand-Exchange Strategy Enabling Sequential Surface Functionalization of Colloidal Nanocrystals, *J. Am. Chem. Soc.,* **2011**, 133, 998–1006.

[8] Charina L. Choi and A. Paul Alivisatos, From Artificial Atoms to Nanocrystal Molecules: Preparation and Properties of More Complex Nanostructures, *Annu. Rev. Phys. Chem.*, **2010**, 61, 369–389

[9] Pedro H. C. Camargo et al., Cation Exchange: A Simple and Versatile Route to Inorganic Colloidal Spheres with the Same Size but Different Compositions and Properties, *Langmuir,* **2007**, *23,* 2985-2992

[10] Prashant K. Jain, Lilac Amirav et al., Nanoheterostructure Cation Exchange: Anionic Framework Conservation, *J. Am. Chem. Soc.*, **2010**, 132 (29), pp 9997–9999.

[11] D.H. Son et al., Cation Exchange Reactions in Ionic Nanocrystals, *Science*, **2004**,306, p. 1009.

Characterization of Nanocrystals

3.1 Introduction

Many studies have investigated the structure and chemical composition of NCs in an effort to reveal the structure/property relationships as the crystals grow from molecular species toward bulk solids. This is still a big challenge because the smallest NCs (<1 nm) are nearly molecular (<100 atoms) and the largest NCs (>20 nm) contain >100,000 atoms. In this very broad range the percentage of surface atoms goes from >75% to <0.5% (almost bulk). Standard chemical and surface sensitive strategies are well suited for study of the smaller NCs whereas physical probes, which exploit the periodicity of the internal NC lattice, are better suited for the larger ones.[6]

3.2 Chemical Analysis of Nanocrystals

Detailed elemental analysis is the first essential step in determining the chemical composition of the NCs. Techniques as diverse as atomic absorption and emission, neutron activation, X-ray fluorescence and mass spectroscopy can be employed to reveal the composition of the average NC. Inductively coupled plasma mass spectrometry (ICP-MS) or atomic emission spectroscopy (ICP-AES)

are very powerful techniques that are commonly used now days to determine the mean composition of NCs. In the first one the samples is ionized with inductively coupled plasma and then a mass spectrometer is used to separate and to quantify the formed ions. The second one is a particular emission spectroscopy that exploits the inductively coupled plasma to produce excited species (atoms and ions) which emit at specific wavelength depending on the atomic specie. The intensity of this emission is proportional to the concentration of the element inside the sample. [1]

The use of a specific chemical spectroscopy as infrared absorption, photoelectron spectroscopy, and electron energy loss spectroscopy (EELS) can be useful to know not only what species are present in the NCs but how the components are distributed within the NCs.

3.3 X-ray photoelectron spectroscopy (XPS)

X-ray photoelectron spectroscopy (XPS) is an analytic method to determine the chemical species on the surface of a sample. When a material is irradiated with a beam of X-rays some electrons escape from its surface with energies that depend on the atomic levels of the elements constituting the sample. This is known as photoelectric effect, and it can be expressed as:

$$E_k = hv - \Phi - E_B$$

where E_k is the kinetic energy of the photo-emitted electron, hv is the energy of the incident X-ray beam, Φ is the work function of the spectrometer and E_B is the binding energy of the electron. The last one is basically the energy required to release an electron from its atomic orbital (e.g., 1s, 2s, 2p, 3s) and therefore for every element we have specific binding energies. In a XPS experiments the kinetic energy and number of electrons that escape from the surface (1 to 10 nm) of the NCs are measured (see fig 3.1).

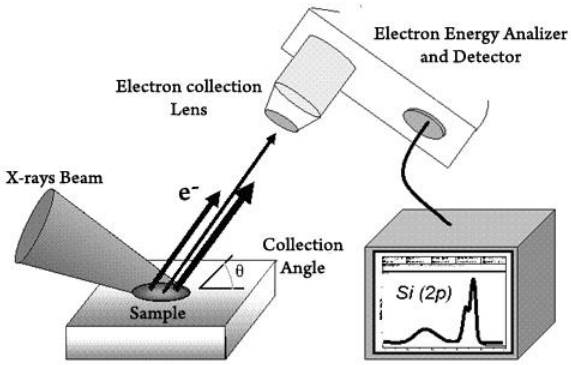

Figure 3.1 Sketch of XPS experimental setup. (Wikipedia)

It is then possible to evaluate not only the chemical species on the surface but also their relative abundance. To count the number of electrons at each kinetic energy value, with the minimum of error, XPS must be performed under ultra-high vacuum (UHV) conditions because electron counting detectors in XPS instruments are typically one meter away from the material irradiated with X-rays.

3.4 Transmission Electron Microscopy (TEM)

Transmission Electron Microscopy is definitely one of the most remarkable technique for characterizing NCs and their assemblies. Typically a drop of a diluted colloidal dispersion is deposited on a mesh grid coated with a thin polymer or carbon film. When it has dried, the grid is placed in the microscope column which is then evacuated. An electron beam is used as source of "light" that hits the sample. The transmitted beam produces an image which is focused onto a fluorescent screen (see fig 3.2). [1-2]

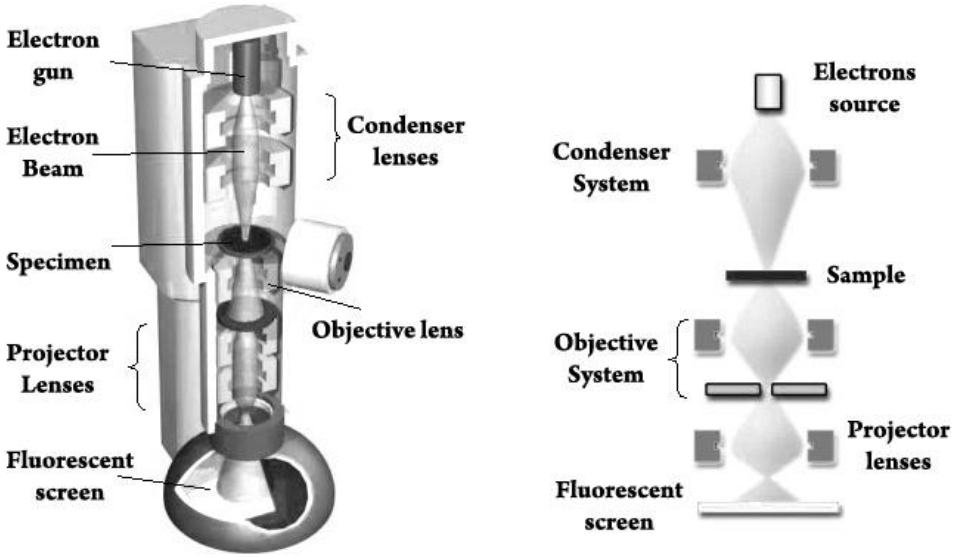

Figure 3.2 Representation of a Transmission Electron Microscope (left) and sketch of the optical experimental setup in a TEM (right).

To focus the electrons electromagnets are employed and the wavelength of the beam is controlled by the accelerating voltage, with 100kV or 200kV being typical values so that the resolution of < 1nm is achieved. The limit is not inherent in the instrument but often depends on the electron densities of the materials analyzed and their thermal stability. Crystals made of elements with high atomic numbers produce more efficient electron scattering and so better contrast is obtainable. The heating effect of the electron beam is greater in the focused intense beam used at higher magnification and this can cause degradation (shrinking or decomposition) of the NCs.

Low-resolution TEM (applied voltage typically 100kV) studies allow a statistical description of the size and shape of NCs. High resolution TEM (HRTEM) imaging can reveal not only the shape of an individual NC but also its crystallinity allowing, at the same time, the detailed analysis of its crystal structure. Normally the measurement of several hundred NCs (usually 200) in a series of images are employed to develop a statistical model of NC size and shape, while 10 to 20 HRTEM images, are used to develop a description of internal NC structure. These limited observations must be compared with X-ray scattering studies, which simultaneously probe statistically large ensembles of NCs.

3.4.1. Spectroscopy Combined With TEM

TEM combined with a specific spectroscopy can be an extremely powerful instrument for a detailed and specific chemical mapping of nanosized crystals. For

example Electron Energy Loss Spectroscopy (EELS) or Energy-dispersive X-ray spectroscopy (EDS) can be performed directly in the electron microscope not only to detect the elements constituting a single NC and their ratios but also to estimate their distribution in the NC itself.

In electron energy loss spectroscopy (EELS) the nanocrystals are exposed to the incident electrons beam of electrons with a specific known energy. The electrons can be either elastically or inelastically scattered by the atoms of the NCs and may lose some energy. Depending on the nature of the scattering phenomena different information can be obtained. In low-loss region (< 100eV) the dominant feature is the zero loss peak. The zero loss peak represents electrons that suffered no inelastic scattering. In this region also induced plasmon oscillations occur. Since the plasmon generation is the most frequent inelastic interaction of electron with the sample, the intensity in this region is relatively high. Intensity and number of plasmon peaks increases with specimen thickness. In the high-Loss region (> 100eV) we have the ionization of atoms that requires a minimum ionization energy. The incident electron has, in fact, to expel an inner-shell electron, which leads to ionization edges in the spectrum at energy losses. Since each element has a unique electron orbital configuration, the adsorption edges are different for each element. Further, the intensity of the adsorption edge is proportional to the number of atoms present which adsorb energy (corresponding to that adsorption edge) from the transmitted electrons. Therefore, quantification of elemental abundances can determined from the integration of the intensities under absorption edges. Compared to the plasmon generation, the inner-shell ionization is a much less probable process, leading to a low intensity of the peaks. Element-specific energies lost due to inner shell ionizations of atoms are taken into account for chemical mapping. An example of an EELS spectrum is given in figure 3.3. The technique is particularly effective for light elements and the energy resolution is typically 1 eV but can approach 0.1 eV if an electron-beam monochromator is used.

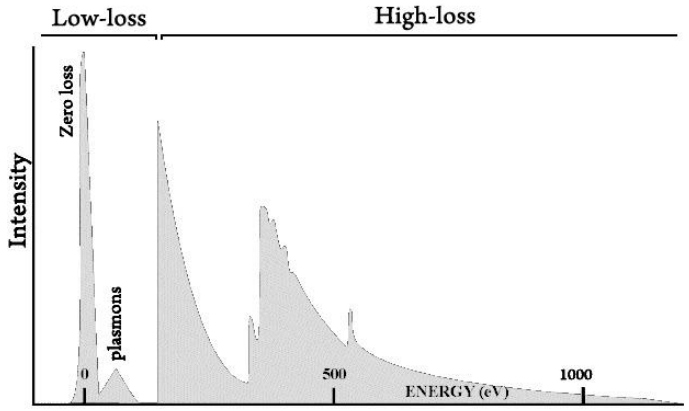

Figure 3.3 Example of a TEM-EELS spectrum. Since the intensity of the peaks in the high-loss region is very low the gain change used is 500 time higher than the low-loss one.

The Energy-dispersive X-ray spectroscopy (EDX) is normally used in chemical analysis of samples. The NCs are irradiated with a high energy beam of electrons. The electrons in the inner shells of the atoms can be excited producing, in the relaxation to the ground level, X-ray emission with. The X-rays emitted from a specimen can be detected and measured by an energy-dispersive spectrometer connected to the TEM. As the energy of the X-rays is characteristic of the atomic structure of the elements this allows the elemental composition of the specimen to be measured. Thus the chemical analysis and mapping of the NCs, especially for medium-heavy and heavy elements is achieved with this technique.

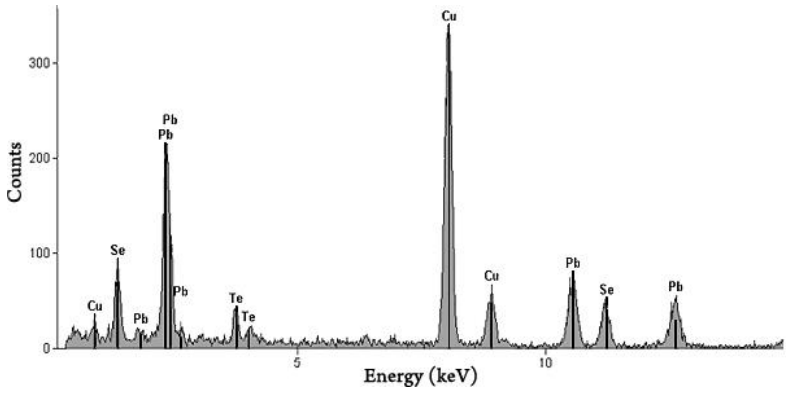

Figure 3.4 Example TEM-EDS spectrum relative to a mixture of PbSe and PbTe NCs on a typical copper grid.

3.5 X-Ray Diffraction (XRD)

The X-Ray diffraction is a powerful tool daily used to determine the crystal structure of the synthesized NCs.[3]

When X-rays interact with a solid material the scattered beams can add together in a few directions and reinforce each other to yield diffraction. The regularity (periodicity) of the material is responsible for the diffraction of the beams. Diffraction can occurs when any electromagnetic radiation interacts with a periodic structure which repeating distances must be about the same wavelength of the radiation.

For a crystal structure it's possible to define a repeating unit cell represented by three vectors $\vec{a}_i, \vec{b}_i, \vec{c}_i$. A family of lattice planes in a crystal structure can be identified by three integers h, k, l, (the Miller indices). For example, given the three Miller indices h, k, l, (hkl) denotes planes orthogonal to the reciprocal lattice vector, $\vec{v}_{hkl}$:

$$\vec{v}_{hkl} = h\vec{a} + k\vec{b} + l\vec{c}$$

where $\vec{a}, \vec{b}, \vec{c}$ are the reciprocal vectors of the unit cell.

Let us consider an X-ray beam incident on a pair of parallel lattice planes (hkl), separated by an interplanar spacing d_{hkl}. Two parallel incident rays make an angle (θ_{hkl}) with these planes. A reflected beam of maximum intensity will result if the waves are in phase. To this to be verified, the difference in path length must then be an integral number of the wavelength, λ. The relationship describing the angle at which a beam of X-rays of a particular wavelength diffracts from a crystalline surface was discovered by William H. Bragg and W. Lawrence Bragg and is known as Bragg's Law (see figure 3.5):

$$2d_{hkl}\, sin\theta_{hkl} = n\lambda$$

where n is an integer.

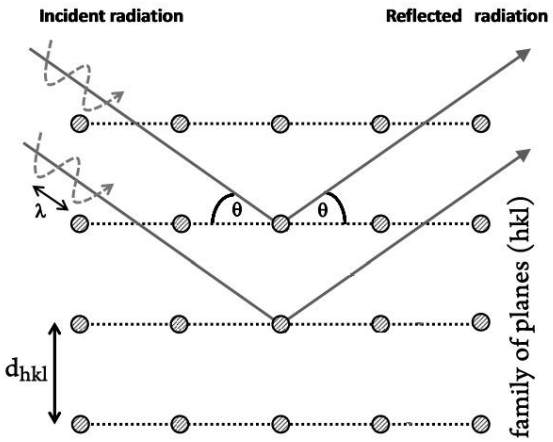

Figure 3.5 Schematic representation of the Bragg's law. When the path difference between the incident and the reflected beams is equal to an integral number of wavelengths, then the scattered beams are in phase.

The intensities of the reflections are determined by the distribution of the electrons in the unit cell. The intensities depend on what kind of atoms we have and where in the unit cell they are located. Therefore planes with high electron density will reflect strongly, planes with low electron density will give weak intensities. A typical diffraction spectrum of a NCs sample consists of a plot of reflected intensities versus the angle 2θ.Each reflection is fully defined when we know the d-spacing, the intensity (area under the peak) and the indices h, k, l. So for a given diffraction pattern it's possible to identify univocally a specific crystal structure.

Homogeneous or uniform elastic strain in a material can shift its diffraction peak positions. From the experimental shifts measured, one can calculate the change in d-spacing, that is the result of the variation of lattice constants under a strain. Moreover inhomogeneous strains can vary from NC to NC and this can cause a broadening (rather than a single shift) of the diffraction peaks that increases with sinθ.

Peak broadening is also caused by the finite (nanometric) size of the NCs, and in this case it's independent from sinθ. If we consider a sample made of NCs, in absence of inhomogeneous strains, it's possible to estimate the NCs size, D, from the peaks width using the Scherrer's formula:

$$D = \frac{k\lambda}{B cos\theta_B}$$

where B is the full width of half maximum (FWHM) of the diffraction peak at angle θ_B and k is the Scherrer's constant (normally of the order of unity for usual crystals). In case of inhomogeneous strain and finite crystal size the analysis of the XRD peaks becomes more complex.

3.6 Infrared spectroscopy (IR)

Photon energies associated with the infrared (IR) region of the spectrum are not large enough to excite electrons, but may induce vibrational excitation of covalently bonded atoms and groups. In addition to the facile rotation of groups about single bonds, molecules experience a wide variety of vibrational motions, characteristic of their component atoms. Consequently, virtually all organic compounds will absorb infrared radiation that corresponds in energy to these vibrations (resonance conditions). Infrared spectroscopy is based on the fact that molecules absorb specific frequencies that are characteristic of their structure.

In general a molecule composed of n-atoms has 3n degrees of freedom, six of which are translations and rotations of the molecule itself. This leaves 3n-6 degrees of vibrational freedom (3n-5 if the molecule is linear). Vibrational modes are, in general, stretching, bending, scissoring, rocking and twisting. The exact frequency at which a given vibration occurs is determined by the strengths of the bonds involved and the mass of the component atoms. It's fundamental, also, to take into account that one selection rule that influences the intensity of infrared absorptions, is that a change in dipole moment should occur for a vibration to absorb infrared energy. So normally not all the 3n-6 modes are "IR active" and detectable through IR absorption. The general region of the IR spectrum in which the various kinds of vibrational bands are observed is the 4000 to 500 cm^{-1} range as shown in figure 3.6.

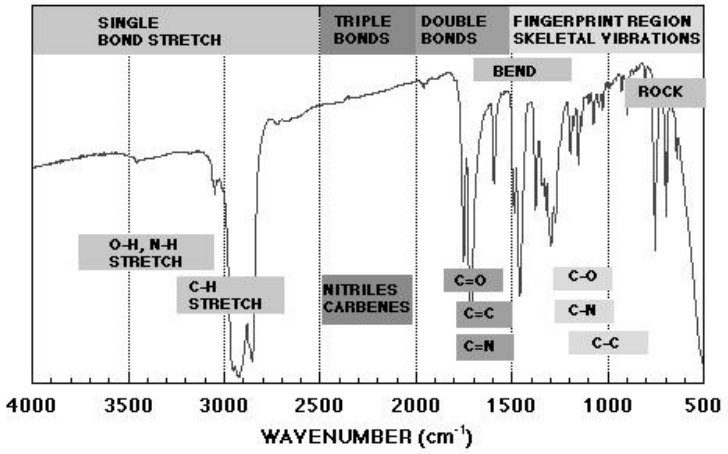

Figure 3.6 An example of experimental IR spectrum is shown. In the graph some typical regions where specific bonds are found in an infrared spectrum have been highlighted. Specific functional groups present on the surfactants used in colloidal synthesis are easily identifiable with IR spectroscopy.

IR spectroscopy is a very interesting tool when applied to colloidal synthesis of NCs. It is, in fact, possible to clearly identify the surfactants bonded to the surface of the nanocrystals. In some specific cases it is also possible to determine the type of surface bonding. For example using this technique, the interaction between the carboxylate head of a carboxylic acid and the metal atom on the surface of a NC has been categorized as four types: monodentate, bridging (bidentate), chelating (bidentate), and ionic interaction. [4]

3.7 Raman Spectroscopy

Similarly to IR spectroscopy, Raman spectroscopy is an experimental technique based on inelastic scattering of monochromatic light (usually from a laser source). The photons are absorbed by the sample and then re emitted. Frequency of the reemitted photons is shifted up or down in comparison with original monochromatic frequency, which is called the Raman effect.[5]

This shift, as in IR spectroscopy, provides information about vibrational, rotational and other low frequency transitions in molecules and vibrational modes in crystalline structures.

In Raman spectroscopy an incident photon of energy hv_0 can be inelastically scattered by the sample and loose some energy, promoting a specific

Raman-active vibrational mode of energy E_t. Thus the final energy of the photon will be lowered ($h\nu_0 - E_t$) and the new photon frequency is called "Stokes" (see figure 3.7). It can also happen that the sample is already in the excited state at the time of the interaction with the photon. In this case the excess of energy is released resulting in a scattered photon of energy $h\nu_0 + E_m$. The final photon's frequency, in this case is called "Anti-Stokes". This event is much less probable so the intensity of Anti-stokes lines is much lower (see figure 3.7).

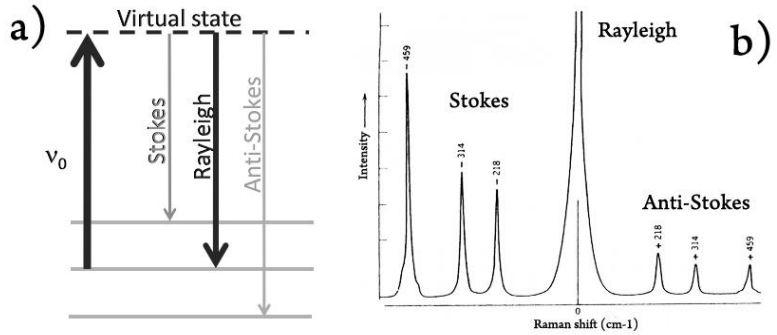

Figure 3.7 a) Schematic representation of (a) the energy levels involved in Raman spectroscopy. b) Example of a Raman spectrum collected for CCl_4 excited at 488nm. It's possible to note that the Anti-Stokes signals are much less intense than Stokes ones.

It is noteworthy to say that only about 0.001% of the incident light produces inelastic Raman. Spontaneous Raman scattering is very weak and special measures should be taken to distinguish it from the predominant elastic scattering (Rayleigh). Differently from IR spectroscopy, the polarization of the system must change for a vibration to be Raman active.

This technique works perfectly in recognizing specific crystal structures. Every structure has, in fact, specific crystal vibrations (phonons) at specific energies, so its Raman spectra can be used as a fingerprint of it. In colloidal synthesis Raman is thus a very important tool, complementary to XRD, for the identification of crystalline polymorphs in nanocrystalline samples.

3.8 Electron Paramagnetic Resonance (EPR)

Electron paramagnetic resonance (EPR) is a spectroscopy that is commonly used for studying paramagnetic materials. A material is called paramagnetic, if it has no macroscopic magnetic moment in the absence of an

external magnetic field, but in a magnetic field has one which points in the direction of the field. This can be understood by imagining that there are oriented microscopic magnetic dipole moments inside the materials that can align with the external field. For the occurrence of electron paramagnetism the existence of unpaired electrons inside the crystal structure is necessary. The excitation of electron spins and the observation of their resonance frequencies are the basis of EPR spectroscopy.

Every electron has a magnetic moment and spin quantum number. In the presence of an external magnetic field the magnetic moment aligns with the field in two ways: parallel and antiparallel. This produces a splitting of the energy levels (that in the ground state are degenerate) that is directly proportional to the magnetic field's strength. This phenomenon is known as Zeeman effect. At this point an unpaired electron can be excited from one energy level to the other absorbing or emitting an electromagnetic radiation of specific wavelength. Since there are more electrons in the lower energy state (due to the Maxwell-Boltzmann distribution), there is a net absorption of energy from the system.

In EPR experiments these absorptions are measured using microwaves in the region of gigahertz and magnetic fields of about 0.4 tesla. Crystal structures made of ions of the transition metals (belonging to the groups 3d, 4d, 5d, 4f and 5f of the periodic table) are normally studied in EPR experiments to see if there are "trapped" electrons inside the crystal structure. EPR is a powerful tool in studying the effect of n-doping structures such as metal oxides. It's in fact possible to understand if the external carrier introduced by the doping are free electrons rather than charged stuck on cationic sites.

3.9 Dynamic Light Scattering

Since the particle in a colloidal solution are moving with a Brownian motion we can follow their motion with a technique known as photon correlation spectroscopy or dynamic light scattering. A laser produces coherent light that is elastically scattered by a small volume of NCs in a dilute dispersion (figure 3.8a). Since the incident light is coherent the phase relationship is maintained. The colloidal particles behave like a random three dimensional diffracting array having therefore a random diffraction pattern. Since the particles are not only randomly distributed but also moving the relative pattern is moving too. If from the

detector we look at a small area defined by a small scattering volume, the bright diffractive spots move in and out of our vision at a rate that depends on the Brownian motion of the NCs (figure 3.8b). The detector (photomultiplier) is connected to a photon correlator and the intensity is measured over the time. Once the total time of the measurement is set the scattering intensity is recorded over a series of short time intervals until the total time is reached. Such time interval is called "correlation delay time", τ_c. At two of these times that are close together there is a strong correlation in the scattering intensities while for two intervals that are far this is not the case. The instrument constructs the correlation function comparing the scattering intensity at the beginning of the experiment to the ones measured in the short time intervals (figure 3.8c). The correlation function, $g(\tau_c)$, can be expressed:

$$g(\tau_c) = \exp\left(-\tau_c D_s Q^2\right)$$

where D_s is the self diffusion coefficient of the particles and Q is the modulus of the scattering vector.

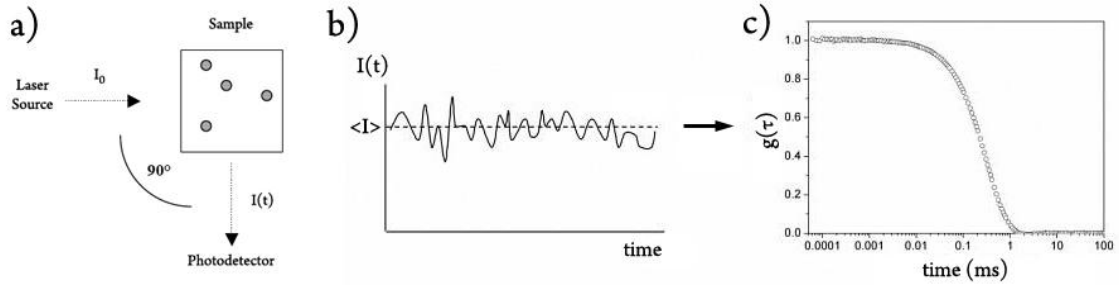

Figure 3.8 a) Schematic representation of a dynamic light scattering experimental setup. I_0 is the intensity of the incident radiation and I(t) is the scattering intensity due to moving particles. b) An example of I(t) and the corresponding autocorrelation function (c).

Plotting the data as natural logarithm versus Q^2 one obtains a straight line whose slope is intimately connected to the diffusion coefficient. The Stokes-Einstein relationship (as already seen before in chapter 1.5) is used to calculate the hydrodynamic radius, R_H, of the NCs:

$$R_H = \frac{k_B T}{6\pi\eta D_s}$$

If we a have a broad distribution of NCs the correlation function will be a sum of different exponential decaying terms weighted by the probability of each

time occurring. The intrinsic problem of this technique is that, in such a case, we cannot invert the summation obtaining a unique solution that describes our system. Supplementary models have to be taken into account in case of samples with a broad size distribution. In addition, as the intensity of the scattered light has been measured, the mean is weighted to the larger sizes.[2]

3.10 References

[1] C. B. Murray, C. R. Kagan and M. G. Bawendi, Synthesis and characterization of monodisperse nanocrystals and close-packed nanocrystals assemblies, *Annu. Rev. Mater. Sci.,* **2000**. 30:545–610

[2] Jim Goodwin, Colloids and Interfaces with Surfactants and Polymers, *John Wiley & Sons, **2004***.

[3] Emil Roduner, Size matters: why nanomaterials are different, *Chem. Soc. Rev.,* 2006, 35, 583–592.

[4] L. Zhang et al. / Applied Surface Science 253 (**2006**) 2611–2617

[5] L. Andrew Lyon et al., Raman Spectroscopy, *Anal. Chem.,* **1998**, 70, 341R-361R.

Warm White Light Project

4.1 Lights of the Future

The 20% of the global electrical energy is consumed for illumination. The development of efficient light sources to reduce energy waste is a now days challenge. Switching from conventional to solid-state lighting is essential for reducing the consumption of electricity and fossil fuels. Solid-state lighting in the form of light-emitting diodes (LEDs) is the most striking promise in meeting the challenge of saving energy. Currently white-light LEDs (WLEDs) can be found in a many applications, such as displays, internal lighting and flashlights. In order to achieve the full potential of WLEDs and make these systems competitive, advanced technologies must be developed to produce a high quality of white light that is highly efficient, has a long lifetime and cheap. The ideal WLEDs should emit a broad spectrum of light that would be similar to the sunlight. Most of the most efficient current WLEDs, however, emit a cool blue-like light not very appealing to the human eyes [1,2].

To evaluate the quality of the light emitted from WLEDs, several parameters, such as Commission Internationale de l'Eclairage (CIE) chromaticity coordinates, color rendering index (CRI), correlated color temperature (CCT) and luminous efficacy (LE) are used. The CIE coordinates (x,y) express precisely the emission color of the WLED, as perceived by human eyes. Color rendering is an essential figure of merit for a light source used in illumination applications. It is a

very common misconception that the color of an object depends only on the properties of the object. So, the true color of an object requires that we have a certain reference in mind. The CRI index is basically a quantitative measure of the ability of a light source to reproduce the colors of a variety of objects in contrast to an ideal or natural light source and it is expressed as a percentage. A high CRI value indicates that a light source will accurately render the colors of an object. Color temperature may appear to be a somewhat surprising quantity, as color and temperature would not seem to have a direct relationship with each other. However, the relationship is derived from Planck's blackbody radiator. The correlated color temperature is, then, the temperature in Kelvin (K) at which the heated black-body radiator matches the color of a tested light source. Low CCT indicates warmer (more yellow/red) lights, while high CCT implies cooler (more blue) lights. Finally the LE of a light source is a key metric for energy savings considerations. The luminous efficiency is expressed in lumens per watt and it expresses the total luminous flux divided by the total lamp power input. The desirable light source in color-critical applications should have a high CRI, CIE coordinates close to (0.33 , 0.33) (that correspond to the "perfect white"), CCT values from 2500 to 4500 K (warm white) and high LE.

As regarding the materials of the future WLEDs, organic molecules provide the advantage of low-cost fabrication for large-area light emitting panels (thanks to the ink-jet technology), but they are unfortunately not very efficient, the lifetime is short and the quality of emitted colors is low. Inorganic materials seem to overcome the problems of organic ones offering good luminescent properties combined with improved lifetimes. For example inorganic phosphors, phosphorescent materials made of optically active rare-earth atoms embedded in an inorganic matrix, are commonly used modern in lighting devices. As an example Cesium-doped yttrium aluminum-garnet $Y_3Al_5O_{12}:Ce^{3+}$ (YAG) is a common yellow phosphor. The problem of conventional phosphors is the poor tunability of color emission and the necessity of a relative high amount of material to achieve good absorption and thus emission of light (this is because the absorption/emission occurs only on the rare-earth atoms sites). Finally while high efficient yellow phosphors are readily available, the efficiency of red phosphors still lags. On the other hand QDs have their emission colors tuned by simply altering the nanocrystal size (or in some cases the composition) with very high quantum efficiency, making them attractive candidates for applications in solid-state lighting. Moreover semiconductor nanocrystals are easily processable through surface functionalization, and they show high resistance to photo-

oxidation and thus long lifetimes. That's why the integration of NCs like quantum dots is leading the modern research on lighting systems.

4.2 Lighting Devices

WLEDs used in modern lighting devices be divided in three categories: a) discrete color mixing, b) color conversion, and c) direct white light generation [1,2].

4.2.1. Discrete Color Mixing

One intuitive approach for achieving white light is to optically mix several colors of electroluminescent emissions (e.g., red, green, cyan and blue) of semiconductors in the desired ratio (see fig 4.1).

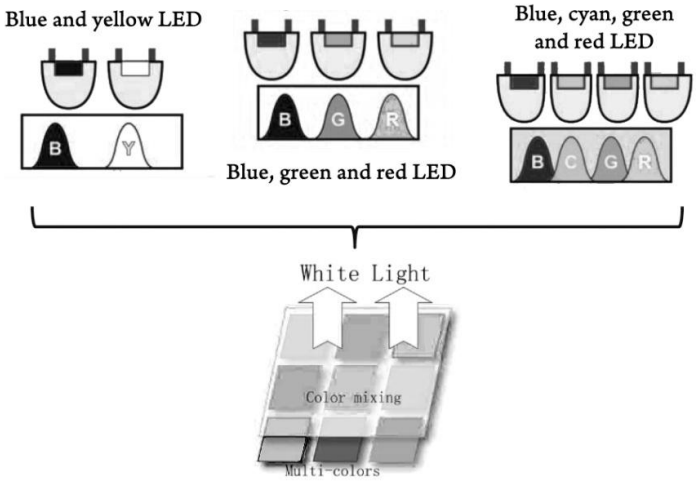

Figure 4.1 Figure x. Schematic representation of "color mixing" WLEDs: Different LEDs or QDs emitting red, green, cyan and blue light are mixed to give white light.

For example a mixture of blue-, green-, cyan- and red-emitting LEDs or electroluminescent QDs (made mainly with CdS, CdSe, ZnSe and ZnS) have been shown to work perfectly to produce white light. This approach could potentially provide a general route to prepare long-lifetime devices but it has to face several challenges. Unfortunately the emission power, peak wavelength and spectral width of semiconductor materials vary with temperature. LED emission powers decrease exponentially with temperature; low-gap red LEDs are particularly sensitive to ambient temperature. As a result, the chromaticity point, correlated

color temperature, CRI, and efficiency of LED-based light sources drift as the ambient temperature of the device increases. Moreover, working with QDs instead of LEDs, it is quite complicate to always maintain the appropriate fractions of the different population of QDs. A slight change in the mixing proportions makes it impossible to reproduce the same quality of white light. Furthermore, even when the ratio of the three populations of QDs remains constant, a change in the whole solution concentration can alter the final emitted color.

4.2.2. Color-Conversion WLEDs

In color-conversion WLEDs, blue (or UV) LEDs are used as light sources. This "high energy" source is then partially (or totally in case of UV source) converted (photoluminescence) by a layer of QDs or phosphors into warmer colors (like green, yellow or red) (see figure 4.2).

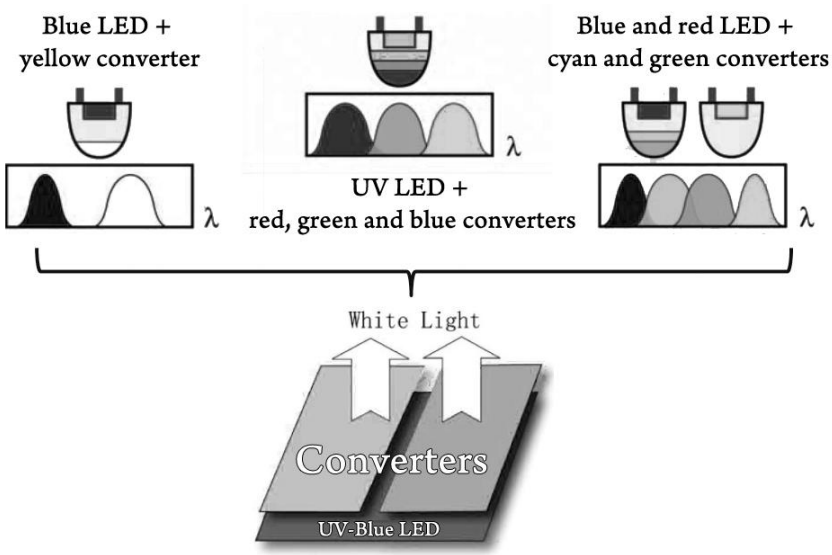

Figure 4.2 Schematic representation of "color conversion" WLEDs: If a blue led is used as light source, a part of the blue light is converted into other colors by QDs or phosphors. The sum of the blue and other components produces white light. If a UV source is used, the converters absorb all the light emitting different colors that mix to give white light. The color is "generated" within the chip and the epoxy case.

Such color-conversion layers are normally deposited directly onto the LED chip using epoxy resins as polymer matrix. The color-conversion technique employing phosphors is now days is the cheapest and so the most commercially exploited. Devices that use phosphors have great color stability and do not suffer from the strong change in chromaticity and color rendering. This is because the

intra–rare-earth atomic transitions occurring in phosphors do not depend on temperature. However, it is still hard to control the composition of phosphor layers and subsequently deposit uniform films, thus causing the undesired visible color variations. Additionally, at the moment it is impossible to tune the photoluminescence of phosphors, which makes it difficult to get a warm white light. That's why as an alternative to phosphors, QDs have been lately considered for the color-conversion layers. As in color-mixing strategy the nanocrystals that have been tested are mostly Cd-based and even if the control over the optical properties of these QD is high it is still difficult to achieve a CRI over 85 (a warmer light). Some recent reports have demonstrated that excellent CRI values could be achieved by combining conventional phosphors and semiconductor nanocrystals. These results indicate that the combination of both QDs and phosphors with blue LEDs can be a wonderful solution to create warm white light. Unfortunately the main disadvantage to this approach is the "self-absorption" of semiconductor nanocrystals, which dramatically reduces the overall device efficiency. A large fraction of the emitted light from a population of QDs with higher bandgap is likely to be absorbed by either the nanocrystals themselves (in a low amount) or the neighbouring nanocrystals with lower bandgap (in a high amount). For instance, the emissions from the blue-emitting nanocrystals would be significantly absorbed by the green- and red emitting ones. Moreover, the vicinity of the semiconductor QDs to the LED chip (that heats up while in use) can lead to unpleasant changes in chromaticity of the WLED due to thermal effects. This effect is due to the fact that the color is "generated" within the chip and the epoxy case where the nanocrystals are dispersed.

4.2.3. Direct White-Light WLEDs

Direct white-light generation can be imagined as particular color converting setup. In this case a UV LED source is used to excite the photoluminescence of only one type of nanocrystals that can emit white light. Special QDs with a very broad emission are employed for this technique. For example direct white light was achieved using ZnSe nanocrystals with both energy band blue emission and broad surface green/red emission. Similarly, the broad surface-state emissions and band-edge emission from 1.5-nm "magic sized" CdSe nanocrystals (unfortunately with a quantum yield of 2%) was tested in these systems. Fluorescent ZnO–SiO_2 composite nanopowders showing broad emission spectra were successfully exploited to fabricate highly bright WLEDs. Additionally, metal ion-doped nanocrystals, such as ZnS:Pb^{2+},Si-doped ZnS, Mn^{2+}-doped ZnS and Mn^{2+}-doped CdS are new promising systems for the direct generation of white light. In

contrast to the undoped counterparts, these NCs have the potential to overcome some intrinsic disadvantages such as: self-absorption and poor stability under thermal, chemical and photochemical disturbances. While the high CRI values and the good CIE coordinates obtained with all these systems are extremely promising the related WLEDs have very low luminous efficiency (1.0 lm/W), and the stability of optical properties needs further improvement.

4.3 "Warm white light" project

The aim of this PhD project, also called "warm white light project", is to propose an alternative solid state lighting device that works using the same principles of color-conversion WLEDs. The idea is to create a polymer based nanocomposite that could work as a transparent glass in off-mode and as a "lamp" in on-mode. The new concept is to spatially decouple the light source and the converters in order to avoid all the thermal problems that affect the current LEDs (in which the color is "generated" within the chip and the epoxy case). To do so, a blue LED, made of Indium gallium nitride (InGaN), is coupled to a bulk polymer nanocomposite sheet where the actual conversion of light takes place as depicted in figure 4.3. For emitting white light it is necessary that the nanocomposite would not only convert partially the blue light into warmer colors (like yellow and red) but also diffuse the blue light outside in order to have a color mixing.

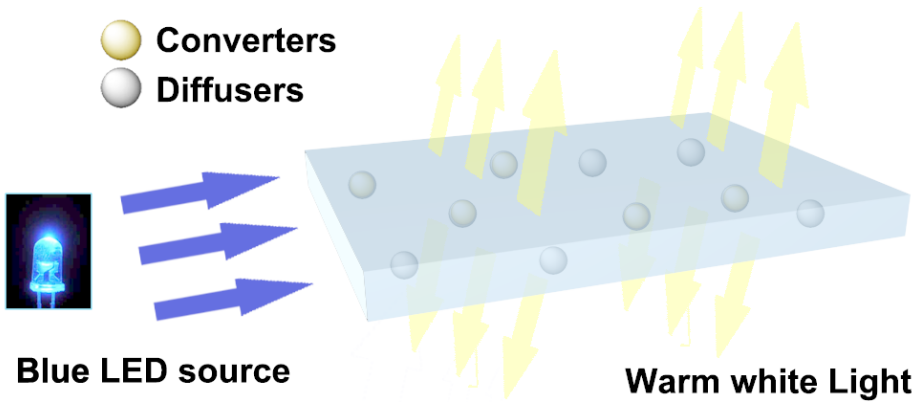

Figure 4.3 Sketch of the final lighting device. A blue LED is used as light source. The light is partially diffused and partially converted by the bulk polymer nanocomposite, resulting in a warm white light. In off mode the device appears as a transparent polymer.

The polymer matrix will be poly methyl methacrylate (PMMA), well known material that has two main advantages: it is highly transparent and it has very low oxygen permeability. PMMA transmits up to 92% of visible light (3 mm thickness), and gives a reflection of about 4% from each of its surfaces on account of its refractive index. This transparency can be achieved by bulk polymerization of methyl methacrylate. This kind of process, if well controlled, is able to avoid the formation of undesired air bubbles and internal strain (defects that would lower the transparency of the material due to light scattering).

The choice of the blue LED chip is mainly due the low cost and the very high efficiency of such device. Moreover, as explained before, the blue light is suitable for both exciting the converters (that emit at lower energies than blue) and also for participating in the final emission of white light.

We decided to use TiO_2 NCs as diffusers exploiting the Rayleigh scattering. Rayleigh Scattering is an elastic scattering process that occurs when the scattering objects are small compared to the wavelength of the incident light. The amount of scattering that occurs for a beam of light depends mainly upon the size of the particles and the wavelength of the light. Specifically, the intensity of the scattered light (I_s) depends on the particles size (d), their refractive index (n) and on the wavelength of the incident light (λ) as follow:

$$I_s \propto \frac{d^6}{\lambda^4}\left(\frac{n^2-1}{n^2+2}\right)^2$$

The choice of TiO_2 NCs is thus easily understandable if we think about the advantages of having a high refracting index material with dimensions much smaller than the wavelength. Titanium oxide NCs are not only perfect scattering objects but they are also "transparent" in the visible light spectral range due to the large bandgap of the material itself. Commercially available TiO_2 NCs (T805 Aldrich), already surface modified with octyl silanes, could be used for this purpose. Unfortunately the commercially available products contain many big aggregates creating problems in obtaining well controlled NCs dispersions. A low cost synthesis of colloidal TiO_2 NCs is then necessary in order to have a full control over the scattering properties of the final polymer nanocomposite.

Eventually we decided to use non toxic QDs as converters in our system. Trying to overcome the problems related to the current phosphors, our idea is to use quantum dots that could absorb the blue light and emit warmer wavelength

such as yellow, orange and red. At first the use of QDs instead of phosphors is due to the possibility of precisely tune the emission of the converters. Moreover, while the current phosphors have micrometric dimensions, these nanocrystals are normally in the range of few nanometers. If the quantum efficiency of the QDs is high enough it's, in principle, possible to achieve a good conversion of the blue light with a very low concentration of such converters. This would lead to a reduced waste of materials and at the same time would allow the final composite to be transparent in off mode. The same couldn't be achieved using phosphors due to their big dimensions and thus high scattering of light.

4.4 Quantum Dots for Solid-State Lighting Devices

As shown up to now QDs are very promising materials for solid state warm white light devices. The widespread use of Cd based QDs is a testament to their excellent size-dependent optical properties in the visible range. For fundamental studies, CdSe nanocrystals have served as an excellent model system. However, cadmium, an extremely toxic component, makes future use of this type of nanoscaled candidate uncertain in practical applications. It is well known that cadmium is a highly toxic element, any potential release of which is considerably harmful to the environment and mankind. Eventually, the inherent toxicity of cadmium-related nanomaterials will prevent their applications to the increasing WLED market and other related fields. Therefore, the engineering development for large-scale production of nontoxic, user-friendly, and environmentally benign nanomaterials is needed, where non-cadmium nanocrystal-based WLEDs will be the priority. In response to this requirement, nontoxic InP/ZnS nanocrystals with high emission efficiency in the visible range might be a good substitute for CdSe nanocrystals. $CuInS_2$ and $AgInS_2$ also have been proposed as alternatives with optical properties comparable to CdSe nanocrystals. These materials might be acceptable for real-world applications because of their non-toxicity and environmental benignity.

The experimental part of this PhD will be mostly focused on the synthesis of these new emerging materials. The obtained NCs will be then studied and then, eventually, embedded in a polymer matrix of PMMA. These final nanocomposites would be the first prototypes for "warm white light project" devices.

4.5 References

[1] Quanqin Dai, Chad E. Duty, and Michael Z. Hu, Semiconductor-Nanocrystals-Based White Light-Emitting Diodes, S*mall*, **2010**, 6, No. 15, 1577–1588.

[2] E. Fred Schubert and Jong Kyu Kim, Solid-State Light Sources Getting Smart, *Science*, **2005**, 308, 1274.

Indium Phosphide/Zinc Sulfide (InP/ZnS) Core-Shell QDs

5.1 Introduction

As mentioned in the previous chapter, recently, colloidal III-V semiconductor nanocrystals (NCs) have attracted intense interest owing to their less ionic lattice, larger exciton diameters, and, most of all, because of their reduced toxicity compared to II-VI compounds. Moreover a big advantage offered by III-V semiconductor nanocrystals lie in the strength of the covalent bond (versus the ionic bond in the II-VI semiconductors) that makes these systems robust and so adapt for in-vivo applications [1-7]. Among III-V semiconductors, InP is probably the only one which could offer a compatible emission color range similar to that of Cd-based QDs but without intrinsic toxicity since InP has neither Class A elements (Cd and Hg), nor Class B elements (As and Se)[2,5]. Indium phosphide has, in fact, broad size-tunable emission in the visible and near-infrared spectral range due to its bulk band gap of 1.35 eV [4]. Nevertheless, the study and applications of III-V semiconductor nanocrystals are limited by the difficulty in their synthesis. Presumably due to their covalent-bond character, the synthesis of InP QDs often suffers from long reaction times or an uncontrollably fast nucleation that follows by the formation of amorphous or bulk compounds [2,3]. Existing problems surrounding InP QDs include poor emission efficiency, poor control of size distribution, poor size tenability, and/or poor

stability. Furthermore, the synthetic procedure of InP NCs is more complicated than that for CdSe nanocrystals [5]. So, until now InP NCs synthesized by current chemical methods did not achieve the same quality as that of most II-VI semiconductor NCs [1].

Colloidal InP QDs are normally synthesized by the injection of precursors into a hot solution of surfactants. In these reactions, Indium(III) carboxylates, react with tris(trimethylsilyl)phosphine, $P(TMS)_3$, at elevated temperatures to produce trimethylsilyl-carboxylate and InP QDs [1,3-5]. The In:P precursors ratio that optimizes the crystallinity of InP NCs has been found to be 2:1. The common coordinating solvents, ligands for II-VI systems, and the similar precursors do not work well for the synthesis of III-V semiconductor NCs. So the syntheses of InP are mostly carried out in non coordinating solvents, and it is still a challenge to develop a rapid reaction approach in coordinating solvents [3,5].

The role of our work is to explore the reported InP synthesis and to further improve the luminescent properties of these systems. In order to increase the quantum yield of these NCs a shell of ZnS will be grown. To the best of our knowledge the syntheses that seem to give the best results can be divided in three categories: a) high temperature, b) polyethylene glycol (PEG) "assisted", and c) amine assisted. So our work will start from these ones.

5.2 High Temperature Route

Following other works [6-7] we tested the optical properties of InP obtained at "high temperature", 300°C. In a typical synthesis Indium acetate, $In(ac)_3$, (0.4mmol) was mixed with a desired amount of myristic acid, MA, and octadecene (ODE) (25ml) in a three neck flask. The mixture was heated at 120°C under vacuum for 1h until a clear solution was obtained. The system was then purged with N_2 and further heated to 300°C. $P(TMS)_3$ (0.2 mol) was dissolved in ODE (2ml) in a glove box and injected into the hot flask. After the injection the temperature was set to 270°C to let the InP NCs grow for 5 minutes. The reaction was then quenched lowering the temperature of the flask to room temperature. The nanocrystals were cleaned adding ethanol to the reaction solution and centrifuging for 10 minutes at 3000rpm. The QDs were redispersed in toluene and precipitated with ethanol for three times.

It has been shown [6-7] that the amount of the carboxylate group is fundamental for tuning the reactivity of the indium precursor, so different In:MA ratios were used during the synthesis ranging from 1:2 to 1:4. While using a In:MA=1:2 no fluorescent product was collected, working with 1:3 and 1:4 ratios red emitting QDs were synthesized as shown in figure 5.1.

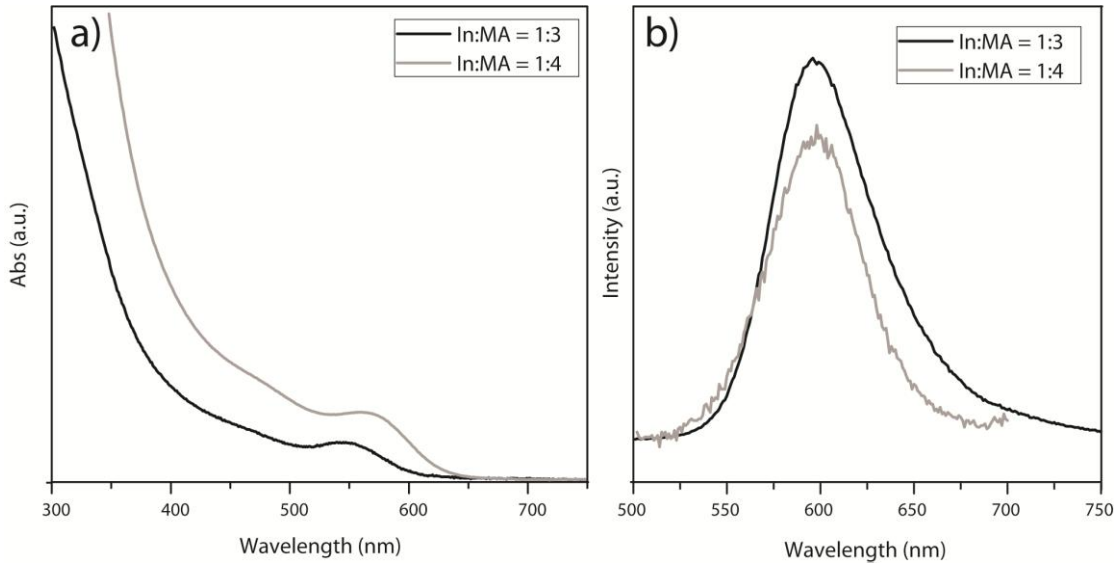

Figure 5.1 a) UV-Vis absorption spectra of the InP samples obtained using In:MA ratios of 1:3 and 1:4. In panel b) the corresponding photoluminescence spectra are presented. (λ_{ex} = 400nm)

As it is possible to appreciate from figure 5.1a) the samples don't seem to be polydisperse showing a marked absorption edge. Increasing the amount of MA the particles get bigger (the absorption edge moves to lower wavelength). This is probably due to the steric hindering that the carboxylate groups produce. At higher amount of MA the precursors are less consumed during the first nucleation burst and so the NCs formed at the early stages can further grow by monomers addition. Unfortunately these systems seem to be more defective yielding to a lower photoluminescence (PL) (see figure 5.1b).

A ZnS shell was grown on the QDs showing the best PL (In:MA=1:3) to increase the emission efficiency. In a typical shell synthesis, after quenching the InP synthesis, the reaction solution was heated at 120°c. A solution of diethyl zinc, Et_2Zn, (0.3mmol), bis(trimethylsilyl)sulfide, BTS, (0.3 mmol) and trioctylphosphine, TOP, (1ml), prepared in glovebox, was added drop by drop to the flask. The temperature was then raised to 200°C for 70 minutes to let the shell grow. The NCs, as before, were cleaned using toluene as solvent and ethanol as anti-solvent for three times.

The PL was strongly enhanced by the growth of the ZnS shell (see figure 5.2).

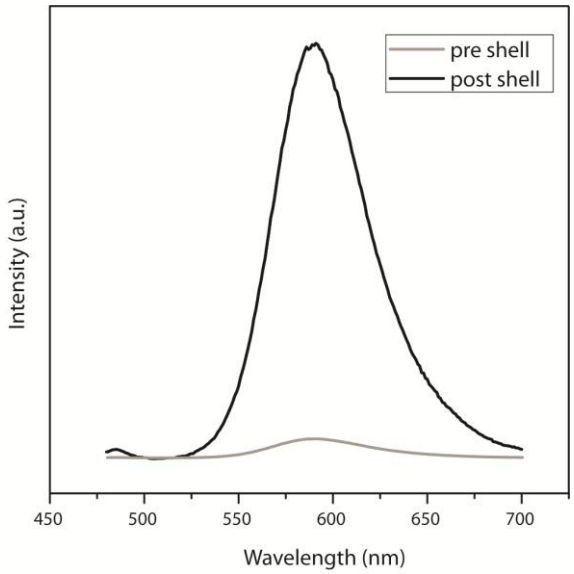

Figure 5.2 PL spectra of the InP sample grown using In:MA=1:3 before and after the growth of a ZnS shell. The samples were excited using (λ_{ex}=450nm).

The PL QY was unfortunately very low (in the order of 2%) as measured in comparison with Rhodamine 6G. Moreover the tunability of the emission was very low and, typically, even quenching the reaction just after the injection, a red emitting QDs were achieved. Thus this synthesis didn't seem to be promising for our purpose and so was discarded.

5.3 PEG "Assisted" Synthesis

In a quite recent work of Sungjee Kim and others [2] a polar and weakly coordinating solvent (instead of the typical non-coordinating ones) was used in order to have a better control over the crystallinity of InP NCs. In their paper they claim that higher polarity provides a better solubility and homogeneity of the precursors, which leads to rapid and controlled reactions that can be performed at lower temperature. They selected polyethylene glycol (PEG, MW=1500–4000) as an ideal solvent for InP NCs synthesis. This solvent is weakly coordinating through the terminal -OH group, which is able to activate In–carboxylate and $P(TMS)_3$ precursors. The polymer is also nontoxic, relatively inexpensive and easily recyclable.[2]

Following this work we tested the optical properties of InP obtained using PEG as solvent. In a typical synthesis Indium acetate, $In(ac)_3$, (0.4mmol) was mixed with myristic acid, MA, (1.7mmol) and PEG (4g) in a three neck flask. We decided to use PEG with a MW of 1500 rather than 400 or 4000. That's because using a low molecular polymer the solubilization of the In precursors and MA was not possible, while using PEG 4000 the whole solution was too viscous. The mixture was heated at 150°C under vacuum for 1h until a clear solution was obtained. The system was then purged with N_2 and kept at 150°C. $P(TMS)_3$ (0.2 mol) was dissolved in TOP (0.5ml) in a glove box and injected into the hot flask. The InP NCs were grown at 150°C for the desired time. The reaction was then quenched lowering the temperature of the flask to 120°C. A solution of diethylzinc, Et_2Zn, (0.3mmol), bis(trimethylsilyl)sulfide, BTS, (0.3 mmol) and trioctylphosphine, TOP, (1ml), prepared in glovebox, was added drop by drop to the flask. The temperature was then raised to 200°C for 70 minutes to let the shell grow. The nanocrystals were cleaned adding ethanol to the reaction solution and centrifuging for 10 minutes at 3000rpm. The QDs were redispersed in toluene and precipitated with ethanol for three times.

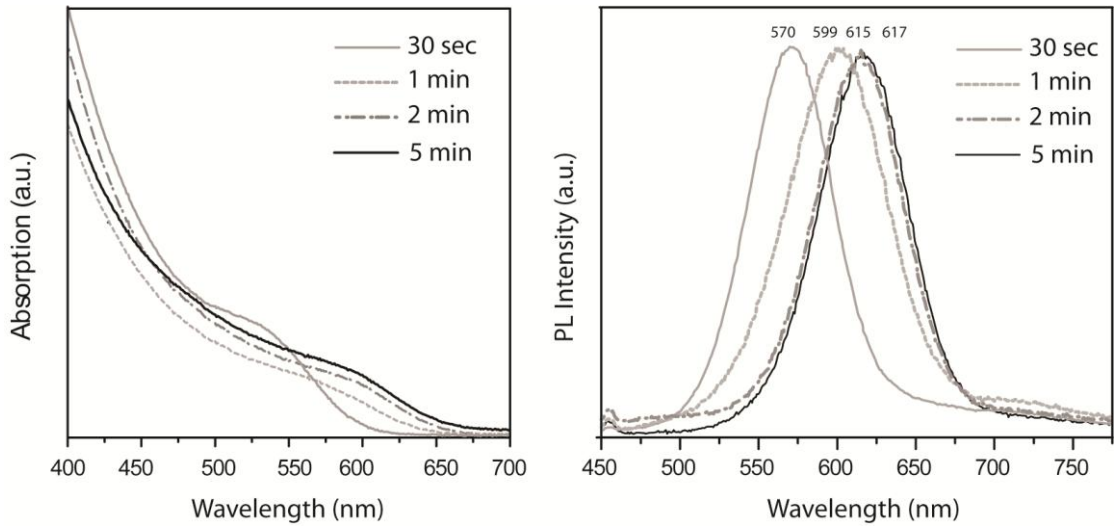

Figure 5.3 UV-Vis absorption spectra (left) and PL curves (right) of InP/ZnS core-shell samples obtained at different growth times. (λ_{ex} = 400nm) It's clear how the absorption and emission move to lower energies increasing the reaction time.

The PEG assisted route allowed for the tuning of the photoluminescence from 570nm to 617nm just varying the reaction time, as shown in figure 5.3. Using this strategy green or blue emitting QDs seemed to be precluded. Increasing the reaction time, unfortunately, the amount of side products/big aggregates increased leading to a lower reaction yield. The use of PEG brought many

problems in the cleaning step. This polymer is solid at room temperature and hardly soluble in a mixture of toluene and ethanol. Unfortunately, also in this case, the obtained QDs didn't show high luminescence and the QY was never higher than 5%.

5.4 Amine "Assisted" Synthesis

To make In carboxylate species reactive enough for the formation of InP at low temperatures, activation reagents would be needed. Fatty amines have been known as common activation reagents and good ligands for improving emission properties of II-VI QDs. Furthermore, amines have been shown to play an important role for the efficient growth of ZnS shell on the surface of InP NCs [5]. For lowering the reaction temperature only fatty amines with a short hydrocarbon chain seem to work in InP synthesis. Lowering the reaction temperature not only can lead to a better control over the growth of InP NCs but also suppress the formation of In_2O_3 (that forms at high temperatures)[5]. The amine "assisted" synthetic scheme developed for InP QDs at relatively low temperatures is quite similar to those developed for CdSe nanocrystals including the solvent, ligands, precursors, and no necessary thorough degassing.[2,5]

Following others' works [2,5] we devised a synthesis of InP NCs as follows. In a typical synthesis Indium acetate, $In(ac)_3$, (0.4mmol) was mixed with the desired amount of myristic acid, MA, and ODE (4g) in a three neck flask. The mixture was heated at 120°C under vacuum for 1h until a clear solution was obtained. A solution of $P(TMS)_3$ (0.2 mol), octylamine (OA) in a desired amount, and ODE (1.5ml) was prepared in a glove box and injected into the reaction flask at 180°C. The InP NCs were grown at 180°C for the desired time. The reaction was then quenched lowering the temperature of the flask to 120°C. A solution of diethylzinc, Et_2Zn, (0.3mmol), bis(trimethylsilyl)sulfide, BTS, (0.3 mmol) and trioctylphosphine, TOP, (1ml), prepared in glovebox, was added drop by drop to the flask. The temperature was then raised to 200°C for 70 minutes to let the shell grow. The nanocrystals were cleaned adding ethanol to the reaction solution and centrifuging for 10 minutes at 3000rpm. The QDs were redispersed in toluene and precipitated with ethanol for three times.

Keeping the amount of In precursor, solvent and P precursor fixed we varied the quantity of MA and OA in order to study the effects on the synthetic

results. For a fixed amount of OA, (1.95mmol), we increased the amount of MA from 1.7mmol to 2mmol. As already observed in the "high temperature" route, the nucleation of NCs seemed to be gradually hindered so that the particles could further grow during the growth step (see fig. 5.4). As it is possible to observe in figure 5.4a, using less MA (1.7mmol) the particles didn't seem to grow much after the injection and the absorption peak slightly shifted from 430nm to 465nm after 3 minutes. After that time the peak didn't move further to the red and it got broader indicating the occurrence of a polydisperse sample. Using higher amount of MA (2mmol) the growth of the QDs seemed to be more controlled and the absorption peak moved from 490nm to 610nm. The absorption edge didn't broaden but a second absorption shoulder started to appear already after 4 minutes. A second population of smaller QDs probably nucleated in a second step.

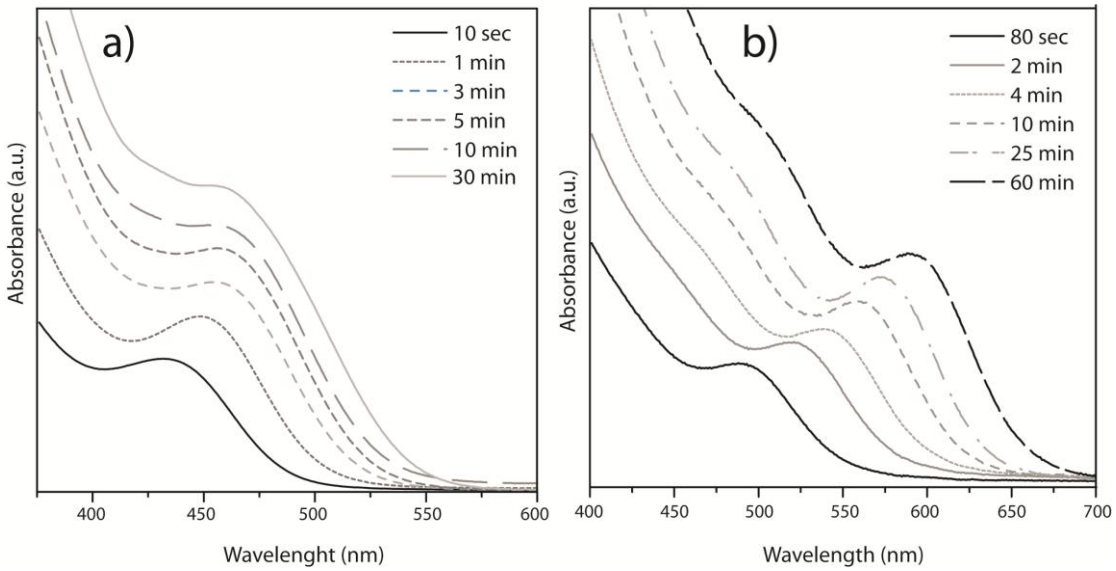

Figure 5.4 Absorption spectra of InP QDs grown using different amount of MA: 1.7mmol (a) and 2mmol (b). It is possible to see how the absorption edge moves to the red during the reaction time indicating the growth of the NCs.

Unfortunately it was not possible to monitorize the photoluminescence these systems during the growth of QDs. This was because no light emission was observed without a further growth of a ZnS shell. This indicated that the defective surface states on the bare InP NCs played an important role in the optical properties of these systems.

For a fixed amount of MA, (1.7mmol), we varied the amount of OA from 1 mmol to 2.4 mmol. Using 1 mmol of OA (figure 5.5a) two populations of NCs were easily distinguishable already after 1 min. Two absorption shoulders

appeared in the absorption spectra, moving toward low energies as the reaction times increased. Increasing the amount of OA to 2.4 mmol (figure 5.5b) a similar behavior to what observed before (figure 5.4a) occurred. The particles didn't grow much after the initial nucleation and the absorption peak moved slightly from 430nm to 450nm. In this case the particles grew less than what observed using 1.95mmol of OA.

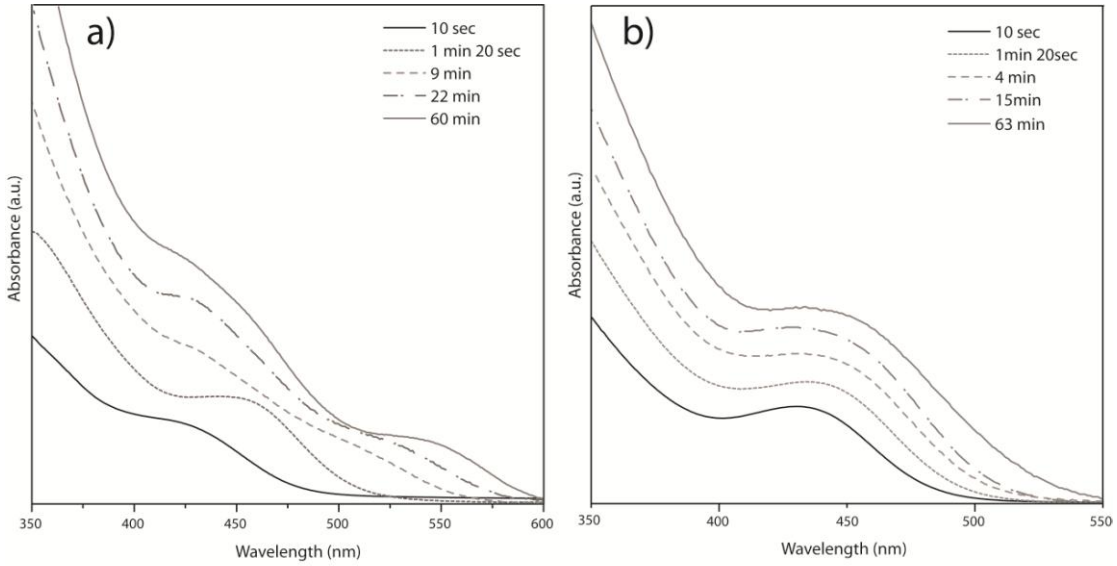

Figure 5.5 Absorption spectra of InP QDs synthesized using a fixed amount of MA, (1.7 mmol) and varying the amount of OA: a) 1mmol and b) 2.4mmol.

The synthetic route that worked best was employing 1.7mmol of MA and 1.95mmol of OA even if a poor control over the dimension was achieved. Varying the reaction time from 6 to 9 minutes, it was possible to tune the luminescence of InP/ZnS QDs from green/yellow (530nm) (QD1), to yellow (540nm) (QD2) as shown in figure 5.6. Unfortunately increasing the reaction time no further red shift was achieved.

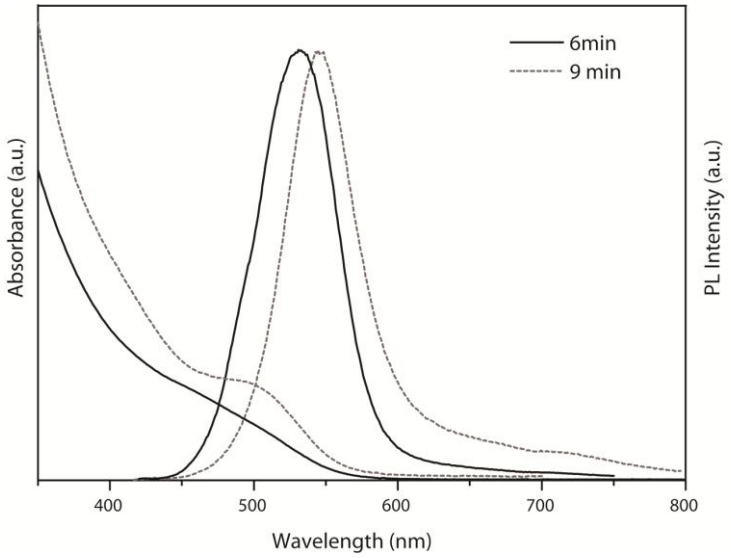

Figure 5.6 UV-Vis absorption and PL spectra of InP/ZnS QDs obtained using 1.95mmol of OA and 1.7mmol of MA varying the reaction time from 6min (QD1) to 9 min (QD2). (λ_{ex} = 400nm)

The only way we found to increase the size of our NCs and to shift the color emission to lower energies was a multiple injection of precursors. This strategy, often applied for II-VI systems, allowed for a further growth of our NCs pushing the photoluminescence up to the orange/red (580nm) (QD3). In a typical "multiple injection" synthesis Indium acetate, $In(ac)_3$, (0.4mmol) was mixed with the desired amount of myristic acid, MA, and ODE (4g) in a three neck flask. The mixture was heated at 120°C under vacuum for 1h until a clear solution was obtained. A solution of $P(TMS)_3$ (0.2 mol), octylamine (OA) in a desired amount, and ODE (1.5ml) was prepared in a glove box and injected into the reaction flask at 180°C. After 4 minutes of growth at 180°C a solution of $P(TMS)_3$ (0.2 mol) and ODE (1ml) (prepared in a glove box) was added drop by drop to the reaction flask. The NCs were let to further grow for the desired time at 180°C. The reaction was quenched lowering the temperature to 120°C and subsequently a ZnS shell was grown following the usual procedure (see above). Figure 5.7 shows the evolution of the UV-Vis absorption spectrum of the growing InP particles and the PL emission of the final InP/ZnS QDs.

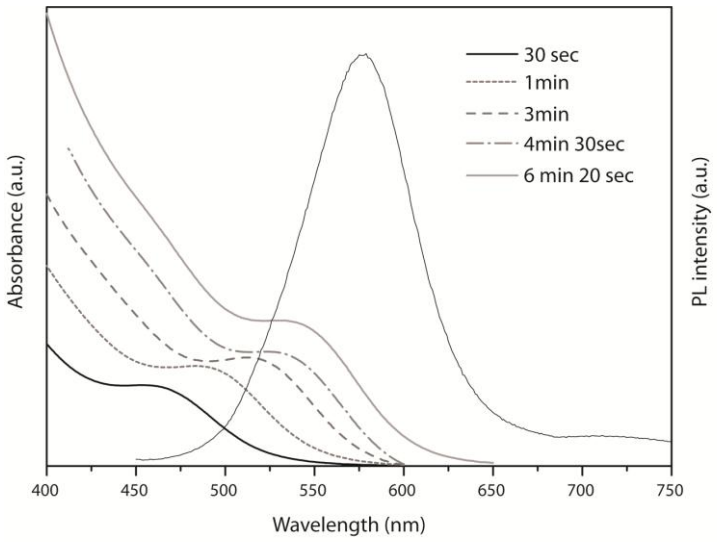

Figure 5.7 Evolution of the UV-Vis absorption of InP NCs grown with the "multiple injections" route. It's possible to notice how the absorption edges moves further to lower energies after adding the extra P precursor (after 4 min). The PL of the final InP/ZnS QDs obtained is also shown (QD3). (λ_{ex} = 400nm)

Since In and P precursors strongly react also at room temperature it was not possible to add both in the second "injection" step. We found out that the only way to increase the size was the injection of just $P(TMS)_3$ exploiting the fact that in the initial reaction the In:P ratio was 2:1.

The QY of the samples QD2 and QD3 was measured to be as high as 50% and 43% respectively.

5.5 InP/ZnS-PMMA Bulk Polymer Nanocomposites

The samples QD2 and QD3 were chosen to be integrated into a PMMA matrix in order to produce polymer nanocomposites for the "warm white light" project. For the synthesis of bulk nanocomposites a desired amount of QDs was added to a 10^{-3}M solution of Azobisisobutyronitrile (AIBN) in methyl methacrylate (MMA) and the resulting mixture was heated to 60°C under N_2 for 36 hours. The resulting bulk solid composite was further heated at 95°C for 12 hours for the curing process.

Unfortunately no luminescence was observed in the final polymer nanocomposites. In order to investigate the reason for the quenching of our systems we first prepared a solution of QDs in MMA without adding the radical initiator and we heated up the whole dispersion for 36h under N_2. The resulting liquid mixture exhibited fluorescence indicating that the temperature, or the potential ligand exchange with, MMA were not the causes of the quenching during the polymerization process. The QDs in toluene were exposed to AIBN at 60°C to examine the effects of the radical initiator on the optical properties of our systems. As reported in figure 5.8 the luminescence of our systems decreased during the exposure to the AIBN radicals until a total quenching was observed after several hours. As it is possible to notice in figure 5.8, during the exposure to radicals, the main PL peak at 540nm decreased and the emission due to the surface states (lower energies) increased dominating the whole PL spectrum after 6 hours. The effect of the radical initiators was probably to produce an etching of the QDs' surface, opening new defective-non ricombinative decay channels for photogenerated carriers. The same happened employing other radical initiators such as benzoyl peroxide or lauryl peroxide.

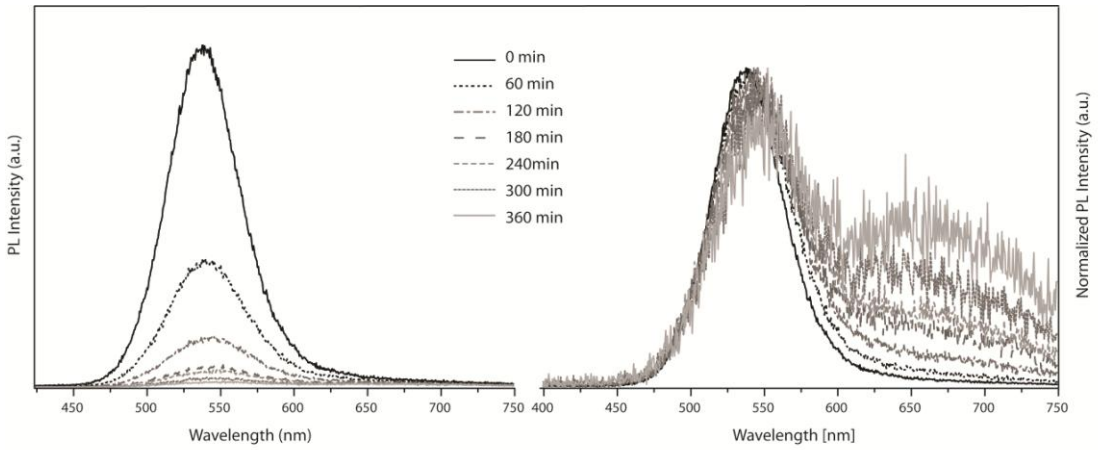

Figure 5.8 (left) Time-integrated PL spectrum the sample QD2 during its explosion to AIBN at 60°C at several times. (right) The same PL normalized at the main emission peak @ 540 nm (λ_{ex} = 400nm).

Bulk nanocomposites of PMMA-InP/ZnS QDs were consequently discarded as possible solution for our project.

5.6 InP/ZnS-PMMA Thin-Films

Since these QDs cannot withstand the attack of radical initiators a film casting procedure was used in order to achieve polymer based nanocomposites. A solution of a desired amount of QDs in toluene (1.8 10^{-4} M for the sample QD2 and 1.2 10^{-4} M for QD3) was mixed directly to 20ml of a solution of PMMA in toluene (20%w/w) and stirred at room temperature until a clear solution was obtained. Doctor blade (also called tape casting) technique was adopted for producing thin films on large area surfaces from the prepared solutions.

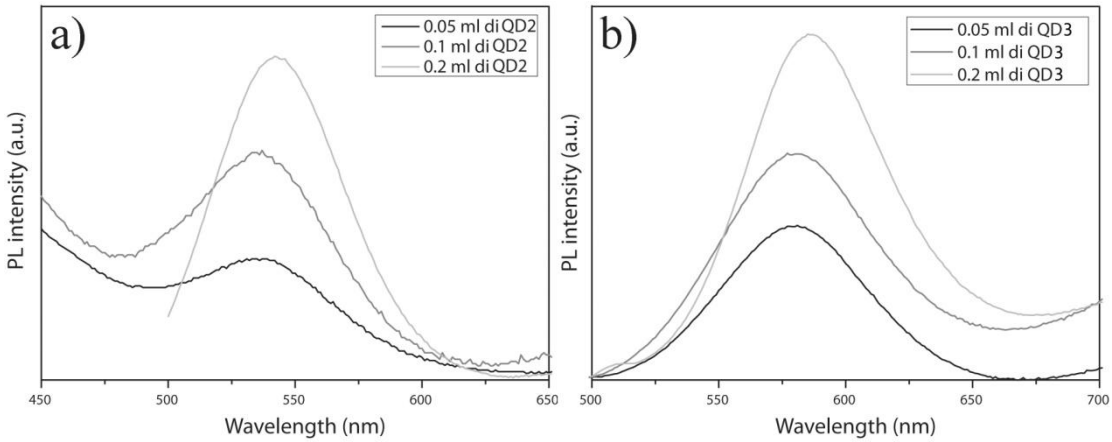

Figure 5.9 Photoluminescence spectra of the films obtaines using 0.05 ml, 0.1 ml and 0.2 ml of a) QD2 and b) QD3 in 20 ml of polymer solution (λ_{ex} = 400nm) .

After the evaporation of the solvent the resulting nanocomposite films exhibited fluorescence as reported in figure 5.9. These systems are now under study, further characterizations are necessary to understand the properties of the obtained nanocomposite films. The idea is, in case, to exploit these systems as "covering layers" of the main bulk polymer sheet in order to separate the scattering event (that would occur just in the polymer sheet charged only with TiO_2 NCs) from the conversion "step". If these films were used, the conversion would occur in the composite film deposited on the external surfaces of the polymeric bulk object.

5.7 Conclusions

InP/ZnS Core-Shell QDs were synthesized following three different main strategies. Among them the most promising route was the "amines assisted" one

that allowed for the production of yellow and orange emitting QDs with a QY as high as 50%. Unfortunately these systems were shown to be quiete weak and couldn't sustain a bulk polymerization process. The radical initiator was found to be resposible of the quenching of these QDs producing non radiative surface states. A tape casting technique was, then, adopted for producing thin InP/ZnS-PMMA nanocomposite films that could be used as converting layers in the warm white light project. Further characterizations are still necessary in order to find real applications of these films.

5.8 References

[1] Peter M. Allen, Brian J. Walker, and Moungi G. Bawendi, Mechanistic Insights into the Formation of InP Quantum Dots, *Angew. Chem. Int. Ed.,* **2010**, 49, 760 – 762.

[2] Sahid Hussain, Nayoun Won, Jutaek Nam, Jiwon Bang, Hyokyun Chung, and Sungjee Kim, One-Pot Fabrication of High-Quality InP/ZnS (Core/Shell) Quantum Dots and Their Application to Cellular Imaging, *ChemPhysChem, 2***009**, 10, 1466 – 1470.

[3] Shu Xu, Sandeep Kumar, and Thomas Nann, Rapid Synthesis of High-Quality InP Nanocrystals, *J. AM. CHEM. SOC.*, **2006**, 128, 1054-1055.

[4] Liang Li and Peter Reiss, One-pot Synthesis of Highly Luminescent InP/ZnS Nanocrystals without Precursor Injection, **2008**, 130, 11588–11589

[5] Renguo Xie, David Battaglia, and Xiaogang Peng, Colloidal InP Nanocrystals as Efficient Emitters Covering Blue to Near-Infrared, *J. AM. CHEM. SOC.*, **2007**, 129, 15432-15433

[6] David Battaglia and Xiaogang Peng, Formation of High Quality InP and InAs Nanocrystals in a Noncoordinating Solvent, *Nano Lett.*, **2002**, Vol. 2, No. 9, 1027-1030.

[7] Derrick W. Lucey, David J. MacRae, Madalina Furis, Yudhisthira Sahoo, Alexander N. Cartwright, and Paras N. Prasad, Monodispersed InP Quantum Dots Prepared by Colloidal Chemistry in a Noncoordinating Solvent, *Chem. Mater.*, **2005**, 17, 3754-3762.

Size-tunable, hexagonal plate-like Cu_3P and Janus-like Cu-Cu_3P nanocrystals

Luca De Trizio, Albert Figuerola, Liberato Manna, Alessandro Genovese, Chandramohan George, Rosaria Brescia, Zineb Saghi, Roberto Simonutti, Marijn Van Huis, and Andrea Falqui. Size-Tunable, Hexagonal Plate-like Cu_3P and Janus-like Cu–Cu_3P Nanocrystals, *ACS Nano*, **2012**, 6 (1), pp 32–41.

6.1 Introduction

Transition metal phosphides have attracted much interest in the recent years for their potential in magnetic recording media, catalysis and as anode materials in lithium ion batteries.[1,2] Especially in batteries, nanostructuration of the active material in the electrodes can introduce improvements with respect to bulk materials in terms of charge/discharge cycling and rates.[3-6] Several efforts have been made to prepare nanoparticles of transition metal phosphides and the most promising results were obtained with the solution-phase high-temperature decomposition of organometallic molecular precursors, which yielded spherical, rod-like and hyperbranched cobalt, nickel, iron, vanadium and manganese phosphide nanoparticles,[7-15] while Cu_3P nanoparticles had been prepared almost exclusively by ball milling,[2] ceramic,[2,16] solid-vapor[17] or solvothermal approaches.[18-22] Cu_3P is interesting as it could represent an air-

stable and an environmentally-friendly material in light and high capacity anodes, since it has theoretical gravimetric capacities which are slightly higher than those of graphite but volumetric capacities more than three times larger than graphite (3020 $mAhcm^{-3}$ for Cu_3P and 830 $mAhcm^{-3}$ for graphite).[23,24]

In 2007, an alternative method for the synthesis of metal phosphide nanoparticles was reported by the groups of Schaak and Chiang[25,26] and consisted of a sequence of reactions in which first metallic nanoparticles were formed and later they were phosphorized with alkyl phosphines. The method was initially tuned for Ni_2P nanoparticles and later generalized to other transition metals, thus becoming the first valuable approach for the preparation of size-controlled and soluble Cu_3P particles in the nanosize regime.[27] The metallic nanoparticles obtained in the first step retained their size and shape upon phosphorization, and hence a good control over the metal growth guaranteed narrow size distributions of the corresponding phosphide nanocrystals. Often the phosphorization process has been found to proceed *via* the Kirkendall effect, by which large enough metal nanoparticles lead to hollow structures, while slight modifications of this procedure yield "non-hollow" phosphide nanoparticles.[26]

Here we report two "one-pot" approaches for the preparation of colloidal Cu_3P nanocrystals, one of which is also capable to yield Janus-like Cu-Cu_3P nanoparticles. In the first approach (Scheme 1a), Cu_3P nanocrystals with hexagonal plate-like shape and sizes tunable from 5 to 50 nm were synthesized via a direct, homogeneous nucleation of small Cu_3P nuclei, which could be grown bigger with longer reaction time. In the second approach (Scheme 1b) Cu_3P nanocrystals were obtained still using a one-pot synthesis in which first Cu nanocrystals were formed and then they were phosphorized over time to Cu_3P. In this case the formation of hollow nanostructures was never observed, while instead we always found dimeric Janus-like nanoparticles as intermediate, with one domain made of Cu and the other made of Cu_3P, the two domains sharing a flat epitaxial interface. In this case the intermediate Cu_3P domains in the Janus-like nanoparticles and the final Cu_3P nanocrystals exhibited a truncated hexagonal bipyramidal habit. If annealed at high temperature and under high vacuum, the Janus-like nanoparticles were de-phosphorized, thus they were transformed back to single nano-crystals of metallic copper. Such feature suggests a possible use of these nanoparticles as phosphorous sources.

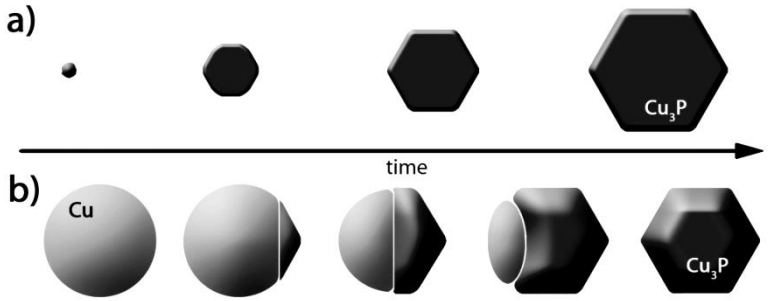

Scheme 6.1 Sketches of the two synthesis approaches to Cu_3P nanocrystals. Approach a) is based on the direct, homogeneous nucleation of platelet-shaped Cu_3P nanocrystals, which then grow over time. In approach b), first Cu nanoparticles are grown, and then they are progressively phosphorized to Cu_3P Janus-like particles in which the volume fraction of the truncated bipiramidal Cu_3P domain increases over time.

We studied the electrochemical lithiation of both the Cu_3P nanoplates and the Cu-Cu_3P Janus like particles and found that the lithium ions can be reversibly intruded and extruded from the phosphide nanoplates, following a reversible displacement reaction (between lithium and copper ions) that makes them an attractive material for applications in lithium ion batteries. On the other hand, the electrochemical properties displayed by the Janus-like nanoparticles with respect to lithiation were remarkably different, due to the presence in them of the large copper domains, which actually makes them unsuitable for applications in batteries.

As regarding the *warm white light* project these NCs would be an ideal template material for the production of InP. Cation-exchange procedures with In^{3+} would lead to the transformation of Cu_3P to InP opening new alternative synthetic ways for the production of InP QDs. In the last section of this work the cation-exchange strategies applied to Cu_3P NCs will be shown.

6.2 Synthetic Strategies Adopted for Cu_3P NCs

In both synthesis approaches that we followed, a mixture of 3 g of trioctylphosphine oxide (TOPO) and the desired amount of trioctylphosphine (TOP) was degassed in a reaction flask for 2h at 150°C under vacuum and then put under inert atmosphere at 370 °C. In a second flask, a solution of CuCl (0.4 mmol), oleylamine (2.4 mmol) and octylamine (2.4 mmol) was prepared under inert atmosphere and then heated at 180°C for 2h to get a clear solution, after

which it was cooled to 150°C and its content was rapidly injected via a syringe into the first reaction flask. The resulting mixture was kept at 350°C for the desired time and then cooled to room temperature. In the syntheses, the relative amounts of TOP and CuCl dictated whether direct nucleation of Cu_3P nanocrystals occurred, followed by their growth (first approach), or alternatively first Cu nanocrystals were formed and then they were converted into Cu_3P (second approach). Direct nucleation of Cu_3P nanocrystals, with apparently no intermediate formation of Cu nanocrystals, was observed when 2 ml (1.66 g) of TOP or more were added, which corresponds to a TOP:Cu molar ratio of at least 11.2:1. A typical time evolution of the Cu_3P nanoparticles is displayed in Figure 1a-d, which reports Transmission Electron Microscopy (TEM) images of aliquots taken at different times. Small Cu_3P nuclei, with sizes around ~5nm and hexagonal shape, were observed already a few seconds after injection (Figure 6.1a). After 2 minutes (Figure 6.1b), nanocrystals with hexagonal plate-like morphology were observed, and the morphology was retained for longer reaction times (Figure 6.1c-d), during which the nanocrystals became bigger (they typically reached 50 nm after 30 minutes). Therefore the final size of these plate-like nanocrystals could be easily controlled by the total reaction time.

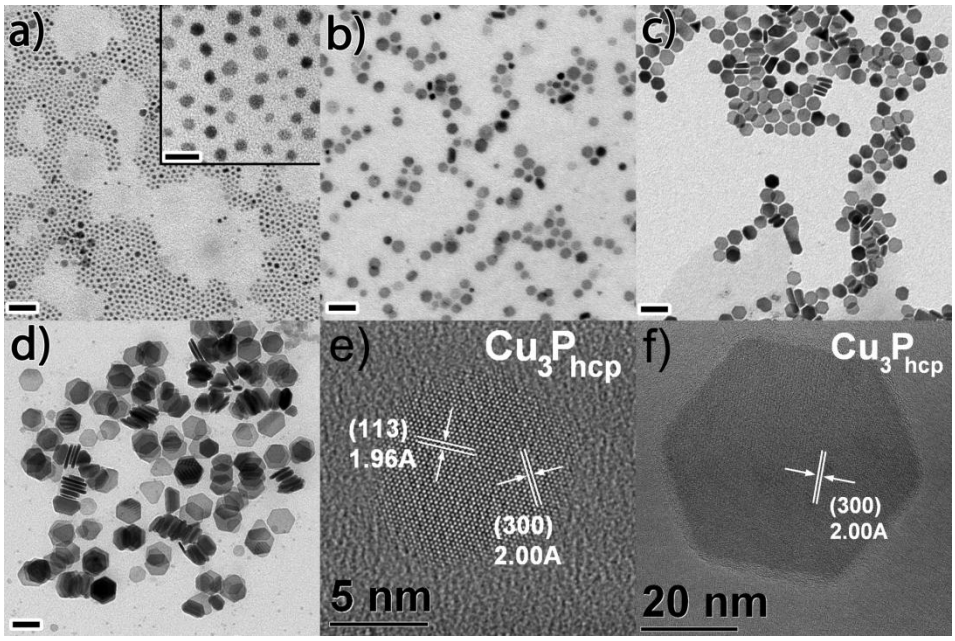

Figure 6.1 TEM images documenting the direct formation of Cu_3P nanoplates in solution when working at a TOP:Cu molar ratio of 11.2:1. Images refer to aliquots recovered after a) 10 sec, b) 2 min, c) 15 min and d) 25 min of reaction, respectively. The scale bar is 50 nm for the panels and 20 nm for the inset. e-f) HRTEM images of Cu_3P nanoplates after a) 10 sec and b) 25 min of reaction, respectively. In both cases the nanocrystals show a structure clearly ascribable to the hcp Cu_3P phase.

When the amount of TOP was increased from 2ml to 3 and 4 ml a faster nucleation and growth occurred. After less than one minute of reaction a polydisperse product in which many particles were already 50 nm big was observed. Variations in the amount of TOPO instead did not have a major effect on the nucleation and growth rates, suggesting that TOPO behaved more like a solvent, while TOP was the source of phosphorous. The nanocrystals had Cu_3P hexagonal close packed (hcp) structure (space group $P6_3cm$), as confirmed by High Resolution TEM (HRTEM, Figure 6.1e-f). These nanoplates tended to form columnar stacks on the carbon support film upon evaporation of the solvent (Figures 6.1d and 6.2a-c), as previously found by various groups on disc-like particles of other materials.[28,29]

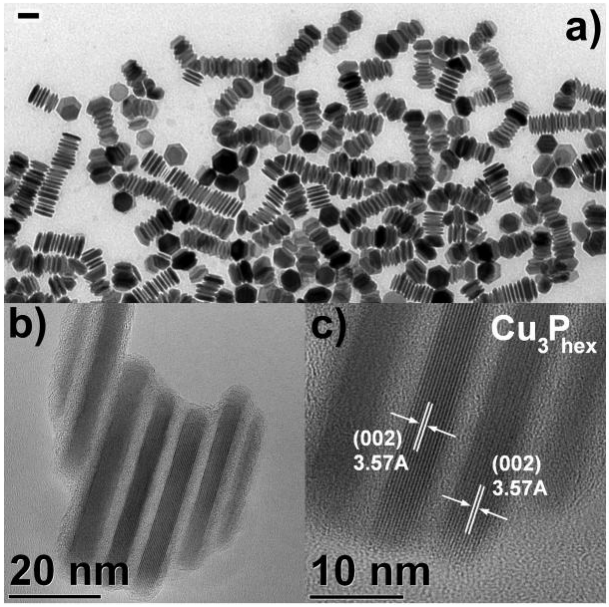

Figure 6.2 TEM (panel a)) and HRTEM (panels b) and c)) images of Cu3P nanoplates as obtained after 25 min of direct nucleation reaction and self-assembled in columnar stacks with their main surface normal to the plane of the TEM grid. The scale bar in panel a) has a length corresponding to 50 nm. Panel c) shows a higher magnification image of the bottom right corner of the group of particles displayed in panel

When instead a volume of TOP of less than 2 ml was used (for example 1 ml, corresponding to a TOP:Cu ratio of 5.6:1) first Cu nanoparticles were formed, most likely due to a reduction of Cu^+ by the alkylamines present. Over time, these Cu particles reacted with TOP and were slowly converted to Cu_3P. A typical time evolution of the synthesis is reported in Figure 6.3, which displays TEM images of aliquots taken at 4, 10, 25 and 45 minutes of reaction time (i.e. after the injection), respectively. At 10 and 25 minutes, particles composed of two domains of

different electron contrast were clearly discerned. Especially in the aliquot at 25 minutes, each Janus-like particle was formed by one hemispherical domain and one faceted domain. In the aliquot at 45 minutes, only faceted particles were found. The XRD pattern of these Janus-like particles evidenced peaks arising from both metallic Cu and Cu_3P (Figure 6.3e).

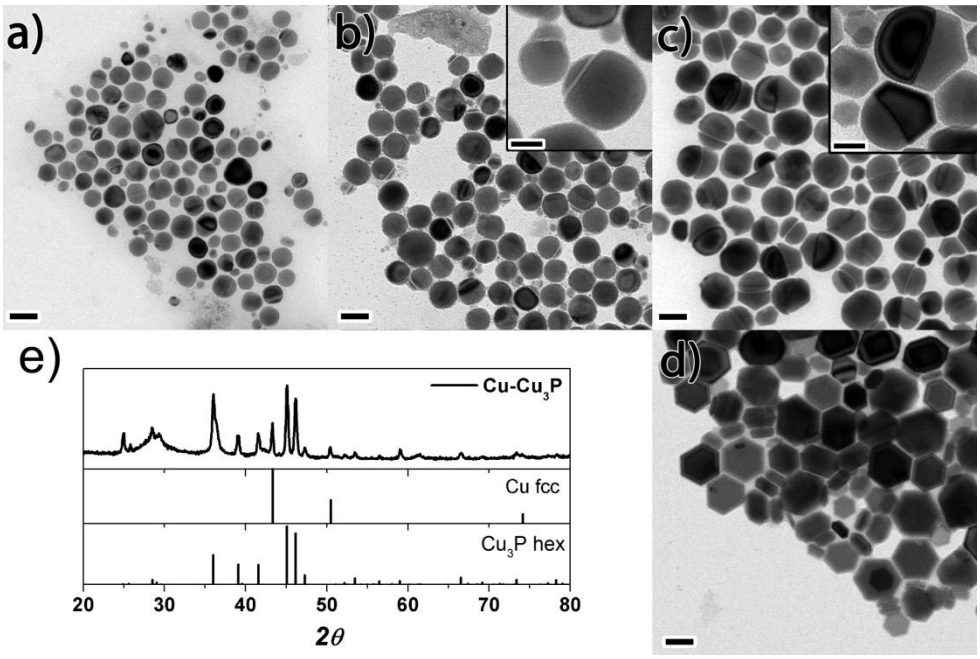

Figure 6.3 a-d) TEM images documenting the formation of Cu nanoparticles and their progressive phosphorization when working at a TOP:Cu molar ratio of 5.6:1. Aliquots were collected at the following reaction times: a) 4 min; b) 10 min; c) 25 min; d) 45 min. The scale bar is 50 nm for the panels and 20 nm for the insets; e) XRD pattern of a powder sample of Janus-like particles. Bulk reflexes of Cu and Cu_3P are also displayed. As a note, also in this second reaction mechanism, the relative amount of TOPO (ranging from 2 to 4 g) did not have any effect on the chemical conversion of Cu into Cu_3P, which confirms the role of TOP as phosphorous precursor.

6.3 TEM analysis of Cu_3P and Cu-Cu_3P Systems

HRTEM analysis (Figure 6.4a) confirmed that in the Janus-like particles the spherical domain was Cu, with face-centered cubic (*fcc*) crystalline structure (space group Fm3m) while the faceted domain was Cu_3P, with crystal lattice ascribable to *hcp* Cu_3P. HRTEM analysis (Figure 6.4b) on the particles recovered at later times indicated instead that they were Cu_3P nanocrystals, with no more Cu domains attached to them. Within the intrinsic limitations of the EFTEM reported in

literature,[30,31] the EFTEM images (insets of the Figure 6.4c and 6.4d) mapped the spatial distribution of copper (red) and phosphorus (green) in these two samples, in agreement with the structural identification of the domains composing the nanostructures provided by HRTEM.

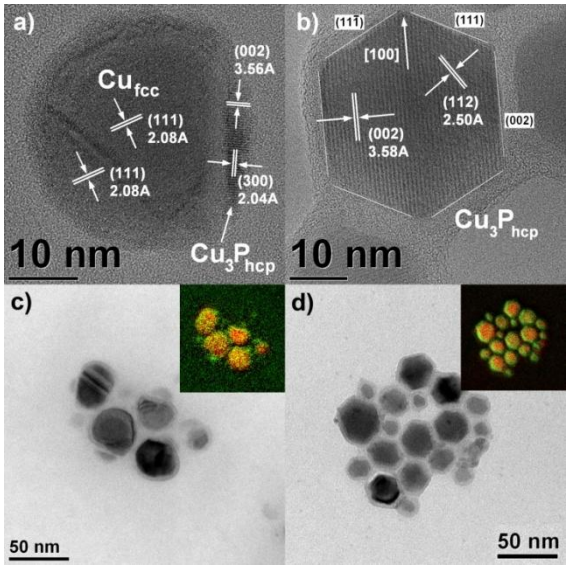

Figure 6.4 HRTEM and EFTEM images displaying the evolution of Cu-Cu_3P nanocrystals obtained by phosphorization of the Cu nanoparticles after a), c) 10 min and b), d) 45 min of reaction, respectively. Panels a) and b) display HRTEM images of a particle representative of each sample. Panels c) and d) are EFTEM zero-loss images of the two samples, with their inset showing P (green) and Cu (red) EFTEM maps of the same zones.

These morphologies suggest that the phosphorization most likely proceeds via the nucleation of a small Cu_3P domain on only one site on the surface of the initial Cu nanocrystals, which then extends progressively from that region to the whole nanocrystal. Under this assumption, one possible "kinetic" explanation why the phosphorization does not start over the whole surface of the nanocrystals, which would lead instead to a Cu@Cu_3P core@shell morphology, could be related to the type of surfactant coverage, which prevents this process from taking place. Hence, as soon as an active site is found for TOP to react on the surface of a Cu nanocrystal, further phosphorization will proceed only from that site. Also, it is remarkable that in the present phosphorization scheme of a Cu nanocrystal there appears to be no large unbalance in the relative diffusion rates of Cu and P species, which would have yielded hollow Cu_3P structures if for example P were diffusing much slower than Cu species.

To better understand the mechanism leading to the formation of the Cu_3P nanocrystals obtained by progressive phosporization of Cu nanoparticles, an in-depth TEM analysis of the intermediate steps of reaction was carried out. Figure 6.5 displays the results of this analysis, including HRTEM, EFTEM and Electron Tomography (ET). The latter was performed using High Angular Annular Dark Field (HAADF) imaging in Scanning TEM (STEM): as in this mode the intensity depends on Z^2, the STEM-HAADF is very effective to distinguish materials with different mean atomic number. In particular Figure 6.5b displays the 3D volume reconstruction of the dimeric Janus-like heterostructures as obtained by ET analysis, where the lighter part of each Janus particle is that made of metal copper.

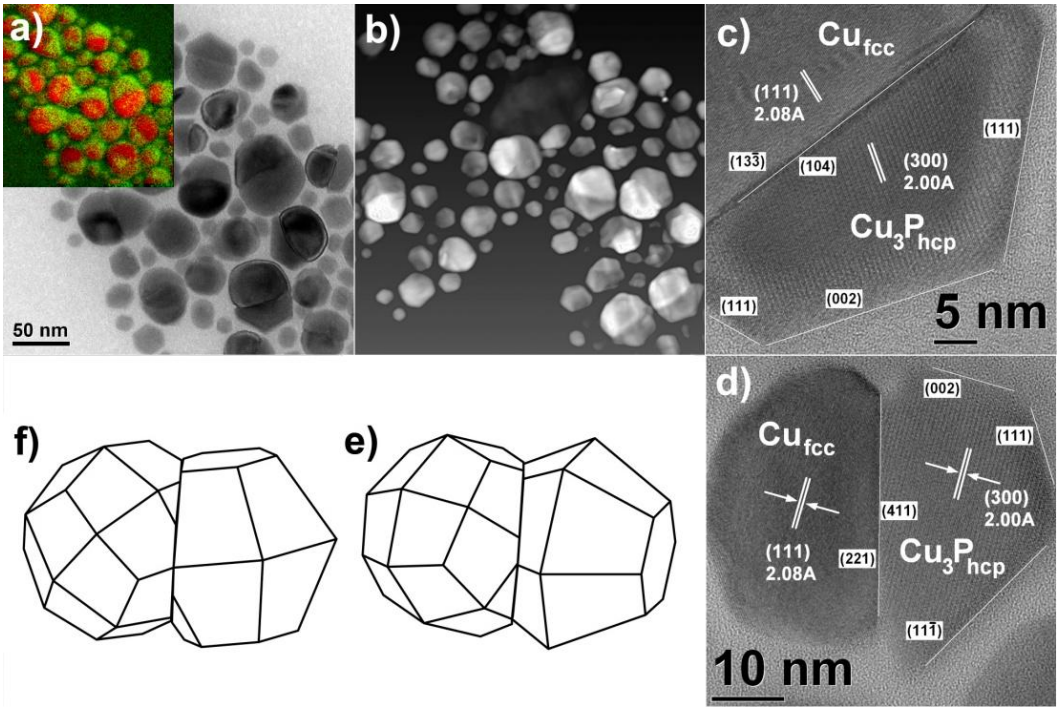

Figure 6.5 Evolution of the initial copper nanocrystals after 25 min of phosphorization, leading to the formation of Janus-like Cu-Cu_3P heterostructures. a) EFTEM zero-loss images of the sample, with inset showing P (green) and Cu (red) EFTEM maps of the same zone. b) 3D volume reconstruction and c), d) HRTEM images of the dimers. The lighter part of each dimer is the one constituted by copper. The Cu and Cu_3P domains are attached following two types of epitaxial relationships: c) $Cu_3P(411)//Cu(221)$ together with $Cu_3P\langle 0\text{-}11\rangle//Cu\langle -110\rangle$ and d) $Cu_3P(104)//Cu(13\text{-}3)$ together with $Cu_3P\langle 0\text{-}10\rangle//Cu\langle -321\rangle$ (interface and vector alignment relationship, respectively). Figure e) and f): reconstruction of the crystalline shape of the structures shown in c) and d), respectively.

Moreover, via a detailed analysis of HRTEM[32,33] (see Figure 6.5c-d) data of several Cu-Cu_3P heterostructures we identified two distinct epitaxial growth processes of Cu_3P on Cu occurring during the phosphorization of the Cu

nanocrystals. In both cases, the Cu_3P (300) lattice planes were found aligned with the Cu(111) lattice planes along the epitaxial interfaces according to the following crystallographic relationships:

1) $Cu_3P(411)//Cu(221)$ and $Cu_3P<0\text{-}11>//Cu<\text{-}110>$

2) $Cu_3P(104)//Cu(13\text{-}3)$ and $Cu_3P<0\text{-}10>//Cu<\text{-}321>$

where the left terms represent the interface alignment and the right ones the vector alignment. For each epitaxial relationship the lattice mismatch was calculated considering the projections of the main lattice planes Cu_3P (300) and Cu (111) onto the corresponding epitaxial interfaces. We can define the lattice mismatch (*m*) between two lattice sets along a certain direction as follows:

$$m = |d_1\text{-}d_2| \; / \; 0.5\cdot(d_1+d_2) \times 100\%$$

In the expression above d_1 and d_2 represent the projected lengths of $Cu_3P(300)$ and Cu(111) lattice planes onto their corresponding epitaxial interfaces. *m* was calculated to be 0.9% and 0.5% for the epitaxial relationships 1) and 2) reported above, respectively, which indicates a good fit of the two crystalline domains composing the Cu-Cu_3P heterostructures that have commensurate misfit along the epitaxial interfaces. By combining HRTEM and 3D volume reconstruction resulting from Electron Tomography analysis we could determine both the epitaxial relationships between the two domains composing the heterostructures and their crystalline habit as displayed in Figure 6.5e and 6.5f, were we reported the sketches of the nanocrystals imaged in Figure 6.5c and 6.5d, respectively. When the reaction was carried out until complete phosphorization, the final Cu_3P nanocrystals had truncated hexagonal bipyramid habit, which is different from the plate-like habit of the nanocrystals synthesized by direct nucleation of Cu_3P.

The Cu-Cu_3P eutectic in the Cu-P bulk alloy is well known in metallurgy and has been studied extensively in the past[34] and it is interesting to recall that in 1988 Selke et al.[35] rapidly cooled bulk Cu-P alloys at 15%P, close to the Cu-Cu_3P eutectic point (15.7% P) and found a microcrystalline lamellar structure of alternating Cu and Cu_3P layers with preferential orientation. The lamellae were stacked according to the planar orientation relationship $Cu_3P(010)//Cu(111)$ and with epitaxial interface parallel to Cu(111) and $Cu_3P(010)$ lattice planes. These relationships, which according to the authors should minimize the interfacial energy, are different however from those found by us in the Janus-like Cu-Cu_3P

nanocrystals. We observed instead a perfect parallelism between the $Cu_3P(300)$ and Cu(111) lattice planes for one orientation relationship but not for the second one, where the $Cu_3P(300)$ and Cu(111) lattice planes form an angle of 11°. Besides, the epitaxial interfaces in our Cu-Cu_3P dimeric heterostructures were tilted with respect to the $Cu_3P(300)$ and Cu(111)lattice sets, and this was observed for both 1) and 2) (see above) orientation relationships, which is clearly different from the quenched Cu-P alloys.

The above differences can be rationalized in terms of the remarkably different conditions in which the two types of heterostructures were prepared. The formation of a eutectic requires the initial melting of the components and the subsequent solidification of the alloy below the eutectic temperature, which in the specific case of the Cu-P system is 714°C, i.e. a much higher temperature than that involved in our nanocrystal syntheses. Moreover, rapid cooling of the Cu-Cu_3P eutectic by Selke et al. led to a spinodal decomposition process, with possible volume constraints in the evolution of the lamellar phase, which could have imposed the kinetically driven formation of only specific sets of interfaces. In our case the phosphorization of Cu particles occurred in the solution phase, therefore the nucleation and growth of Cu_3P crystals most likely proceeded without volume constraints, so that their growth was favoured along those crystallographic directions that minimized the most the interfacial energies, as suggested by the low mismatch values measured in the Cu-Cu_3P nanocrystals reported here.

One aspect for sure that Cu-Cu_3P eutectic in the bulk alloy and our nanoparticles have in common is the evolution of extended and flat interfaces between the Cu and Cu_3P domains. This indicates that, despite the markedly different experimental conditions, in the Cu-Cu_3P system there is preference for development of specific sets of low energy interfaces over ill-defined, defective interfaces. This concept, if extended to other alloy/eutectic systems that exhibit similar behaviour, might help to predict the formation of nanoscale heterostructures with flat, epitaxial interface between domains of two different materials.

In order to investigate the thermal stability of the Janus-like particles, an HRTEM in-situ annealing study was performed on the Janus-like Cu-Cu_3P particles drop-cast onto a MEMS microheater.[36] After annealing at temperatures between 400 and 500 °C, the Cu_3P domains were found to transform into Cu, as shown in Figure 6.6a-b, so that homogeneous, single crystalline Cu particles were

obtained, due to a de-phosphorization caused by the evaporation of P into the vacuum.

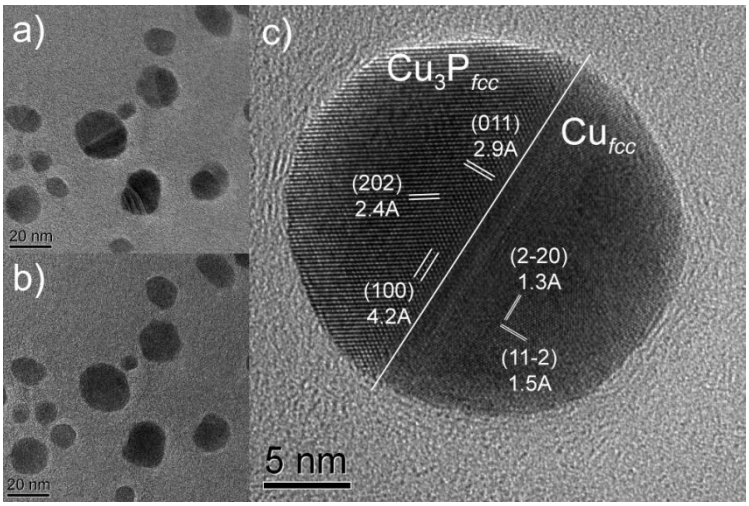

Figure 6.6 Evolution of the Janus-like Cu-Cu_3P nanocrystals due to in-situ thermal annealing under vacuum, as performed in the HRTEM. a) Particles imaged at 450°C, where the dark domains are made of Cu and the lighter ones are made of Cu_3P; b) Same particles shown in a), but after annealing at 500°C for 10 minutes: the particles are single-crystalline and with the fcc copper structure. c) Janus-like particle after annealing at 150°C. The Cu_3P domain appears to have a fcc-type crystalline structure oriented along the [110] zone axis, with lattice parameter equal to 4.16 Å. The copper domain is oriented along the [111] zone axis.

At all considered temperatures, the Cu particles were still crystalline and no melting was observed. The smaller Janus-like particles were found to de-phosphorize at lower temperatures and after shorter time durations than larger particles. After heating at a temperature of 500 °C for 60 minutes, any remaining Janus-like particles (with Cu_3P domains) were typically those larger than 15 nm. When the samples were heated between 100 °C and 200 °C, a number of Janus-like particles exhibited a peculiar behaviour: in Cu_3P domain a pattern of atomic columns was visible which did not correspond to Cu, neither to the hexagonal Cu_3P structure, as displayed in the HRTEM image reported in Figure 6.6c. Instead, it showed a typical [110] projection of a fcc-type structure. When assuming that the Cu_3P variant is cubic, the lattice parameter for fcc-type copper phosphide (Cu_3P_{fcc}) can be estimated at 4.16 Å. Besides, from Figure 6.6c, the following orientation relationship could be deduced:

$$Cu_3P_{fcc}\{100\}//Cu\{1\text{-}10\} \text{and } Cu_3P_{fcc}[011]// Cu[11\text{-}2]$$

The planar alignment coincides with the orientation of the interface, so that $Cu_3P_{fcc}[100]//Cu[1\text{-}10]$ are vectors normal to the interface, while

Cu_3P_{fcc}[011]//Cu[11-2] are vectors parallel to the interface. These findings indicate that the starting hexagonal crystalline structure of the Cu_3P domain changed into a fcc one, being the main advantage of the presence of such a new stacking that it creates a fcc-type Cu_3P_{1-x} {100} spacing of 2.9 Å in the plane of the interface: this is nearly twice the Cu {112} lattice spacing of 1.48 Å and the cubic Cu_3P phase therefore fits much better onto the Cu lattice. This structural change is most likely associated to a variation of the Cu/P stoichiometry.

6.4 Electrochemical Properties of Cu_3P NCs

One possible application of the nanoparticles developed in the present work is in lithium ion batteries, as already pointed out in the introduction for this class of materials. To this aim, we investigated the electrochemical properties of the Cu_3P nanoparticles prepared following the first synthetic approach, which yielded plate-like morphology. Cyclic voltammetry and impedance analysis were employed to probe the lithiation and de-lithiation behaviour of the platelets. It is well known from previous works that the lithiation process on Cu_3P electrodes leads to the formation of metallic copper upon a progressive displacement with Li^+ ions, and upon de-lithiation, the extruded copper is re-incorporated so that the Cu_3P phase is recovered. The process can be represented as: [37, 38]

$$Cu_xP + x\ Li \Leftrightarrow L_xCu_{x-1}P + Cu^0$$

This quasi-reversible displacement reaction has manifested in a reversible capacity around 370-380 mAh/g for Cu_3P based nanostructures and thick films reported so far.[17,39] In our case, the Cu_3P nanoplates could easily be indentified in the random dispersions from the sampled composite (85% wt) used for preparing electrodes, due to the fact that their plate-like morphology remained intact, see Figure 6.7b. After the first discharge from 3.0 V to 0.02 V on galvanostatic mode, the charge cycle was followed by the AC impedance, as reported in the Figure 6.7a. The resulting semi-circles (inset of Figure 6.7a) in the high frequency region clearly indicated the occurrence of the charge-transfer process (due to the transfer of Li^+ ions) through the electrode/electrolyte interface, followed by the spike-like region at the lower frequency region of impedance spectra that evidences a solid-state Li^+ ion diffusion. At OCPs (Open Circuit Potential) below 1V, the electrodes had a lower polarization resistance that increased upon de-lithiation as for Cu_3P. In agreement with previous literature reports,[17,37-39] at reduction potentials below 1.0 V the progressively extruded

Cu ions appeared to be crystallized into metal domains, while upon Cu intrusion the initial Cu_3P phase was recovered. This occurred at oxidation potentials, starting from 1.0 V to 2.4 V, see Figure 6.7a. This reversibility of Cu metal extrusion/intrusion upon charge/discharge indicated that hexagonally close packed lattice of Cu_3P nanoplates has the capability to withstand the possible structural deformation caused during cycles by the intrusion/extrusion of both Cu and Li ions. Cyclic voltammograms (CVs), as reported in Figure 6.7c, further illustrated the complex nature of lithiation/de-lithiation processes which proceed through multiple steps on the Cu_3P nanoplates. From the CVs, the Cu displacement reaction with Li^+ ions started from at about 1.5 V versus Li and continued when moving towards more negative potentials. There were several peaks (indicating lithiation in different steps) further in the cathodic scan followed by a strong reduction peak centered at 0.4-0.3 V during the first CV cycle (as reported in the inset), where most of the Cu ions had been extruded from the hcp crystal lattice as they were replaced by Li^+ ions. At 0.02 V, about 3.5 Li^+ ions per Cu_3P would be required to complete the displacement reaction and to achieve complete reduction of copper to Cu^0 during the progressive lithiation. In the oxidation process, the sharp peaks at 1.1V, 1.3V, 1.5V and a shoulder at 1.8V were indicative of in-steps Cu intrusion reaction to form Cu_3P. This is in good agreement with the impedance data on charge cycle above 2.0 V, where the progressively enlarged semi-circles indicate that the electrode resistance increased as in the case of Cu_3P. In the second cycle (Figure 6.7c), most of the peaks were retained and shifted slightly towards more positive potentials and slowly stabilized in the successive cycles.

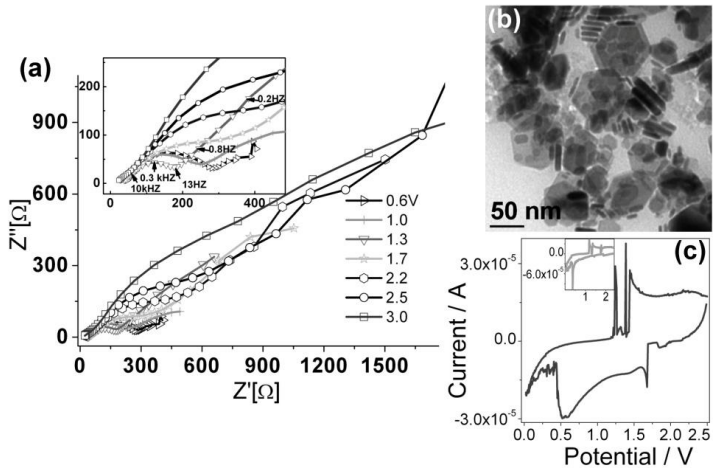

Figure 6.7 a) Impedance spectra of the Cu_3P electrode as the function of open circuit potential (OCP), the inset is a magnification of the high frequency region; b) Cu_3P nanoplates in the composite electrode; c) Cyclic Voltammogram (CV) of 2nd cycle at 0.5 mVS^{-1} illustrating the complex lithiation process involving the Cu_3P electrodes. The inset reports the CV of 1st cycle.

We additionally characterized the electrochemical properties of the Janus-like Cu-Cu_3P nanoparticles. One motivation in this direction came from considerations that a battery performance depends also on the electronic conductivity of the electrodes and on the interface between the electrodes and the current collectors,[11] and that one way to optimize these features would be offered by hybrid nanocrystals in which the metallic domain would improve electronic conductance, as possibly in the case of the present Janus-like dimers. In other words, nanostructured electrodes where both an electroactive domain and a robust metallic nanodomain are homogeneously combined could be in principle ideal for effective and lasting lithium ion batteries. In this regard, a previous work on Cu_3P by Villevieille et al. reported substantial improvements in terms of cyclability when Cu_3P nanoparticles were grown on metallic Cu nanorods working as current collectors, which was claimed to be due to both the nanometric dimensions of the materials and to the quality of the interface between them.[17] However, the same CV analysis carried out on the Cu-Cu_3P nanoparticles was clearly indicative of irreversible electrochemical processes. Basically, a strong reduction current in the cathodic scan was observed but on the oxidation process almost no activity was measured. The impedance analysis of a typical electrode built from Cu-Cu_3P nanocrystals indicated that the resistance of the electrode increased irreversibly from the second cycle. We ascribed this behaviour to the presence of the large metal copper domains, which most likely cause irreversible alloying processes.

6.5 Cation-Exchange with In^{3+}

Cation exchange reactions between Cu_3P and In^{3+} ions would lead to a new synthetic approach for the production of InP NCs. In order to obtain InP we tried different approaches.

At first, following a procedure developed by Alivisatos P. et al. [40] we used tributylphosphine (TBP) to promote the cation exchange between Cu^+ and In^{3+}. In order to avoid oxidation processes we decide to work under inert atmosphere in a glove box. In a typical synthesis a solution of In^{3+} (0.2mmol) dissolved in MeOH (2ml) was added to a mixture of toluene (1ml) and TBP in a desired amount. Once a clear solution was obtained through stirring, a dispersion of Cu_3P NCs (0.125 mmol of $Cu^{+)}$ in toluene (1ml) was added and the resulting mixture was stirred for 24 hours at room temperature. The solution was then

heated at 80°C for 30 minutes. $In(ac)_3$, $InCl_3$ and Indium 2,4 pentendionate were used as Indium salts. Different amounts of TBP, namely 0.15ml and 0.30ml, were used in cation exchange reactions. Nothing occurred using these synthetic procedures. Also we tried avoiding MeOH (that lowered in some case the solubility of In salts, as $In(ac)_3$) and toluene using just 2ml of TBP as solvent and base. In this case we could heat the whole solution at 200°C but nothing was observed.

We then moved our attention on typical strategies that were demonstrated to work in CdS and CdSe systems.[41] In a typical synthesis a solutions of In^{3+} (0.5mmol), n-hexylphosphonic acid (HPA) (80mg), octadecylphosphonic acid (ODPA (290mg), tri n-octylphosphine oxide (TOPO) (3g) and tri n-octylphosphine (TOP) (1.5g) was degassed in a three neck flask at 150°C under vacuum. A dispersion of Cu_3P in TOP (0.5ml) containing 0.065mmol of Cu^+ was injected into the flask under N_2 at different temperatures. As Indium salts we decide to use $In(ac)_3$ and $InCl_3$. Injecting the Cu_3P NCs at temperatures higher than 100°C no product could be precipitated already after some minutes, probably because the phosphonic acids could bind to the Cu^+ ions dismantling the Cu_3P structure. Working at lower temperatures, on the other side, didn't lead to any cation exchange but just Cu_3P nanocrystals were collected.

6.6 Conclusions

In conclusion, we have reported here two "one-pot" approaches for the preparation of size-controlled Cu_3P nanoparticles within the 5-50 nm range. The electrochemical properties suggested that the as-prepared Cu_3P nanoplates could be used as anode material in lithium ion batteries. The nanocrystals couldn't be converted to InP through the cation-exchange procedures that we exploited. Other systems have to be synthesized in order to obtain non-toxic, fluorescent and robust QDs for the *warm white light* project.

6.7 References

[1] Brock, S. L.; Senevirathne, K. Recent developments in synthetic approaches to transition metal phosphide nanoparticles for magnetic and catalytic applications. *J. Sol. St. Chem.* **2008**, *181* 1552-1559.

[2] Bichat, M.-P.; Politova, T.; Pfeiffer, H.; Tancret, F.; Monconduit, L.; Pascal, J.-L.; Brousse, T.; Favier, F. Cu_3P as anode material for lithium ion battery: powder morphology and electrochemical performances. *J. Power Sources* **2004**, *136*, 80-87.

[3] Bruce, P.G.; Scrosati, B.; Tarascon, J.M. Nanomaterials for rechargeable lithium batteries. *Angew. Chem. Int. Ed.* **2008**, *47*, 2930-2946.

[4] Arico, A.S.; Bruce, P.; Scrosati, B.; Tarascon, J.M.; Van Schalkwijk, W. Nanostructured materials for advanced energy conversion and storage devices. *Nature Mater.* **2005**, *4*, 366-377.

[5] Cabana, J.; Monconduit, L.; Larcher, D.; Palacin, M.R. Beyond Intercalation-Based Li-Ion Batteries: The State of the Art and Challenges of Electrode Materials Reacting Through Conversion Reactions. *Adv. Mater.* **2010**, *22*, E170-E192.

[6] Bichat, M.P.; Gillot, F.; Monconduit, L.; Favier, F.; Morcrette, M.; Lemoigno, F.; Doublet, M. Redox-induced structural change in anode materials based on tetrahedral (MPn(4))(x-) transition metal pnictides. *Chem. Mater.* **2004**, *16*, 1002.

[7] Perera, S.C.; Fodor, P.S.; Tsoi, G.M.; Wenger, L.E.; Brock, S.L. Application of de-silylation strategies to the preparation of transition metal pnictide nanocrystals: The case of FeP. *Chem. Mater.* **2003**, *15*, 4034-4038

[8] Perera, S.C.; Tsoi, G.; Wenger, L.E.; Brock, S.L. Synthesis of MnP nanocrystals by treatment of metal carbonyl complexes with phosphines: A new, versatile route to nanoscale transition metal phosphides. *J. Am. Chem. Soc.* **2003**, *125*, 13960.

[9] Koo, J.P.B.; Hwang, Y.; Bae, C.; An, K.; Park, J.G.; Park, H.M.; Hyeon, T. Novel synthesis of magnetic Fe_2P nanorods from thermal decomposition of continuously delivered precursors using a syringe pump. *Angew. Chem. Int. Ed.* **2004**, *43*, 2282-2285.

[10] Qian, C.; Kim, F.; Ma, L.; Tsui, F.; Yang, P. D.; Liu, J. Solution-phase synthesis of single-crystalline iron phosphide nanorods/nanowires. *J. Am. Chem. Soc.* **2004**, *126*, 1195– 1198.

[11] Park, J.; Koo, B.; Yoon, Y.K.; Hwang Y.; Kang, M.; Park, J.-G.; Hyeon T.' Generalized synthesis of metal phosphide nanorods via thermal decomposition of continuously delivered metal-phosphine complexes using a syringe pump. *J. Am. Chem. Soc.* **2005,** *127 (23)*, 8433-8440.

[12] Li, Y.; Malik, M. A.; O'Brien, P. Synthesis of single-crystalline CoP nanowires by a one-pot metal-organic route. *J. Am. Chem. Soc.* **2005,** *127 (46)*, 16020-16021.

[13] Senevirathne, K.; Burns, A. W.; Bussell, M. E.; Brock, S. L. Synthesis and characterization of discrete nickel phosphide nanoparticles: Effect of surface ligation chemistry on catalytic hydrodesulfurization of thiophene. *Adv. Func. Mater.* **2007,** *17*, 3933-3939.

[14] Maneeprakorn, W.; Malik, M. A.; O'Brien, P. The preparation of cobalt phosphide and cobalt chalcogenide (CoX, X = S, Se) nanoparticles from single source precursors. *J. Mater. Chem.* **2010**, *20*, 2329-2335.

[15] Zhang, H.; Ha, D.-H.; Hovden, R.; Fitting Kourkoutis, L.; Robinson, R. D. Controlled Synthesis of Uniform Cobalt Phosphide Hyperbranched Nanocrystals Using Tri-n-octylphosphine Oxide as a Phosphorus Source. *Nano Lett.* **2011**, *11 (1)*, 188–197.

[16] Pfeiffer, H.; Tancret, F.; Brousse, T. Synthesis, characterization and electrochemical properties of copper phosphide (Cu_3P) thick films prepared by solid-state reaction at low temperature: a probable anode for lithium ion batteries. *Electrochim. Acta* **2005**, *50,* 4763-4770.

[17] Villevieille, C.; Robert, F.; Taberna, P.L.; Bazin, L.; Simon, P.; Monconduit, L. The good reactivity of lithium with nanostructured copper phosphide. *J. Mater. Chem.* **2008**, *18*, 5956-5960.

[18] Su, H. L.; Xie, Y.; Li, B.; Liu, X. M.; Qian, Y. T. A simple, convenient, mild solvothermal route to nanocrystalline Cu_3P and Ni_2P. *Solid State Ionics* **1999**, *122*, 157-160.

[19] Xie, Y.; Su, H. L.; Qian, X. F.; Liu, X. M.; Qian, Y. T. A mild one-step solvothermal route to metal phosphides (metal = Co, Ni, Cu). *J. Sol. St. Chem.* **2000**, *149*, 88-91.

[20] Aitken, J. A.; Ganzha-Hazen, V.; Brock, S.L. Solvothermal syntheses of Cu_3P via reactions of amorphous red phosphorus with a variety of copper sources. *J. Sol. St. Chem.* **2005**, *178,* 970-975.

[21] Wang, X.; Han, K.; Gao, Y.; Wan, F; Jiang, K. Fabrication of novel copper phosphide (Cu_3P) hollow spheres by a simple solvothermal method. *J. Cryst. Growth* **2007,** *307*, 126-130.

[22] Liu, S.; Qian, Y.; Xu, L. Synthesis and characterization of hollow spherical copper phosphide (Cu_3P) nanopowders. *Sol. St. Comm.* **2009**, *149,* 438-440.

[23] Wang, K.; Yang, J.; Xie, J.Y.; Wang, B.F.; Wen, Z.S. Electrochemical reactions of lithium with CuP2 and Li1.75Cu1.25P2 synthesized by ball milling. *Electrochem. Comm.* **2003**, *5*, 480-483.

[24] Bichat, M.P.; Politova, T.; Pascal, J.L.; Favier, F.; Monconduit, L. Electrochemical reactivity of Cu_3P with lithium. *J. Electrochem. Soc.* **2004**, *12*, A2074-A2081.

[25] Henkes, A. E.; Vasquez, Y.; Schaak R. E. Converting metals into phosphides: A general strategy for the synthesis of metal phosphide nanocrystals. *J. Am. Chem. Soc.* **2007,** *129 (7),* 1896-1897.

[26] Chiang, R.-K.; Chiang, R.-T. Formation of hollow Ni_2P nanoparticles based on the nanoscale Kirkendall effect. *Inorg. Chem.* **2007,** *46*, 369-371.

[27] Henkes, A. E.; Schaak R. E. Trioctylphosphine: A general phosphorus source for the low-temperature conversion of metals into metal phosphides. *Chem. Mater.* **2007** *19 (17)*, 4234-4242.

[28] Saunders, A. E.; Ghezelbash, A.; Smilgies D. M.; Sigman M. B.; Korgel B. A. Columnar self-assembly of colloidal nanoplates. *Nano Lett.* **2006**, *6 (12),* 2959.

[29] Li, X.; Shen, H.; Niu, J.; Li, S.; Zhang, Y.; Wang, H.; Li, L. S. Columnar Self-Assembly of Cu_2S Hexagonal Nanoplates Induced by Tin(IV)-X Complex as Inorganic Surface Ligand. *J. Am. Chem. Soc.* **2010**, *132 (37),* 12778–12779.

[30] Lozano-Perez, S.; Titchmarsh J. M. EFTEM assistant: A tool to understand the limitations of EFTEM. *Ultramicroscopy* **2007**, *107 (4-5)*, 313-321.

[31] Verbeeck, J.; Bertoni, G. Model-based quantification of EELS spectra: Treating the effect of correlated noise. *Ultramicroscopy* **2008,** *108 (2)*, 74-83.

[32] Deka, S.; Falqui, A.; Bertoni, G.; Sangregorio, C.; Poneti, G.; Morello, G.; De Giorgi, M.; Giannini, C.; Cingolani, R.; Manna, L.; Cozzoli, P.D. Fluorescent Asymmetrically Cobalt-Tipped CdSe@CdS Core@Shell Nanorod Heterostructures Exhibiting Room-Temperature Ferromagnetic Behavior. *J. Am. Chem. Soc.* **2009**, *131 (35)*, 12817-12828.

[33] Maynadié, J.; Salant, A.; Falqui, A.; Respaud, M.; Shaviv, E.; Banin, U.; Soulantica, K.; Chaudret, B. Cobalt Growth on the Tips of CdSe Nanorods. *Angew. Chem. Int. Ed.* **2009,** *48 (10)*, 1814-1817.

[34] Lindlief, W.E. Melting Points of Some Binary and Ternary Copper-rich Alloys Containing Phosphorus. *Met. Alloys* **1933,** *4*, 85-88.

[35] Selke, H.; Ryder P.L. Microstructure and crystallography of a rapidly quenched eutectic Cu-P alloy. *Acta Metall.* **1988,** *36(8),* 2387-2392.

[36] Van Huis, M.A.; Young, N.P.; Pandraud, G.; Creemer, J.F.; Vanmaekelbergh, D.; Kirkland, A.I.; Zandbergen, H.W. Atomic Imaging of Phase Transitions and Morphology Transformations in Nanocrystals. *Adv. Mater.* **2009**, *21*, 4992-4995.

[37] Crosnier, O.; Nazarz, L.F. Facile Reversible Displacement Reaction of Cu_3P with Lithium at Low Potential. *Electrochem. Solid-State Lett.* **2004**, *7 (7),* A187-A189.

[38] Pfeiffer, H.; Tancret, F.; Bichat, M.P.; Monconduit, L.; Favier, F.; Brousse, T. Air stable copper phosphide (Cu_3P): a possible negative electrode material for lithium batteries. *Electrochem. Comm.* **2004**, *6 (3)*, 263–267.

[39] Mauvernay, B.; Doublet, M.L.; Monconduit L. Redox mechanism in the binary transition metal phosphide Cu_3P. *J. Phys. Chem. Solids* **2006**, *67 (5-6)*, 1252.

[40] Dong Hee Son, Steven M. Hughes, Yadong Yin, A. Paul Alivisatos, Cation Exchange Reactions in Ionic Nanocrystals, *Science*, **2004**, 306, 1009.

[41] Sasanka Deka, Karol Miszta, Dirk Dorfs, Alessandro Genovese, Giovanni Bertoni, and Liberato Manna, Octapod-Shaped Colloidal Nanocrystals of Cadmium Chalcogenides via "One-Pot" Cation Exchange and Seeded Growth, *Nano Lett.,* **2010**, 10, 3770–3776.

Strongly Fluorescent Quaternary Cu-In-Zn-S Quantum Dots

Luca De Trizio, Mirko Prato, Alessandro Genovese, Alberto Casu, Mauro Povia, Roberto Simonutti, Marcelo J. P. Alcocer, Cosimo D'Andrea, Francesco Tassone, and Liberato Manna, Strongly Fluorescent Quaternary Cu–In–Zn–S Nanocrystals Prepared from $Cu_{1-x}InS_2$ Nanocrystals by Partial Cation Exchange, *Chem. Mater.,* **2012**, 24 (12), pp 2400–2406.

7.1 Introduction

Colloidal semiconductor nanocrystals (NCs) are considered extremely promising for applications in many different areas.[1] While early studies were boosted by II-VI type (e.g., CdTe, CdSe and HgS) and IV-VI type (e.g. PbSe) NCs, due to the intrinsic toxicity of these materials recent trends in research on semiconductor NCs are shifting the focus towards the less-toxic NCs of binary III-V, ternary I-III-VI_2 semiconductors and copper based quaternary chalcogenides, which appear to represent valid alternatives.[2-29] Applications of these new classes of NCs have been proven in biomedical labelling,[2-4] solar cells[5-13,26,28,29] and in opto-electronic devices such as color-converting solid state lighting emitting diodes (LEDs).[14,23-25,30,31] Early research in this area had targeted mainly Cd-based NCs,[31-41] and then also binary III-V (e.g. InP

and InAs) and ternary I-III-VI_2 NCs, for example $AgInS_2$,[42] $CuInSe_2$ (CISe) and $CuInS_2$ (CIS) NCs.[23-25,30] CIS and CISe are direct band gap semiconductors, with band gaps of 1.5 eV (CIS) and 1.05 eV (CISe), large absorption coefficients, radiation stability[10,15,43] and a certain tolerance to structural defects. Also, these materials have ionic crystal lattices,[15,44] in analogy with the II-VI class of semiconductors, and therefore they are good candidates for cation exchange reactions. The introduction of Cd, Zn or Ga species in their lattice is indeed rather straightforward and leads to quaternary systems with tunable band gaps and high PL quantum yields (QYs).[24,45-47] Due to all these interesting features, colloidal synthesis routes to these NCs have been intensively developed in the last years, to the point that high QYs and an excellent control over the NC dimensions and the optical emission properties is now routinely reported.[22,24,44,46-57] As an example of ternary I-III-VI_2 NCs, QYs up to 70% were reached by Y.K. Kim et al. in 2012 with CIS(core)/ZnS(shell) NCs.[58] In the case of quaternary Cu-In-Zn-S systems (CIZS), QYs up to 70% were reported by Zhang et al. in 2011[24] even without the need to grow a passivating shell over the CIZS cores. Various studies have then clearly demonstrated that the relative stoichiometries of the various chemical species in CIZS NCs can be varied, which enables to tune both the band gap and the QY of the resulting NCs.[24,46,47]

In this work we present a two-step synthesis of quaternary Cu-In-Zn-S (CIZS) NCs. In the first step, we synthesized Cu-defective CIS NCs (that is, $Cu_{1-x}InS_2$), in which we were able to tune the Cu stoichiometry (from 1 to 0.4 approximately) and we could show that this has strong influence on the QY of the particles. In the second step, these NCs were exposed to Zn^{2+} ions at 210°C, during which Copper and Indium ions were partially replaced by Zinc ions, leading to CIZS (Scheme 7.1).

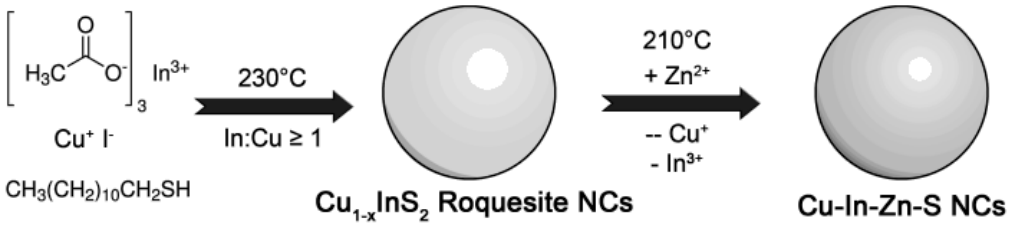

Scheme 7.1 Formation of CIS and CIZS NCs. First CIS NCs with tetragonal chalcopyrite crystalline structure (x>0 when In:Cu>1) are synthesized. Then, Cu^+ and In^{3+} ions are partially replaced in the CIS NCs by Zn^{2+} ions (Cu^+ are actually extracted in a larger fraction than In^{3+}), leading to Cu-defective quaternary CIZS NCs.

CIZS NCs with optimized In/Cu stoichiometric ratio exhibited QYs as high as 80%. Also, from time-dependent PL measurements on the various samples of CIZS we extracted a single exponential PL decay, meaning that non-radiative recombination pathways were strongly reduced in these systems. Eventually the QDs were inglobated in bulk PMMA matrix forming luminescent polymer based nanocomposites. These materials resulted to be very interesting for being applied in the *warm white light* project.

7.2 Synthesis of $Cu_{1-x}InS_2$ QDs

In the first step of the synthesis, we prepared CIS NCs using different molar ratios of In and Cu precursors. We devised a heat-up and solvent-free method for the synthesis of the CIS NCs, following previous works,[17,19] with various modifications. In a typical synthesis, a solution of CuI (0.4 mmol), $In(Ac)_3$ (0.4 mmol) and 5 ml of 1-Dodecanethiol (DT) was loaded into a three-neck flask and was then degassed under vacuum at 80 °C for 1 hour until a clear solution was obtained. The temperature was then raised to 230°C for 11 minutes to let the particles grow. Finally, the reaction was quenched by cooling the solution to room temperature. In order to synthesize copper-deficient NCs (that is, with a ratio of Copper to Indium lower than one), the amounts of DT and $In(ac)_3$ were held fixed while the quantity of Copper precursor was lowered. If needed, the NCs were cleaned by repeated precipitation with acetone and redispersion in hexane for three times. Otherwise the crude solution was used for synthesizing the CIZS nanocrystals. The relevant parameters for the various samples are summarized in Table 7.1 and discussed in this section, while survey HAADF-STEM images of NCs are shown in Figure 7.1a-c.

In:Cu precursor	CIS Composition	Size (nm)	λ_{em} (nm)	QY (%)	PL decay (ns)
1 : 1	$Cu_{1.0}InS_2$	2.9 ± 0.8	714	7	225 (28)
4 : 1	$Cu_{0.45}InS_2$	2.5 ± 0.7	660	19	226 (33)
8 : 1	$Cu_{0.38}InS_2$	2.6 ± 0.8	658	23	245 (34)

Table 7.1 Relevant parameters for syntheses of CIS NCs prepared at different In:Cu precursor ratios. CIS composition was measured by ICP. λ_{em} is the wavelength corresponding to the maximum of the PL peak from NC solutions when excited at 450 nm. The short components of PL decay times are written in brackets.

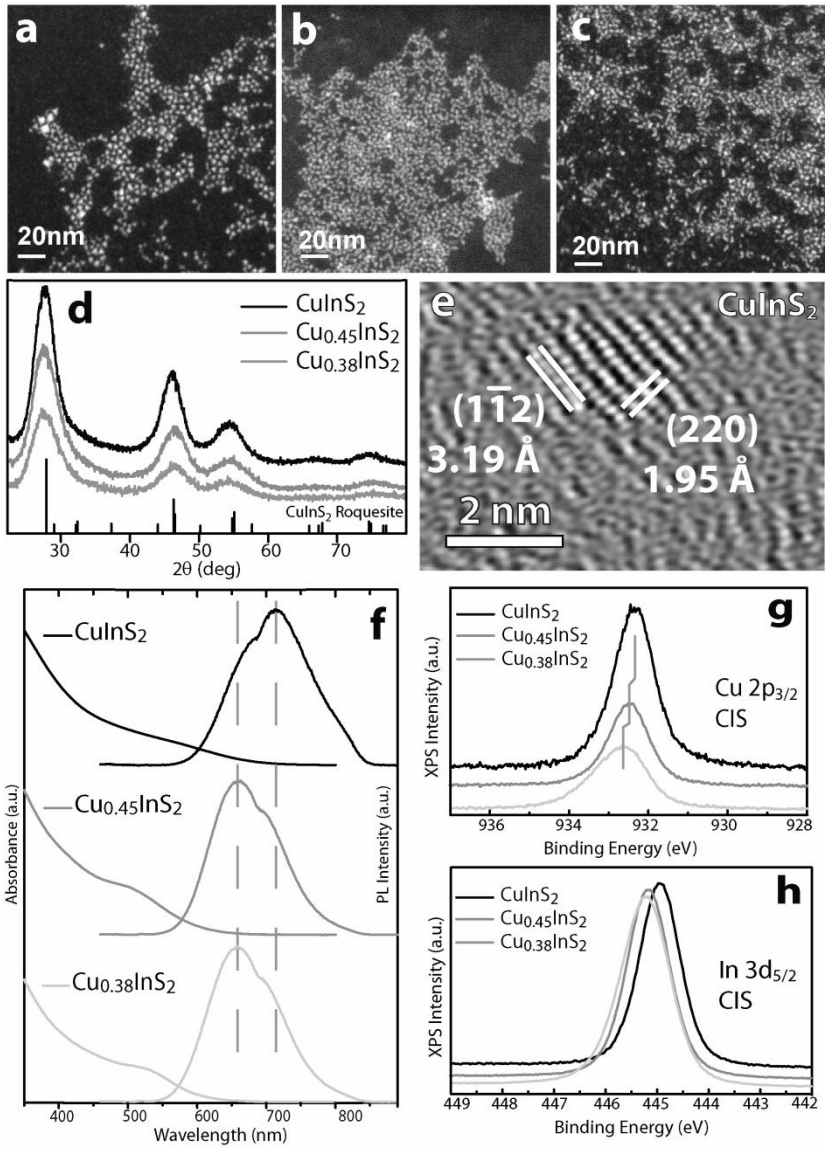

Figure 7.1 HAADF STEM images of $CuInS_2$ **(a),** $Cu_{0.45}InS_2$ **(b)** and $Cu_{0.38}InS_2$ **(c)** NCs. The scale bar is 20 nm in all panels; **(d)** Corresponding XRD patterns for the three samples, along with the bulk pattern of roquesite; **(e)** HRTEM image of a representative $CuInS_2$ NC (i.e. with 1:1 In:Cu ratio) exhibiting the $(1\bar{1}2)$ and (220) lattice sets compatible with the chalcopyrite-like structure of roquesite and showing measured d-spacing of 3.19 Å and 1.95 Å; **(f)** UV-Vis absorption and PL spectra of the same NCs as in **(a-c)**. The PL curves were obtained by exciting the samples at 450 nm; **(g-h)** High resolution XPS spectra of the three CIS NC samples as in (a-c), in the region of the Cu $2p_{3/2}$ level **(g)** and In $3d_{5/2}$ level **(h)**. The data are normalized to the intensity of the In $3d_{5/2}$ peak.

With increasing In:Cu precursor ratios, the mean size of the NCs decreased slightly (Table 7.1). The XRD patterns of all these NCs could be indexed with a tetragonal chalcopyrite-like structure (Roquesite, $CuInS_2$, JCPDS card 47-1372, see Figure 7.1d). When using a 1:1 In:Cu precursor ratio, essentially $CuInS_2$ NCs were

obtained, that is, with In:Cu:S stoichiometric ratios close to 1:1:2. This composition was assessed by ICP (Table 7.1) and also by EDS (which yielded Cu 26%, In 27% and S 48%). When higher molar In:Cu precursor ratios were used instead, both ICP (Table 7.1) and quantitative XPS analysis indicated that the NCs were Cu deficient,[53] while the In:S ratio remained very close to 2:1 (that is, the NCs had $Cu_{1-x}InS_2$ stoichiometry, as typical In:S ratios found by ICP were around 1.97-1.99:1). The XRD patterns of copper deficient CIS samples with Cu:In ratio of 0.45 and 0.38 remained consistent with roquesite pattern; moreover XRD phase identification analysis did not exhibit any other In_xS_y species (Figure 7.1d) present in the sample. Therefore, even if In was used in much excess in the synthesis, no side formation of other NCs was observed except for the CIS ones.

We carried out XPS analysis on the various NC samples in the regions of the Cu $2p_{3/2}$ and In $3d_{5/2}$ peaks. For the CIS NC sample with 1:1 In:Cu stoichiometry, the Cu $2p_{3/2}$ peak was at a binding energy of (932.3 ± 0.1) eV and the In $3d_{5/2}$ peak was at (444.9 ± 0.1) eV (Figure 7.1g-h). Moreover, in the Cu 2p region there was no evidence of shake-up satellites that are typical of Cu(II) species. These data are in good agreement with the results of Courtel et al.,[60] which suggests that Cu and In oxidation states are +1 and +3, respectively. In CIS samples with decreasing Cu stoichiometry, the Cu $2p_{3/2}$ peak slightly shifted to higher binding energies (932.5 eV for $Cu_{0.45}InS_2$ and 932.6 eV for $Cu_{0.38}InS_2$, see Figure 7.1g) without the appearance of Cu(II) related features. Also the In $3d_{5/2}$ peak slightly shifted to higher binding energies in samples with decreasing Cu stoichiometry (445.2 eV for $Cu_{0.45}InS_2$ and 445.3 eV for $Cu_{0.38}InS_2$, see Figure 7.1h). A change in the oxidation states of Cu^+ or In^{3+} would lead to larger shifts (e.g. $In^{3+} \rightarrow In^+$ = -0.8 eV; $Cu^+ \rightarrow Cu^{2+}$ = +1.1eV[61]) therefore we interpreted the observed *small* shifts as due to a modification of the chemical environment experienced by Cu and In electrons (namely the formation of a Cu deficient lattice). The position of S 2p peak maximum was instead not affected by the In:Cu stoichiometry, and was always at (162.1 ± 0.1) eV, again in agreement with literature data.[60]

The CIS NCs were characterized by typical broad optical absorption spectra and multi-peaked emission (Figure 7.1f) with a large Stokes shift with respect to the absorption, in accordance with previous works.[3,15,19,44,55] The PL peaks instead first exhibited a large blue shift when going from $CuInS_2$ to $Cu_{0.45}InS_2$, but then remained stable at 650 nm for samples with Cu stoichiometry below 0.45 (Figure 7.1f and Table 7.1). With the decrease in Cu stoichiometry (i.e.

increasing Cu vacancies) we observed an enhancement of the PL QY: this went from 7%, in the case of stoichiometric $CuInS_2$, up to 23% in the case of $Cu_{0.38}InS_2$, which appeared to be the stoichiometry that maximized the QY of our NCs (Table 7.1). A further decrease in copper stoichiometry, in fact, resulted in less photoluminescent NCs. PL decay times were measured in order to get more insight into the nature of the emitting states and of the surface passivation. The PL decay curves of the CIS NCs (Figure 7.3b) could be fitted by a sum of two exponentials, from which two time constants (Table 7.1) were derived: a long time contribution, which is consistent with previous reports on CIS NCs,[3,17,57] and a short decay component which is probably related to a non-radiative recombination channel. We remark that, while the In:Cu ratio had a strong influence on the QY, it did not have much effect on both time components. The short time component in all our CIS NCs was longer than that reported recently by Li et al.[17] on CIS NCs with 1:1 In:Cu ratio and similar to the short time component measured by Kim et al. in $Cu_{1-x}InS_2$ NCs.[58]

7.3 Synthesis of Cu-In-Zn-S QDs

The crude solution obtained from the synthesis of CIS QDs was heated at 120°C (still under inert atmosphere) and then a solution of Zinc stearate (0.4 mmol) dissolved in 5 ml of ODE and 0.5ml of TOP was added dropwise. The temperature was then raised to 210°C for 90 minutes (this last step was crucial for improving the PL QY), after which the flask was cooled to room temperature and the NCs were then separated by addition of ethanol followed by centrifugation. The NCs were washed three times by repeated dissolution in toluene and re-precipitation in ethanol. This procedure leaded to NCs with a quaternary composition. What actually varied significantly in these "CIZS" NC samples was the Cu stoichiometry, while the In:Zn and In:S ratios varied much less (Table 7.2).

In:Cu precursor	CIZS Composition	Size (nm)	λ_{em} (nm)	QY (%)	PL decay (ns)
1 : 1	$Cu_{0.7}In_{0.77}Zn_{0.85}S_2$	2.7 ±0.7	640	54	202
4 : 1	$Cu_{0.26}In_{0.8}Zn_{0.72}S_2$	2.6±0.8	600	68	198
8 : 1	$Cu_{0.13}In_{0.74}Zn_{0.59}S_2$	2.7 ±0.7	590	80	197

Figure 7.2 Relevant parameters for syntheses of CIZS NCs. The CIZS composition was measured by ICP. λ_{em} is the wavelength corresponding to the maximum of the emission peak exciting at 450 nm.

XRD patterns of all samples were characterized by slight shifts towards higher 2Θ (i.e. smaller d-spacing) with respect to those of the roquesite phase (Figure 7.2a). Not much size variation of these NCs with respect to their parent CIS NCs was appreciated by HAADF STEM analysis (see Tables 7.1 and 7.2). Figure 7.2b is a HRTEM image of a representative particle from a sample with 1:1 In:Cu ratio. The lattice fringes here are compatible with typical lattice sets $(1\bar{1}2)$ and (220) of chalcopyrite-like structure, showing d-spacings and vector relationships consistent with the quaternary roquesite system $Cu_{0.41}In_{0.41}Zn_{0.18}S$ (JCPDS card 47-1371) (Figure 7.2b).

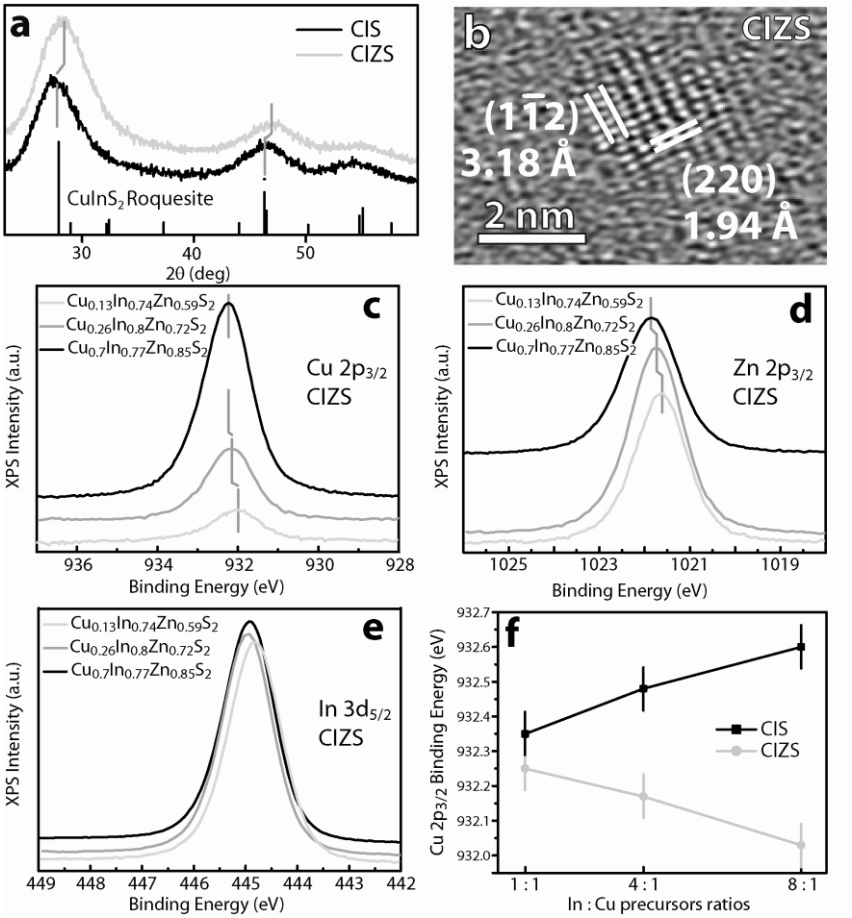

Figure 7.3 **(a)** Detail of the (112), (204) and (312) XRD reflections of CIS and CIZS NCs obtained starting from In:Cu=1:1 precursor ratio: a shift to higher 2Θ of the CIZS peaks with respect to the CIS phase is evident. **(b)** HRTEM image of a representative CISZ NC obtained using a In:Cu ratio of 1:1, and exhibiting both the typical $(1\bar{1}2)$ and (220) lattice sets compatible with the chalcopyrite-like structure, with d-spacing of 3.18Å and 1.94Å, respectively; **(c-e)** XPS characterization of CIZS NCs. The data are shown after normalization to the intensity of the In $3d_{5/2}$ peak. High resolution spectra of **(c)** CIZS Cu $2p_{3/2}$ level, **(d)** CIZS Zn $2p_{3/2}$ level and **(e)** CIZS In $3d_{5/2}$ level showing peak positions shifts vs. In:Cu ratio. In panel **(f)**, the observed Cu $2p_{3/2}$ position trends for CIS and CIZS are compared.

It is clear on the other hand that neither XRD nor HRTEM can be conclusive on the actual crystal phase of these NCs, as the broad XRD patterns observed by us and the lattice sets seen under HRTEM can be compatible with a wide set of materials. Chemical analysis of many particles of this sample, performed via STEM-EDS, yielded elemental quantifications of Cu 19%, In 19%, Zn 16%, S 46%, which is in line with the chemical composition found by ICP.

Quantitative XPS analysis on the CIZS NCs corroborated the chemical composition found by ICP and EDS. Also, the Cu $2p_{3/2}$ peak of the CIZS samples was generally shifted to lower energies with respect to that of their parent CIS samples. It is noteworthy that, contrary to what was found for the parent CIS NCs, the Cu $2p_{3/2}$ peak of the CIZS NCs moved actually to *lower* binding energies with increasing In:Cu ratio (i.e. decreasing Cu stoichiometry, see Figure 7.2, panels c and f). On the other hand, the In $3d_{5/2}$ peak position was less affected this time by the Cu stoichiometry (Figure 7.2d), while the new Zn $2p_{3/2}$ peak also moved to lower binding energies with decreasing Cu content (Figure 7.2e). As shown by Nam et al.,[62] the position of the Cu $2p_{3/2}$ peak should not change due to shell growth. The Cu peak shifts are then more likely related to the incorporation of Zn^{2+} ions in the CIS lattice, in analogy with what already observed by Fukuzaki et al. on Na incorporation in copper deficient $CuInS_2$ thin films[63] (see also the discussion section).

Both optical absorption and PL spectra of the CIZS NCs were blue-shifted with respect to those of their parent CIS NCs (Figure 7.3). The PL decay curves (Figure 7.3c) of all the various CIZS NCs could be fitted by single exponentials. In this case only the long time component was observed (Table 7.2). The suppression of the short decay component is consistent with the considerable improvement in the QY of these samples over the CIS NCs, reaching record values up to 80% for $Cu_{0.13}In_{0.74}Zn_{0.59}S_2$ NCs (Table 7.2).

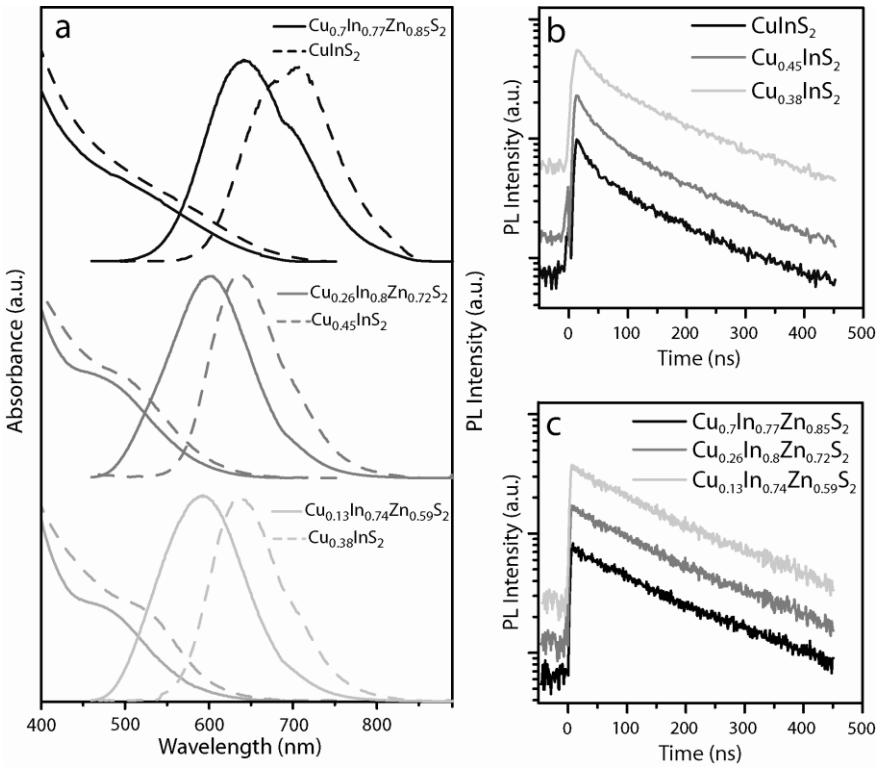

Figure 7.4 **(a)** Comparison of the PL and UV-vis absorption spectra of the CIZS NCs with those of their parent CIS NCs. The absorption and emission curves of the parent CIS NCs have been included as dashed lines to underline the blue shift of both the absorption and emission peaks after the partial cation exchange process. The PL curves were obtained by exciting at 450 nm. (b-c) PL lifetime decays of the CIS **(b)** and CIZS **(c)** NCs.

7.4 Discussion

7.4.1. $Cu_{1-x}InS_2$ NCs

From XRD, ICP and XPS it is clear that Cu-defective CIS NCs could be obtained by varying the molar ratio of In and Cu precursors. The broad absorption spectra and the presence of multi-peaked emission (Figure 7.1f) are usually due to the presence of intra band gap states, as already discussed in various works.[3,15,19,44,55] In bulk CIS, it has been established that a Sulfur vacancy (V_S), an interstitial Copper (Cu_i) and an Indium substituted at a Copper site (In_{Cu}) are donor states, while a Copper vacancy (V_{Cu}), an Indium interstitial (In_i) and a Copper substituted at an Indium site (Cu_{In}) are acceptor states. In small NCs of around 3 nm, most of the atoms are close to the surface and, as far as we know, no information is available on how these defects states are modified by the close

proximity to the surface. M. Uehara et al.[55] and recently Nam et al.[19] were able to tune the band gap and to improve the PL QY of their CIS NCs up to 50% by increasing the In:Cu ratio, thus presumably increasing the number of Copper vacancies. Given the small reduction of the NCs diameter with decreasing Copper content in our CIS samples (Table 7.1), the observed blue shift in absorption is probably not mainly due to quantum confinement effects, but rather to a widening of the band gap due to a lowering in energy of the valence band edge.[19,55] This is possibly related to strong p-type self-doping from the introduction of a large amount of copper vacancies, as in $CuInSe_2$,[64] where the typical Burstein-Moss shift of the optical absorption in strongly p-doped samples has been reported.[65] The introduction of Cu vacancies also raised the emission peak component around 650 nm (Figure 7.1f). Thus, this emission has been consistently attributed to the conduction band to Copper vacancy recombination. Instead, emission peaks at longer wavelength have been associated to donor-acceptor recombination.[19,55] This is also in agreement with an increase in the PL QY from 7%, in the case of stoichiometric CIS, up to 23%, in the case of $Cu_{0.38}InS_2$ for which the PL QY was the highest.

Also, considering the PL dynamics of the CIS NCs, in which the fast decay component can be related to a non-radiative recombination channel, the long time contribution is consistent with both donor-acceptor recombination and conduction-band to acceptor recombination. The fact that both the long and short time decay constants are not really dependent on the In:Cu ratio, while the QY is strongly dependent on it, suggests a dynamical picture of the excitation relaxation in which early branching takes place into independent decay channels which are either dark or bright. Several bright channels with different recombination rates and QYs would thus rationalize the results. Alternatively, the very small size of the NCs suggests that even single defects could change abruptly the physical properties of the NCs, resulting in a population of NCs with strong inhomogeneities of the optical properties, in particular concerning recombination and optical emission.

7.4.2. Cu-In-Zn-S NCs

Our data are also consistent with a conversion of CIS NCs into CIZS NCs upon their reaction with Zn^{2+} and we can exclude that these particles had a core/shell structure formed by a CIS core embedded in a ZnS shell. First, no increase in size was observed by HAADF STEM analysis after the reaction of CIS NCs with Zn^{2+} cations (tab 7.1-7.2), which would have been one of the most

striking indications of core-shell formation.[3,17,19,57] Even a ZnS shell 0.16 nm thick (corresponding to {222} ZnS monolayer), continuous or patched, partially covering the CIS NCs (50% of total crystal surface, in order to maintain the ratio Zn:In=1) would have resulted in a noticeable increase in size (we also did some estimates based on models, which are reported in next session "3D atomic modelling").

A strong support for a quaternary alloy structure instead of a core/shell structure comes from XPS. In the case of core/shell NCs, XPS would have been affected by the layered structure of the system. A case study is the recent work of Nam et al.[62] on core/shell CIS/ZnS NCs, in which the presence of even 1.0 – 1.5 monolayers of ZnS shell induced a large attenuation of the intensity of the Cu peaks (around 50%) and resulted in wrong XPS evaluations of the relative atomic ratios. Nam et al.[62] reported indeed a Zn:Cu ratio of 22.5 as estimated by XPS, while the actual ratio, estimated by EDS, was 6.2. In our case, by quantitative XPS analysis on the CIZS NCs we found In:Cu and In:Zn ratios that were in line with those found by both ICP and EDS.

Further support on the alloy composition came by comparing high resolution XPS of the CIS NCs (Figure 7.1g-h) with those of the CIZS NCs (Figure 7.2c-f). For example, the position of the Cu $2p_{3/2}$ peak should not change after a shell is grown on the cores (see also ref.[62]). In our case instead a shift was clearly observed, which was most likely related to the modification of the crystal lattice due to Zn^{2+} ions entering the CIS structure and partially replacing In^{3+} and Cu^{+} ions. The preferential extraction of Copper that occurred during the exchange (see Table 7.1 and 7.2) can be explained by taking into account that the Cu-S bond is much weaker than the In-S bond[45] and by the fact that the Zn substitution of Cu has been shown to be energetically favourable.[44]

Optical measurements in Figure 7.3a revealed a slight blue-shift of the absorbance bands upon the formation of the CIZS NCs. Park et al.[57] suggested that, upon overcoating the CIS cores using a Zn salt precursor, a partial cation exchange occurred whereby Zn^{2+} replaces In^{3+} and Cu^{+}. This would reduce the size of the core, resulting in a blue shift of both absorption and emission. However, such a blue shift in the absorption bands is not always observed upon shell growth,[19] suggesting that the effect is clearly dependent on the nature of the CIS cores and/or on the coating procedure. From the structural characterization, we may reasonably exclude the formation of a shell and the reduction of the core size. Thus, the blue shift can be attributed to the widening

of the band gap due to the entrance of zinc ions into the CIS structures, as already observed in doping CIS thin films with Zinc[66] and in Cu-In-Zn-S solid solutions.[46,47] On the other hand, we cannot completely exclude a not homogeneous Zn distribution inside the CIZS NCs. Unfortunately, the sizes of the present NCs were too small for allowing a compositional profile in the TEM (see Supporting Information for more details on this point).

Regarding the emission spectra, for all compositions we noticed a relevant blue shift in the emission of the CIZS NCs with respect to their parent CIS NCs (of about 50 nm), which seems to be related to the blue shift of the absorption bands, as shown in Figure 7.3. Kim et al.[58] observed for their Cu-deficient $Cu_{0.2}InS_2$ NCs that, upon the growth of a ZnS shell the blue shift of the emission peak (~300meV) was much more significant than the shift in the absorption spectrum (*an effect that the authors attributed to a tighter size distribution*). On the other hand, in our Cu-deficient systems the same blue shift of ~200meV was observed in both emission and absorption spectra (Figure 7.3) in the conversion of $Cu_{0.38}InS_2$ into $Cu_{0.13}In_{0.74}Zn_{0.59}S_2$, which is an indication of their different nature compared to those obtained by Kim et al. upon shell growth.[30] Moreover, we noticed an increase in the relative ratio of the high energy component over the low energy component in the PL of each CIZS NC sample with respect to the PL of its parent CIS NC sample (Figure 7.3). The change of the PL decay times in the CIZS NCs with respect to the CIS NCs is also consistent with a change of composition, i.e. a change of the ternary into a quaternary system. However, as this change is not very large, we argue that the radiative decay channel is possibly the same in the two systems, e.g. conduction band to Copper vacancy recombination. Also in the quaternary system, in analogy to what we observed for the ternary system, the negligible dependence of these recombination times on the In:Cu ratio, despite a non-negligible variation of the QY, suggests a similar dynamical picture of the relaxation of excitations. Here the absence of the fast decay channel, and the lower QY of the bare CIS NCs where this channel is present, suggests that this fast decay channel features a lower QY with respect to the slower decay channel, i.e. the fast channel is plagued by non-radiative recombination. A relative reduction of the lower energy emission shoulders with respect to the main emission peaks upon cation exchange suggests that the introduction of Zn in the CIS lattice preferentially passivates some donor defects, and that the fast, lossy decay channels are related to these defects. Given the poor knowledge of the nature of these defects in these very small NCs dominated by the surface, we may only make some hypothesis: Zn may be filling vacancy sites,

or, expulsion of interstitial atoms occurs during cation exchange. Both mechanisms are compatible with the observed absence of a relevant variation of the NC volume.

7.4.3. 3D Atomic Modeling of CIZS structures

Starting from the experimental observations of crystal size and shape, we built a 3D atomic model of a roquesite crystal which exhibits tetrahedral habit with 3 nm side (Figure 7.5). This crystal has a total volume of 3.12 nm^3 $\left(V = \frac{112\sqrt{3}}{32}\right)$ and contains about 180 atoms of Cu, 180 of In and 360 of S.

If a {222} monolayer of ZnS sphalerite with a thickness of at least 0.16 nm, containing 91 atoms of Zn, coats all four facets of roquesite crystal, forming a continuous shell, the total amount of Zn atoms would be 364 atoms. In this case the atomic ratio Zn:In will be 2, but this value disagrees totally with the experimental atom ratio Zn:In of 0.8, calculated from the STEM-EDX quantifications. Figure 7.5 displays the atomic models of tetrahedral roquesite crystal ($CuInS_2$) and {222} sphalerite slice (ZnS), respectively. Figure 7.6 shows schematically the growth process of a continuous ZnS shell on roquesite crystal with total covering.

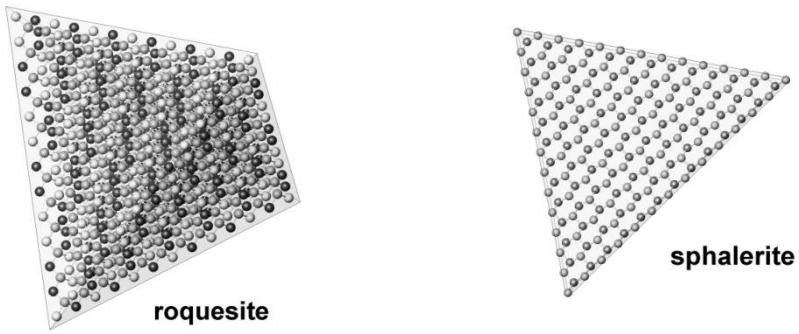

Figure 7.5 Atomic 3D model of a tetrahedral crystal of roquesite (3 nm width) and a {222} slab of sphalerite (0.16 nm thick)

The only way to obtain a ratio Zn:In=1 would be the growth of a continuous shell or a patched shell, both formed by {222} ZnS islands 0.16 nm thick, that cover 50% of the whole crystal surface (Figure 7.7). In both cases the

particles diameter would increase, but no size variation occurred via HAADF STEM image assessment.

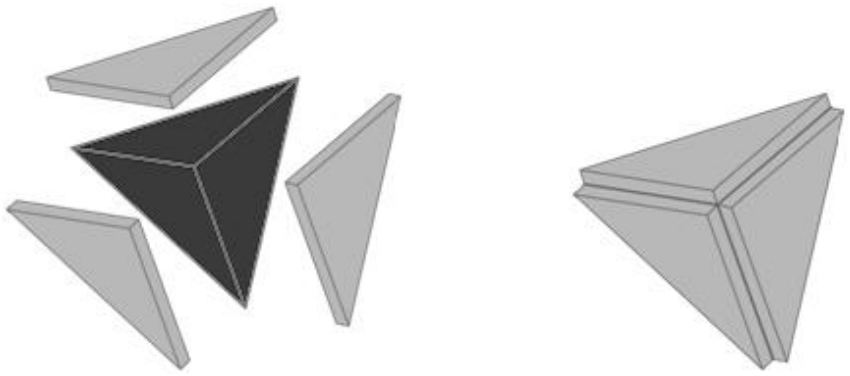

Figure 7.6 Morphological schema showing the growth of a continuous shell with total covering; {222} ZnS slices in gray and roquesite crystal in dark gray.

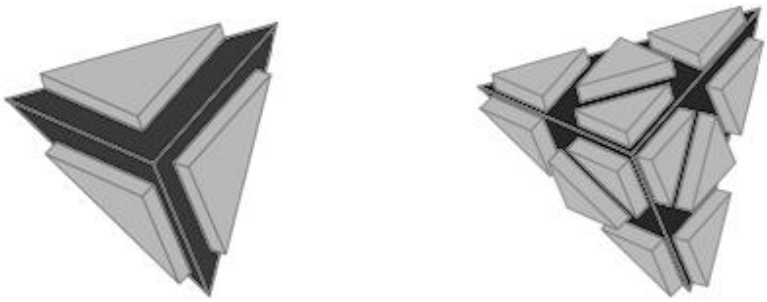

Figure 7.7 Morphological schema showing the growth of continuous (left) and patched (right) {222} ZnS shells with partial covering of 50% of the total crystal surface; ZnS in gray, roquesite in dark gray.

From a crystallographic point of view it is evident that the unit cell of ZnS sphalerite (***a***= 5.4 Å) is compatible with half unit cell of roquesite (***a***=***b***=5.52 Å, ***c***=11.14 Å), as shown in Figure 7.8. In particular, both phases exhibit the same S anionic framework and equivalent cation crystallographic sites filled by atoms with ionic radius not so different (Cu^{1+}=0.96Å, In^{3+}=0.81 Å and Zn^{2+}=0.74 Å). For these reasons the Zn atoms can give rise to a partial substitution of Cu and In atoms in roquesite producing a mixed Cu-In-Zn-S phase with chalcopyrite-like structure instead of a core/shell structure roquesite/sphalerite, as confirmed from all experimental characterizations carried out on CIZS NCs.

7.5 CIZS-PMMA Polymer Nanocomposites

In order to exploit these promising nanocrystals for lighting applications, bulk CIZS-PMMA nanocomposites containing were synthesized through bulk polymerization techniques. In a typical polymerization process a desired amount of QDs was added to a 10^{-3}M solution of Azobisisobutyronitrile (AIBN) in methyl methacrylate (MMA) and the resulting mixture was heated to 60°C under N_2 for 36 hours. The resulting bulk solid composite was further heated at 95°C for 12 hours for the curing process. After the polymerization process the resulting nanocomposites of about 2.5cm diameter and 0.5cm thickness, exhibited strong fluorescence, as shown in figure 7.8. This indicated that our new systems were able to withstand the attack of radical initiators on the contrary to what observed with InP/ZnS QDs. The materials retained their fluorescence even after some months indicating that the polymer matrix was able to protect the NCs against the oxidative atmosphere.

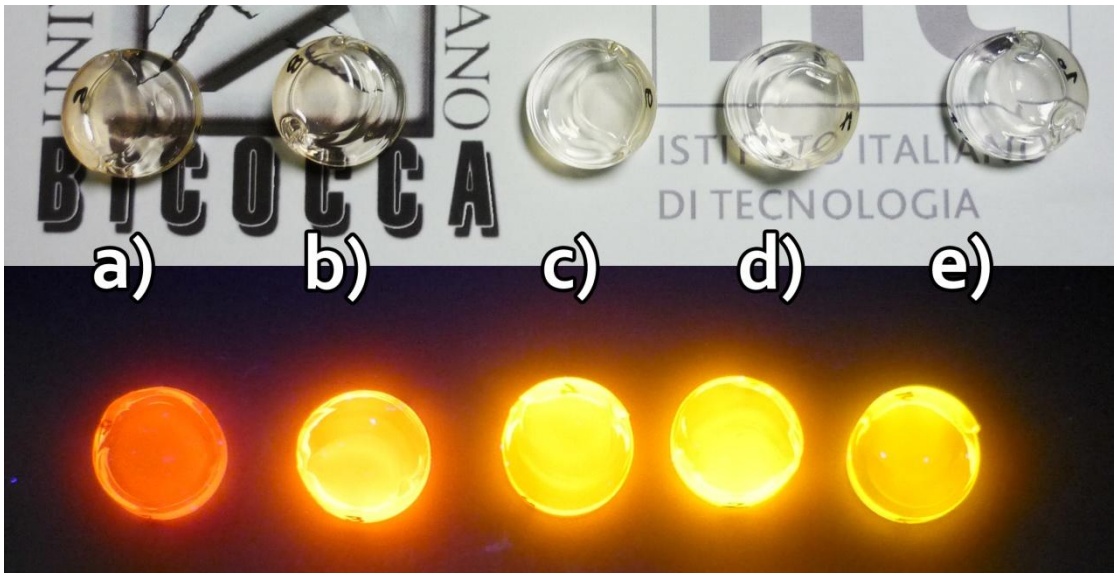

Figure 7.8 Bulk polymer nanocomposites made of PMMA and a) $Cu_{0.7}In_{0.77}Zn_{0.85}S_2$ b) $Cu_{0.42}In_{0.71}Zn_{0.64}S_2$ c) $Cu_{0.26}In_{0.8}Zn_{0.72}S_2$ d) $Cu_{0.18}In_{0.65}Zn_{0.52}S_2$ and e) $Cu_{0.13}In_{0.74}Zn_{0.59}S_2$ nanocrystals. In the upper image the samples are shown under sunlight. In the lower image the nanocomposites were illuminated with an UV lamp (λ=450nm). The diameter of every single thick disk is 2.5cm.

Further analyses are still necessary in order to characterize the properties of the final materials. Optical studies are still in process with the aim of understanding the emission properties of these nanocomposites as well as their fluorescence QY.

7.6 Conclusions

In summary, we set up a two-step synthesis route to strongly fluorescent CIZS NCs reaching a QY up to 80%. In the first step we obtained Cu-deficient CIS NCs by varying the initial amount of In:Cu precursors. We found that the stoichiometry that maximizes the luminescence is $Cu_{0.38}InS_2$. TEM, ICP and XPS analysis indicated that our procedure allows for a good control over the stoichiometry of the quaternary CIZS NCs that is probably hard to achieve otherwise; namely while the In:Zn:S ratio stays almost fixed, the amount of Copper could be tuned in the final structures. The formation of CIZS NCs resulted into a blue shift of both the PL and absorption and the disappearance of the short time decay components in time-resolved PL. This leaded to more efficient systems which shown enhanced PL QY.

CIZS QDs were robust enough to withstand the bulk polymerization process in MMA. Bulk PMMA-CIZS nanocomposites with strong fluorescence were synthesized under inert atmosphere. The resulting systems are potentially extremely useful for the *warm white light* project. It is important to remind that these systems, in fact, are non toxic, highly fluorescent and that the stokes shift characterizing these QDs is very high. This last property is fundamental for an efficient conversion of the blue light avoiding unpleasant "self-absorption" processes (see chapter 4.2.2).

7.7 References

[1] Talapin, D.V., et al., Prospects of Colloidal Nanocrystals for Electronic and Optoelectronic Applications, *Chemical Reviews*, **2009**, 110(1): p. 389-458.

[2] Pons, T., et al., Cadmium-Free CuInS2/ZnS Quantum Dots for Sentinel Lymph Node Imaging with Reduced Toxicity, *ACS Nano*, **2010**, 4(5): p. 2531-2538.

[3] Li, L., et al., Highly Luminescent CuInS2/ZnS Core/Shell Nanocrystals: Cadmium-Free Quantum Dots for In Vivo Imaging, *Chemistry of Materials*, **2009**, 21(12): p. 2422-2429.

[4] Hussain, S., et al., One-Pot Fabrication of High-Quality InP/ZnS (Core/Shell) Quantum Dots and Their Application to Cellular Imaging, *ChemPhysChem*, **2009**, 10(9-10): p. 1466-1470.

[5] Panthani, M.G., et al., Synthesis of CuInS2, CuInSe2, and Cu(InxGa1-x)Se2 (CIGS) Nanocrystal "Inks" for Printable Photovoltaics, *Journal of the American Chemical Society*, **2008**, 130(49): p. 16770-16777.

[6] Li, L., N. Coates, and D. Moses, Solution-Processed Inorganic Solar Cell Based on in Situ Synthesis and Film Deposition of CuInS2 Nanocrystals, *Journal of the American Chemical Society*, **2009**, 132(1): p. 22-23.

[7] Nanu, M., J. Schoonman, and A. Goossens, Nanocomposite Three-Dimensional Solar Cells Obtained by Chemical Spray Deposition, *Nano Letters*, **2005**, 5(9): p. 1716-1719.

[8] Guo, Q., et al., Development of CuInSe2 Nanocrystal and Nanoring Inks for Low-Cost Solar Cells, *Nano Letters*, **2008**, 8(9): p. 2982-2987.

[9] Arici, E., N.S. Sariciftci, and D. Meissner, Hybrid Solar Cells Based on Nanoparticles of CuInS2 in Organic Matrices, *Advanced Functional Materials*, **2003**, 13(2): p. 165-171.

[10] Scheer, R., et al., CuInS2 based thin film solar cell with 10.2% efficiency, *Applied Physics Letters*, **1993**, 63(24): p. 3294-3296.

[11] Contreras, M.A., M.J. Romero, and R. Noufi, Characterization of Cu(In,Ga)Se2 materials used in record performance solar cells, *Thin Solid Films*, **2006**, 511-512(0): p. 51-54.

[12] AbuShama, J.A.M., et al., Properties of ZnO/CdS/CuInSe2 solar cells with improved performance, *Progress in Photovoltaics: Research and Applications*, **2004**, 12(1): p. 39-45.

[13] Castro, S.L., et al., Nanocrystalline Chalcopyrite Materials (CuInS2 and CuInSe2) via Low-Temperature Pyrolysis of Molecular Single-Source Precursors. *Chemistry of Materials*, **2003**, 15(16): p. 3142-3147.

[14] Chang, H.-Y., et al., Ionic compounds lamination reaction and characteristics of photosensitive copper indium sulfide on titania nanotube arrays, *Journal of Alloys and Compounds*, **2011**, 509(35): p. 8700-8706.

[15] Castro, S.L., et al., Synthesis and Characterization of Colloidal CuInS2 Nanoparticles from a Molecular Single-Source Precursor, *The Journal of Physical Chemistry B*, **2004**, 108(33): p. 12429-12435.

[16] Li, C., et al., Highly Luminescent Water-Soluble InP/ZnS Nanocrystals Prepared via Reactive Phase Transfer and Photochemical Processing, *The Journal of Physical Chemistry C*, **2008**, 112(51): p. 20190-20199.

[17] Li, L., et al., Efficient Synthesis of Highly Luminescent Copper Indium Sulfide-Based Core/Shell Nanocrystals with Surprisingly Long-Lived Emission. *Journal of the American Chemical Society*, **2011**. 133(5): p. 1176-1179.

[18] Li, L. and P. Reiss, One-pot Synthesis of Highly Luminescent InP/ZnS Nanocrystals without Precursor Injection. *Journal of the American Chemical Society*, **2008**. 130(35): p. 11588-11589.

[19] Nam, D.-E., W.-S. Song, and H. Yang, Noninjection, one-pot synthesis of Cu-deficient CuInS2/ZnS core/shell quantum dots and their fluorescent properties. *Journal of Colloid and Interface Science*, **2011**. 361(2): p. 491-496.

[20] Xie, R., et al., InAs/InP/ZnSe core/shell/shell quantum dots as near-infrared emitters: Bright, narrow-band, non-cadmium containing, and biocompatible. *Nano Research*, **2008**. 1(6): p. 457-464.

[21] Xie, R. and X. Peng, Synthetic Scheme for High-Quality InAs Nanocrystals Based on Self-Focusing and One-Pot Synthesis of InAs-Based Core–Shell Nanocrystals. *Angewandte Chemie International Edition*, **2008**. 47(40): p. 7677-7680.

[22] Xie, R., M. Rutherford, and X. Peng, Formation of High-Quality I−III−VI Semiconductor Nanocrystals by Tuning Relative Reactivity of Cationic Precursors. *Journal of the American Chemical Society*, **2009**. 131(15): p. 5691-5697.

[23] Ryu, E., et al., Step-Wise Synthesis of InP/ZnS Core−Shell Quantum Dots and the Role of Zinc Acetate. *Chemistry of Materials*, **2009**. 21(4): p. 573-575.

[24] Zhang, J., R. Xie, and W. Yang, A Simple Route for Highly Luminescent Quaternary Cu-Zn-In-S Nanocrystal Emitters. *Chemistry of Materials*, **2011**. 23(14): p. 3357-3361.

[25] Ziegler, J., et al., Silica-Coated InP/ZnS Nanocrystals as Converter Material in White LEDs. *Advanced Materials*, **2008**. 20(21): p. 4068-4073.

[26] Izquierdo-Roca, V., et al., Assessment of absorber composition and nanocrystalline phases in CuInS2 based photovoltaic technologies by ex-situ/in-situ resonant Raman scattering measurements. *Solar Energy Materials and Solar Cells*, **2011**. 95, Supplement 1(0): p. S83-S88.

[27] Todorov, T., et al., Progress towards marketable earth-abundant chalcogenide solar cells. *Thin Solid Films*, **2011**. 519(21): p. 7378-7381.

[28] Shavel, A., et al., Continuous Production of Cu2ZnSnS4 Nanocrystals in a Flow Reactor. *Journal of the American Chemical Society*, **2012**. 134(3): p. 1438-1441.

[29] Redinger, A., et al., Route Toward High-Efficiency Single-Phase Cu 2ZnSn(S,Se)4 Thin-Film Solar Cells: Model Experiments and Literature Review. *IEEE Journal of Photovoltaics*, **2011**.

[30] Kim, H., et al., Characteristics of CuInS2/ZnS quantum dots and its application on LED. *Journal of Crystal Growth*, **2011**. 326(1): p. 90-93.

[31] Dai, Q., C.E. Duty, and M.Z. Hu, Semiconductor-Nanocrystals-Based White Light-Emitting Diodes. *Small*, **2010**. 6(15): p. 1577-1588.

[32] Chen, L., et al., Controllable synthesis of functionalized CdS nanocrystals and CdS/PMMA nanocomposite hybrids. *European Polymer Journal*, **2007**. 43(11): p. 4593-4601.

[33] Chung, W., et al., White emission using mixtures of CdSe quantum dots and PMMA as a phosphor. *Optical Materials*, **2010**. 32(4): p. 515-521.

[34] Lee, J., et al., Full Color Emission from II–VI Semiconductor Quantum Dot–Polymer Composites. *Advanced Materials*, **2000**. 12(15): p. 1102-1105.

[35] Song, H. and S. Lee, Photoluminescent (CdSe)ZnS quantum dot–polymethylmethacrylate polymer composite thin films in the visible spectral range. *Nanotechnology*, **2007**. 18(5): p. 055402.

[36] Woo, J.Y., et al., Enhanced Photoluminance of Layered Quantum Dot–Phosphor Nanocomposites as Converting Materials for Light Emitting Diodes. *The Journal of Physical Chemistry C*, **2011**. 115(43): p. 20945-20952.

[37] Brian, A.A., et al. Nanophosphors Based on CdSe/ZnS and CdSe/SiO2 Colloidal Quantum Dots for Daylight-Quality White LEDs. *Optical Society of America*. **2010**.

[38] Demir, H.V., et al., Tuning shades of white light with multi-color quantum-dot–quantum-well emitters based on onion-like CdSe–ZnS heteronanocrystals. *Nanotechnology*, **2008**. 19(33): p. 335203.

[39] Nizamoglu, S., et al., Warm-white light-emitting diodes integrated with colloidal quantum dots for high luminous efficacy and color rendering. *Opt. Lett.*, **2010**. 35(20): p. 3372-3374.

[40] Wang, H., et al., White light emitting diodes realized by using an active packaging method with CdSe/ZnS quantum dots dispersed in photosensitive epoxy resins. *Nanotechnology*, **2008**. 19(14): p. 145202.

[41] Jang, E., et al., White-Light-Emitting Diodes with Quantum Dot Color Converters for Display Backlights. *Advanced Materials*, **2010**. 22(28): p. 3076-3080.

[42] Mao, B., et al., Synthesis and Photophysical Properties of Ternary I–III–VI AgInS2 Nanocrystals: Intrinsic versus Surface States. *The Journal of Physical Chemistry C*, **2011**. 115(18): p. 8945-8954.

[43] Devaney, W.E., et al., Structure and properties of high efficiency ZnO/CdZnS/CuInGaSe2 solar cells. *IEEE Transactions on Electron Devices*, **1990**. 37(2): p. 428-433.

[44] Nakamura, H., et al., Tunable Photoluminescence Wavelength of Chalcopyrite CuInS2-Based Semiconductor Nanocrystals Synthesized in a Colloidal System. *Chemistry of Materials*, **2006**. 18(14): p. 3330-3335.

[45] Yamamoto, T., et al., Differences in the electronic structure and compensation mechanism between n-type Zn- and Cd-doped CuInS2 crystals. *Physica B: Condensed Matter*, **1999**. 273-274(0): p. 927-929.

[46] Wang, X., et al., A General Synthesis of Cu−In−S Based Multicomponent Solid-Solution Nanocrystals with Tunable Band Gap, Size, and Structure. *The Journal of Physical Chemistry C*, **2010**. 114(41): p. 17293-17297.

[47] Pan, D., et al., Alloyed semiconductor nanocrystals with broad tunable band gaps. *Chemical Communications*, **2009**(28): p. 4221-4223.

[48] Nairn, J.J., et al., Preparation of Ultrafine Chalcopyrite Nanoparticles via the Photochemical Decomposition of Molecular Single-Source Precursors. *Nano Letters*, **2006**. 6(6): p. 1218-1223.

[49] Feng, J., et al., A facile approach to synthesize high-quality ZnxCuyInS1.5+x+0.5y nanocrystal emitters. *Chemical Communications*, **2011**. 47(22): p. 6422-6424.

[50] Zhong, H., et al., Controlled Synthesis and Optical Properties of Colloidal Ternary Chalcogenide CuInS2 Nanocrystals. *Chemistry of Materials*, **2008**. 20(20): p. 6434-6443.

[51] Pan, D., et al., Synthesis of Cu−In−S Ternary Nanocrystals with Tunable Structure and Composition. *Journal of the American Chemical Society*, **2008**. 130(17): p. 5620-5621.

[52] Tang, J., et al., Synthesis of Colloidal CuGaSe2, CuInSe2, and Cu(InGa)Se2 Nanoparticles. *Chemistry of Materials*, **2008**. 20(22): p. 6906-6910.

[53] Batabyal, S.K., et al., Phase-Selective Synthesis of CuInS2 Nanocrystals. *The Journal of Physical Chemistry C*, **2009**. 113(33): p. 15037-15042.

[54] Wang, D., et al., General synthesis of I-III-VI2 ternary semiconductor nanocrystals. *Chemical Communications*, **2008**(22): p. 2556-2558.

[55] Uehara, M., et al., Synthesis of CuInS2 fluorescent nanocrystals and enhancement of fluorescence by controlling crystal defect. *The Journal of Chemical Physics*, **2008**. 129(13): p. 134709.

[56] Nose, K., et al., Synthesis of Ternary CuInS2 Nanocrystals; Phase Determination by Complex Ligand Species. *Chemistry of Materials*, **2009**. 21(13): p. 2607-2613.

[57] Park, J. and S.-W. Kim, CuInS2/ZnS core/shell quantum dots by cation exchange and their blue-shifted photoluminescence. *Journal of Materials Chemistry*, **2011**. 21(11): p. 3745-3750.

[58] Kim, Y.-K., et al., The photoluminescence of CuInS2 nanocrystals: effect of non-stoichiometry and surface modification. *Journal of Materials Chemistry*, **2012**. 22(4).

[59] Williams, A.T.R., S.A. Winfield, and J.N. Miller, Relative fluorescence quantum yields using a computer-controlled luminescence spectrometer. *Analyst*, **1983**. 108(1290): p. 1067-1071.

[60] Courtel, F.M., et al., Synthesis, Characterization, and Growth Mechanism of n-Type CuInS2 Colloidal Particles. *Chemistry of Materials*, **2009**. 21(16): p. 3752-3762.

[61] NIST X-ray Photoelectron Spectroscopy Database

[62] Nam, D.-E., W.-S. Song, and H. Yang, Facile, air-insensitive solvothermal synthesis of emission-tunable CuInS2/ZnS quantum dots with high quantum yields. *Journal of Materials Chemistry*, **2011**. 21(45): p. 18220-18226.

[63] Fukuzaki, K., et al., Changes in the electronic structure of CuInS2 thin films by Na incorporation. *Applied Physics Letters*, **1998**. 73(10): p. 1385-1387.

[64] Zhang, S.B., et al., Defect physics of the CuInSe2 chalcopyrite semiconductor. *Physical Review B*, **1998**. 57(16): p. 9642-9656.

[65] Chattopadhyay, K.K., et al., Burstein-Moss shift in CulnSe2 films. *Vacuum*, **1991**. 42(14): p. 915-918.

[66] Ben Rabeh, B., M. Kanzari, and B. Rezig, Effect of Zinc Incorporation in CuInS2 Thin Films Grown by Vacuum Evaporation Method, *Acta Physica Polonica*, **2009**. 115(3): p. 699-703.

Nb-Doped TiO_2 Nanocrystals

8.1 Introduction

In the last few years the use of transparent conducting oxides (TCOs) has lead to a rapid development of many interesting devices such as flat panel displays (FPDs), smart displays (i.e. touch panels), light-emitting devices (LEDs), organic light-emitting devices (OLEDs), elctrochromic windows and thin film photovoltaics (PV)[1-5]. Among the TCOs Sn-doped In_2O_3 (ITO) and F-doped SnO_2 have mostly been used because of their excellent visible transparency and conducting properties[1,6]. Due to the increasing industrial demand of these materials the current research is mainly focused on new compounds based on earth abundant elements as sustainable alternatives. Alluminum-doped ZnO_2 (AZO) has been show to be a valid inexpensive and non scarce alternative to ITO [2,7,8]. At the same time the industrial need for high-efficency devices requires a broader range of TCOs with specific optical properties. For example high refractive index TCOs are needed to increase the external quantum efficiency of blue GaN LEDs [9-13] while compounds with enhanced VIS-NIR transparency and low resistivity can be used in transparent electrodes to improve the efficiency of solar cells[1,3,13,14]. In addition to the required electrical and optical characteristics, applied TCO materials should be stable in hostile environment containing acidic and alkali solutions, oxidizing and reducing atmospheres and elevated temperature.

Lately Nb-doped TiO_2 (NTO) with its low cost, non toxicity, abundance, thermal and chemical stability (especially in reducing atmosphere) has received significant attention as a new promising alternative to ITO. It has been shown, in fact, that NTO can exhibit an electron conducibility that is comparable to that of ITO while retaining high optical transmittance in both visibile and IR regions [12-20]. Moreover NTO possesses a relatively high refractive index which is especially appropriate for being used in transparent electrodes for solar cells and GaN-based LEDs[11,12].

So far Nb-doped TiO_2 has been obtained in form of films through mainly pulsed laser deposition (PLD) [13-15, 17, 21-23], sputtering [24-26] and sol-gel[16] techniques. Much less effort has been spent on the synthesis and characterization of NTO nanocrystals (NCs) that could in principle improve devices' performances and they are well suitable for low cost industrial process. The synthesis of NTO NCs with control over dimensions and both optical and electrical properties is still a challenge[27-29].

Here we present a new colloidal high-yield synthesis of ~9-15nm Nb-doped TiO_2 nanocrystals with control over the Nb content up to ~18%. The inglobation of such a dopant specie lead to the appearance of a tunable broad plasmon peak that ranges from visible to IR region as an effect of the free carriers generated by the substitutional Nb^{5+}. Increasing the amount of Nb precursor the NTO crystals gradually varied their shape from tetragonal to "peanut" like in the case of Nb:Ti=0.2:1. (scheme 1)

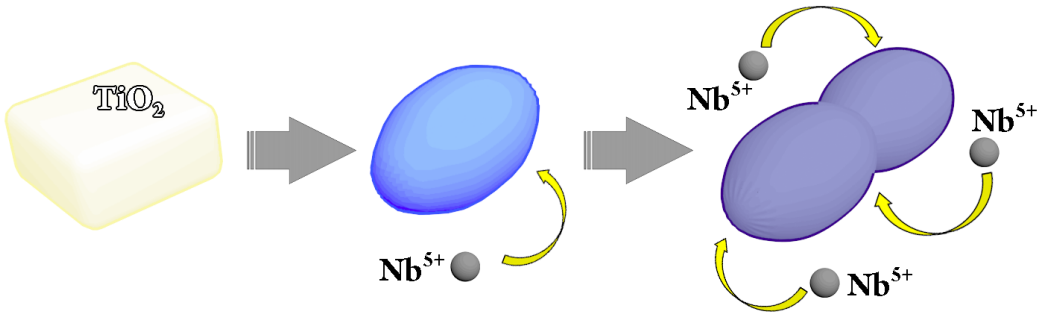

Scheme 8.1 Evolution of Nb-doped TiO_2 NCs. Increasing the ratio of Nb:Ti precursor from 0:1 to 0.2:1 the NCs varied their shape and their optical properties. The colors are indicative of the visible absorption of the samples, and therefore of the coloration of the NCs.

These promising TCO NCs would be ideal for being coupled with InGaN semiconductors to further increase the high efficiency of blue LEDs. The application of such NCs in the *warm white light* project would lead to more efficient final devices. The use of NCs, in fact, can improve the optical properties of the converting + scattering polymer nanocomposite part but also the blue light source of the whole device.

8.2 Synthesis of NTO Nanocrystals

In the synthesis approach we developed[39] a mixture of Octadecanol (ODAL) (13mmol), Oleic Acid (OAc) (1mmol) and Octadecene (ODE) (4ml) was degassed under vacuum at 120 °C for 1 hour in a three-neck flask. A solution of Titanium ethoxide (TEO) (1mmol) and ODE (1ml), previously prepared under inert atmosphere, was then injected in the flask and the temperature was then raised to 290°C for 60 minutes to let the particles grow. The reaction was quenched by cooling the solution to room temperature. The NCs were cleaned by repeated precipitation with acetone and redispersion in hexane for four times. At each cleaning step 100μl of OAc were added to the NCs solution to prevent aggregation. Eventually the NCs were dispersed in 4ml of hexane and 25μl of OAc were necessary to stabilize the colloidal solution. NTO nanocrystals were obtained keeping the amount of all reactants fixed and adding the desired amount of $NbCl_5$ to the solution of TEO and ODE that was injected into the flask. Different samples of NTO were prepared varying systematically the Nb:Ti precursor ratio from 0.025:1 to 0.2:1 (from 2.5% to 20% of Nb precursor). The yield of the proposed synthesis is as high as 75% (~60mg of total product calculated by ICP against the theoretic 79,86 expected).

8.3 Chemical and Structural Characterization of NTO Nanocrystals

XRD and HRTEM confirmed the body-centered tetragonal crystal structure of TiO_2 anatase of all the samples (figure 8.1 and 8.2). In the absence of dopants, 9.6 nm nanocrystals with a tetragonal shape were the only products of the synthesis. Using an alcohol with a shorter chain (Octadecanol instead of OAc) no changes were observed indicating that the alcoholysis isn't the main responsible of the formation of Ti-O-Ti bonds. As it is possible to observe from

the TEM micrographs in figure 8.2, increasing the amount of Nb precursor the aspect ratio of the NTO particles varied elongating systematically along the c axis until reaching a stretched "peanut like" shape.

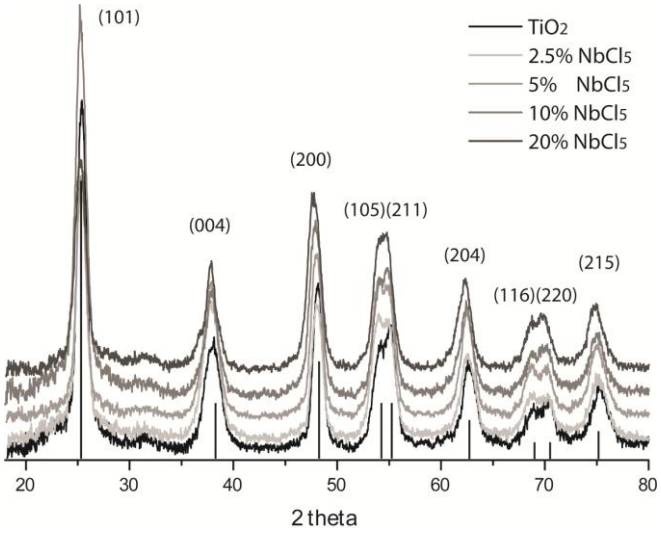

Figure 8.1 XRD patterns of the as-prepared NTO NCs with different Nb loadings. The reference bulk reflections of TiO_2 anatase are shown in the bottom(00-021-1272 JCPD)

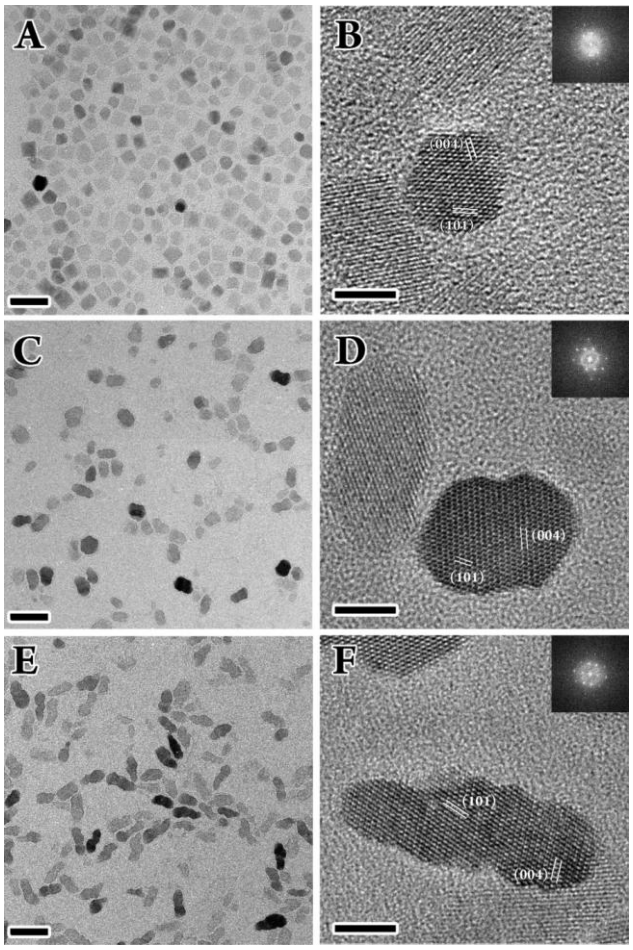

Figure 8.2 Low (left) and high resolution (right) TEM images of NTO nanocrystals with a $NbCl_5$ precursor percentage of 5% (A-B), 10% (C-D) and 20% (E-F). The scalebar of the images A,C and E is 20 nm and 5nm in B,D and F. B) HRTEM image of a "rounded" shaped crystal and it's fast Fourier transformation (FFT) exhibiting the (101) and (004) lattice sets compatible with the body-centered tetragonal structure of TiO_2 anatase and showing measured d-spacing of 3.49 Å and 2.35 Å respectively; D) HRTEM image of a slightly elongated crystal and it's fast Fourier transformation (FFT) exhibiting the (101) and (004) lattice sets compatible with the body-centered tetragonal structure of TiO_2 anatase and showing measured d-spacing of 3.52 Å and 2.40 Å respectively; F) HRTEM image of a "peanut like" shaped crystal and it's fast Fourier transformation (FFT) exhibiting the (101) and (004) lattice sets compatible with the body-centered tetragonal structure of TiO_2 anatase and showing measured d-spacing of 3.54 Å and 2.39 Å respectively.

After an initial shrinking of the nanocrystals made with low amount of Nb precursor (2.5% and 5% of $NbCl_5$) the mean size of the NCs increased up to 15.4 nm as a consequence of the anisotropic shape (table 8.1). A detailed analysis of the XRD patterns collected for the NTO samples confirmed this trend: the FWHM of the peak relative to the lattice plane (004) of TiO_2 anatase lowered systematically with the increase of Nb specie.

% $NbCl_5$	**%Nb in NTO NCs (ICP)[a]**	**%Nb in NTO NCs (XPS)[b]**	**Size (nm)[c]**
0	0	0	9.6 ± 1.6
2.5	3.5	3.4	8.6 ± 1.5
5	5.0	5.3	9 ± 1.4
10	9.6	10.4	11.3 ± 1.6
20	15.9	24.7	15.4 ± 2.4

Table 8.1 The relative amount of precursor used and the composition of the NTO samples are reported with the mean size of the NCs. [a]The amount of Nb in the products was measured by ICP-AES. [b]The amount of Nb and Ti was calculated from XPS hi-res measurements considering the Ti $2p_{3/2}$ and the Nb $3d_{5/2}$ peaks. [c]The mean size of the NCs was estimated from TEM images.

Inductively coupled plasma atomic emission spectroscopy (ICP-AES) confirmed the presence of niobium in all the NTO samples. As a comparison in Mg-doped ZnO[30], AZO[8] and Mn-doped ZnSe [31] NCs the doping efficiency is less than 100% while in ITO NCs [32] it's 100% (like in our synthesis until 10% on Nb precursor)(table 8.1). The inglobation of all the Nb inside the NCs suggests a similar reactivity of $NbCl_5$ and TEO in the synthetic conditions. It is well know that a substitutional Nb^{5+} ion in the TiO_2 anatase structure release on

electron to the conduction band resulting in generation of free carriers and, consequently, in a semiconductor-metal transition of the material[13, 15-17, 20].

8.4 Electro-optical properties of NTO

A first indication of the generation of free carriers inside the Nb-doped TiO_2 NCs can be found looking at the UV-VIS-IR absorption spectra of the NTO samples (figure 8.3). A broad absorption peak ranging from visible region and having a maximum in the IR region appears in the doped sample. Moreover it increases in intensity (figure 8.3a) an moves to higher energies (fig 8.3b) together with the dopant amount strongly indicating that the NTO NCs show a surface localized plasmon peak.

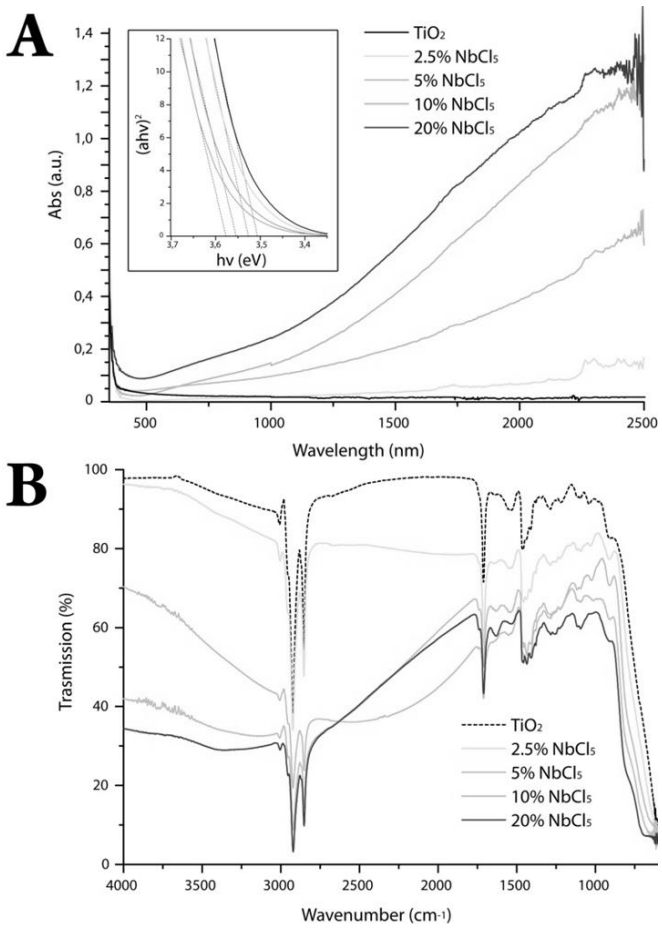

Figure 8.3 Optical properties of the NTO NCs. A) UV-VIS-NIR absorption curves of equimolar solutions of NCs in in tetrachloroethylene (TCE). The weak peaks appearing above 1600nm are due to the oleic acid necessary to stabilize the colloidal solutions. In the inset $(\alpha h\nu)^2$- $h\nu$ plots for different NTO samples are shown. The value of the optical band gap (E_{gOPT}) can be derived from the extrapolation to α=0. B) FTIR-ATR spectra of the corresponding dropcasted NTO solutions.

The optical bandgap (E_{gOPT}), which was evaluated by the $(\alpha h\nu)^2$- $h\nu$ plots of the UV-absorption edge for the NTO NCs systematically increased with the amount of Nb content (figure 8.3a). The Burstein-Moss shift that is due to conduction band filling by carrier electrons, is clearly seen in NTO samples, suggesting that doped Nb^{5+} ions act as the dopant as already observed by others[15, 16, 18]. The EPR spectrum of TiO_2 (figure 8.4) showed just the weak cavity background signal (g ~2.05) and a weak, sharp signal at g ~ 2.0, possibly due to a deep trap[33]. Upon addition of niobium, an intense new axial signal appeared with $g|| \sim 1.94$, $g\perp \sim 1.96$ that is consistent with the formation of substitutional Ti^{3+}[29, 34]. There was no evidence in EPR spectra of Nb^{4+}, which would be expected at g ~ 1.97[35]. Additionally, there was no evidence of the interstitial Ti^{3+} species frequently reported for reduced TiO_2[29, 34].

With increasing niobium concentration, the Ti^{3+} signal increases and broadens (Figure 8.4a), as expected for increasing numbers of extra electrons in the nanocrystals. At very high niobium concentrations the Ti^{3+} signal is broad and poorly resolved. The deep-trap signal at g=2 is still observed at all niobium concentrations. EPR analyses confirmed the effective doping of TiO_2 systems with Nb^{5+} occupying Ti^{4+} sites and giving extra electrons to the final structure.

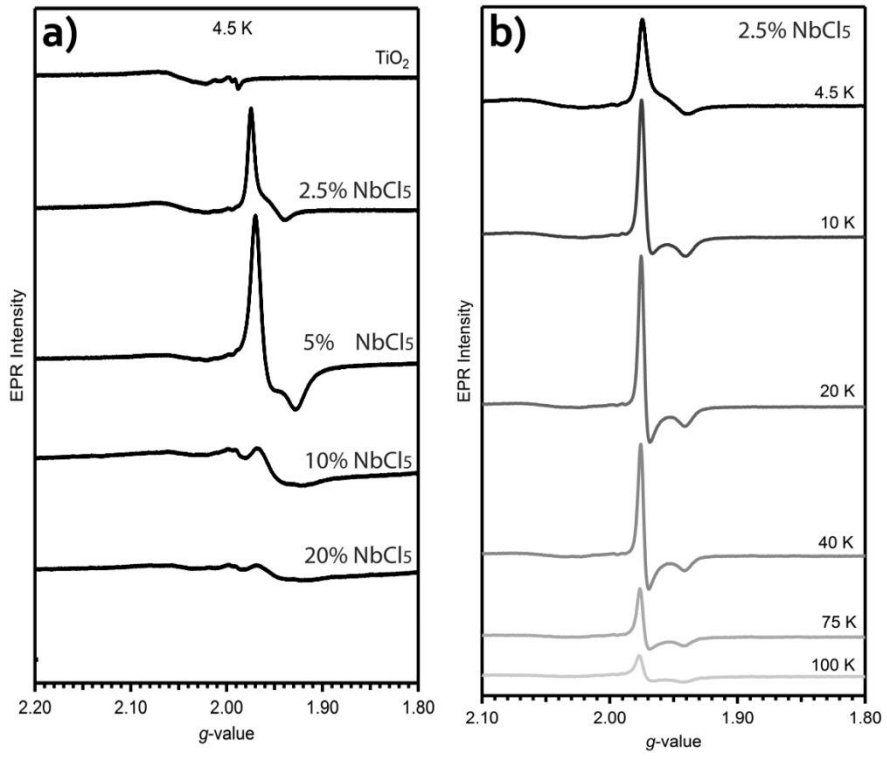

Figure 8.4 a) 4.5K EPR spectra of NTO nanocrystals obtained with different amount of Nb precursor. b) Variable-temperature EPR spectra of NTO NCs made with 2.5% of $NbCl_5$.

For a fixed niobium concentration, increasing the temperature caused a small change in relative peak intensities and a rapid decrease in total intensity (Figure 8.4b). The Ti^{3+} signal is not observed above ~100K (depending on niobium concentration). These data suggest either rapid relaxation of Ti^{3+} at elevated temperatures or signal broadening due to carrier de-trapping.

8.5 Limit of niobium doping

Trying to increase the amount of free carriers, further $NbCl_5$ (30%) was used in the synthesis of NTO NCs. No variations were observed in the optical properties varying the % of $NbCl_5$ precursor ratio from 20 to 30% while the amount of Nb atoms detected by ICP was found to increase. XPS analysis in the regions of the Ti $2p_{3/2}$ and Nb $3d_{5/2}$ peaks were carried to have a better comprehension of the NTO systems. The spectra of the Ti and Nb species were in both cases simple spin-orbit doublets with a Ti $2p_{3/2}$ binding energy of 459.6±0.2 eV and a Nb $3d_{5/2}$ binding energy of 207.9±0.2 eV. In all the samples the Ti and Nb peaks didn't show any shoulder at lower energy, normally related to Ti^{3+} and Nb^{4+} species[36]. Another important information came from the quantitative analysis of the Nb and Ti peaks. For amount of $NbCl_5$ as high as 10% the compositions of the products measured by ICP and XPS matched while for higher amount a higher concentration of Nb was found outside(/on the surface) of the NTO NCs (see table 8.1).

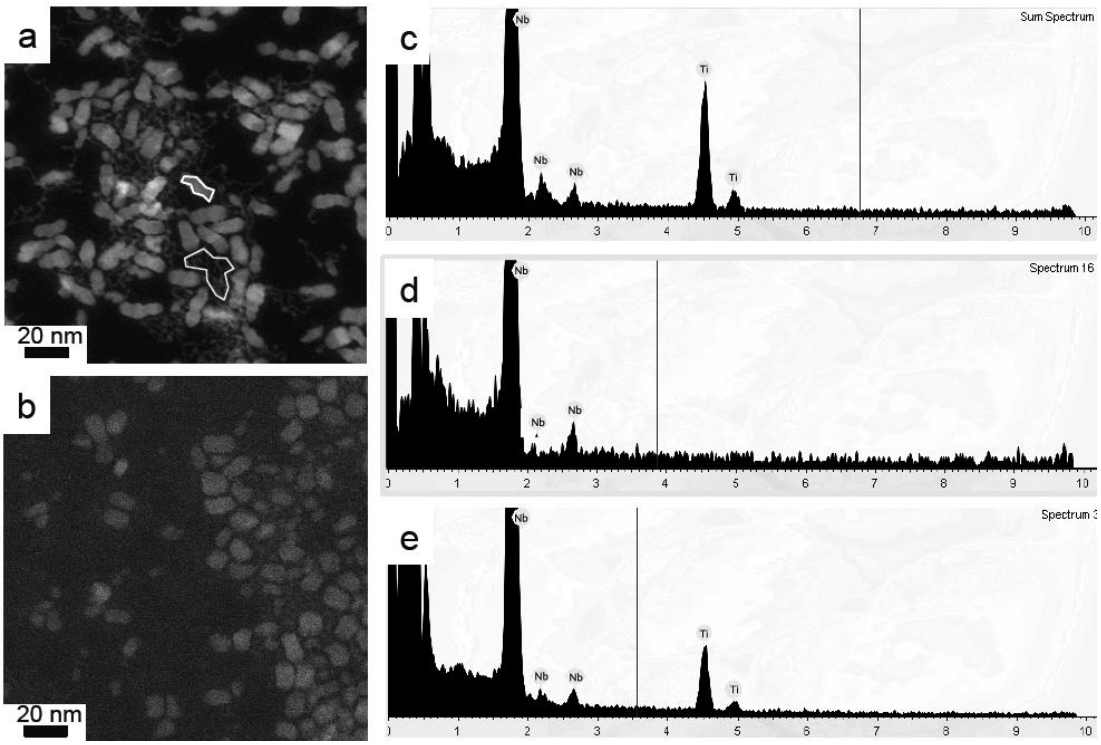

Figure 8.5 HAADF-STEM images of NTO samples obtained using 20%(a) and 10%(b) of $NbCl_5$. In figure (c-e) different areas of the figure (a) were analyzed through STEM-EDS mapping: EDS spectum of the whole area (c), of the amorphous inorganic network outside of the particles (d) and of a single nanoparticle (e).

This "extra" Nb was in fact present in the form of amorphous Nb_xO_y (and so, not detectable by XRD) around the NCs as we could see through elemental mapping EDS in High Angle Annular Dark Field - Scanning Transmission Electron Microscopy (HAADF-STEM) mode (figure 8.5). In the STEM images it was possible to visualize a sort of inorganic network outside of the NCs lacking in Ti and containing just Nb (figure 8.5d). Performing a statistical analysis and looking at the Nb specifically inside each NC, it was clear that there was a NC to NC variation. As a result of this "statistical" analysis the percentage of Nb in the sample obtained using 10% of $NbCl_5$ was 7±5% and for the one obtained using 20% of NbCl5 we calculated 14±12%.

A further proof of the presence of amorphous niobium oxide is given by Raman spectroscopy. As it is possible to appreciate from the collected spectra (figure 8.7) a very broad and weak peak is visible at ~850cm^{-1} in the samples obtained with concentration of $NbCl_5$ higher than 10%.

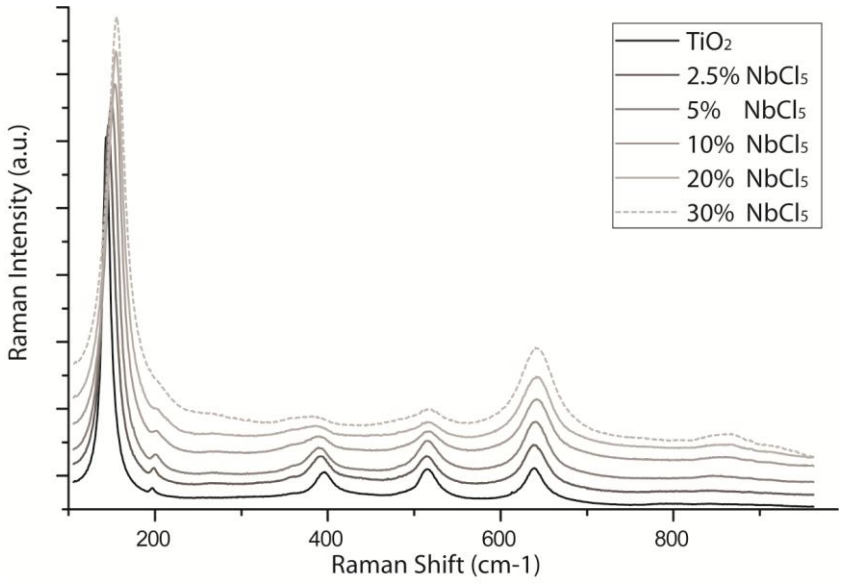

Figure 8.6 Raman spectra of NTO nanocrystals deposited on a quarz substrate.

This peak is related to the vibration mode of the Nb=O bond normally present as network termination in amorphous Nb_xO_y[37, 38]. Moreover the insertion of substitutional Nb^{5+} ions inside the TiO_2 anase lattice structure is reinforced by Raman spectroscopy. The anatase raman peak at 144cm^{-1} broadens and shifts to higher energies as a consequence of the formation of Nb-O-Ti bonds and at the same time the anatase peak at 639cm^{-1} broadens and gets more intense due to the formation of Nb-O bonds (fig 4b). Interestingly no peaks at 235cm^{-1} and 449cm^{-1} of rutile phase are observed confirming, in parallel with XRD and HRTEM analysis, that no rutile phase occurred increasing the Nb doping content on the contrary of what observed by Arbiol et al.[27].

Further experimens were performed trying to understand the kinetics of the synthesis. Lowering the reaction temperature from 290°C to 260°C smaller NTO NCs were obtained. Interestingly also in this case the amount of Nb used for the reaction matched with the amount calculated by ICP on the final samples. Considering that at same amount of $NbCl_5$ lower intensities of Plasmon peak are observed for the samples prepared at 260°C. We can state that at this temperature a worse matching of the precursors reactivities is achieved leading to a less incorporation of Nb inside the particles. Lowering the reactivity of the titanium precursor, using Titanium isopropoxide instead of TEO, led to extremely similar results.

8.6 Conclusions

We developed a new colloidal synthesis of TiO_2 anatase nanocrystals with a tetragonal shape and 10nm size. The synthesis was optimized for the incorporation of Nb dopants up to a Nb percentage of ~18%. The effect of the doping was the generation of free carriers inside the conduction band of the TiO_2 anatase host matrix leading to a tunable surface localized Plasmon peak with its maximum in the IR region. At the same time the filling of the CB with free electrons is proved by the blue shift of the absorption edge in the UV region as a consequence of the Burstein-Moss effect. Working with percentage of $NbCl_5$ ≥20% NTO NCs were produced in presence of Nb_xO_y species that have been successfully detected through HAADF-STEM and Raman spectroscopy. The formation of these species competes with the effective doping process limiting the percentage of Nb inside the TiO_2 NCs.

The undoped TiO_2 nanocrystals (obtainable with a reaction yield of 75%), will be used as inorganic scatterers inside the bulk PMMA polymer sheet for diffusing the blue LED in the final device of the *warm white light* project. On the other hand the NTO nanocrystals could in principle improve the efficiency of modern blue LEDs if used as TCO replacing ITO or AZO due to a better refractive index matching with the emitting InGaN. Therefore, the next step of our project would be the application of these NCs in blue LEDs.

8.7 References

[1] Calnan, S. and A.N. Tiwari, High mobility transparent conducting oxides for thin film solar cells. *Thin Solid Films*, **2010**. 518(7): p. 1839-1849.

[2] Minami, T., Transparent conducting oxide semiconductors for transparent electrodes. *Semiconductor Science and Technology*, **2005**. 20(4): p. S35.

[3] Fortunato, E., et al., Transparent Conducting Oxides for Photovoltaics. *MRS Bulletin*, **2007**. 32(03): p. 242-247.

[4] Ginley, D.S. and C. Bright, Transparent Conducting Oxides. *MRS Bulletin*, **2000**. 25(08): p. 15-18.

[5] Fortunato, E., et al., Highly stable transparent and conducting gallium-doped zinc oxide thin films for photovoltaic applications. *Solar Energy Materials and Solar Cells*, **2008**. 92(12): p. 1605-1610.

[6] Garcia, G., et al., Dynamically Modulating the Surface Plasmon Resonance of Doped Semiconductor Nanocrystals. *Nano Letters*, **2011**. 11(10): p. 4415-4420.

[7] Jiang, X., et al., Aluminum-doped zinc oxide films as transparent conductive electrode for organic light-emitting devices. *Applied Physics Letters*, **2003**. 83(9): p. 1875-1877.

[8] Buonsanti, R., et al., Tunable Infrared Absorption and Visible Transparency of Colloidal Aluminum-Doped Zinc Oxide Nanocrystals. *Nano Letters*, **2011**. 11(11): p. 4706-4710.

[9] Pimputkar, S., et al., Prospects for LED lighting. *Nat Photon*, **2009**. 3(4): p. 180-182.

[10] Hitosugi, T., et al., Electronic Band Structure of Transparent Conductor: Nb-Doped Anatase TiO2. *Applied Physics Express*, **2008**. p. 111203.

[11] Kasai, J., et al., Properties of TiO_2-based transparent conducting oxide thin films on GaN(0001) surfaces. *Journal of Applied Physics*, **2010**. 107(5): p. 053110.

[12] Tasaki, C., et al., Thermophysical Properties of Transparent Conductive Nb-Doped TiO2 Films. J*apanese Journal of Applied Physics*, **2012**. 51, p. 035802.

[13] Hitosugi, T., et al., Properties of TiO2-based transparent conducting oxides. *physica status solidi A*, **2010**. 207(7): p. 1529-1537.

[14] Lee, S., et al., Nb-Doped TiO2: A New Compact Layer Material for TiO2 Dye-Sensitized Solar Cells. *The Journal of Physical Chemistry C*, **2009**. 113(16): p. 6878-6882.

[15] Kurita, D., et al., Carrier generation and transport properties of heavily Nb-doped anatase TiO2 epitaxial films at high temperatures. *Journal of Applied Physics*, **2006**. 100(9): p. 096105.

[16] Kaleji, B.K., R. Sarraf-Mamoory, and A. Fujishima, Influence of Nb dopant on the structural and optical properties of nanocrystalline TiO2 thin films. *Materials Chemistry and Physics*, **2012**. 132(1): p. 210-215.

[17] Furubayashi, Y., et al., A transparent metal: Nb-doped anatase TiO2. *Applied Physics Letters*, **2005**. 86(25): p. 252101.

[18] Zhang, S.X., et al., Niobium doped TiO2: Intrinsic transparent metallic anatase versus highly resistive rutile phase. *Journal of Applied Physics*, **2007**. 102(1): p. 013701.

[19] Kamisaka, H., et al., Density functional theory based first-principle calculation of Nb-doped anatase TiO2 and its interactions with oxygen vacancies and interstitial oxygen. *The Journal of Chemical Physics*, **2009**. 131(3): p. 034702.

[20] Liu, Y., et al., Niobium-Doped Titania Nanoparticles: Synthesis and Assembly into Mesoporous Films and Electrical Conductivity. *ACS Nano*, **2010**. 4(9): p. 5373-5381.

[21] Furubayashi, Y., et al., Transport properties of d-electron-based transparent conducting oxide: Anatase Ti1-xNbxO2. *Journal of Applied Physics*, **2007**. 101(9): p. 093705.

[22] Tonooka, K., T.-W. Chiu, and N. Kikuchi, Preparation of transparent conductive TiO2:Nb thin films by pulsed laser deposition. *Applied Surface Science*, **2009**. 255(24): p. 9695-9698.

[23] Bae, H., et al., Effect of niobium doping on the optical and electrical properties in titanium dioxide grown by pulsed laser deposition. *Journal of Vacuum Science & Technology B: Microelectronics and Nanometer Structures*, **2012**. 30(5): p. 050603.

[24] Hoang, N.L.H., et al., Low-temperature Fabrication of Transparent Conducting Anatase Nb-doped TiO2 Films by Sputtering. *Applied Physics Express*, **2008**. 1, p. 115001.

[25] Sato, Y., et al., Transparent conductive Nb-doped TiO2 films deposited by direct-current magnetron sputtering using a TiO2 target. *Thin Solid Films*, **2008**. 516(17): p. 5758-5762.

[26] Yamada, N., et al., Direct growth of transparent conducting Nb-doped anatase TiO2 polycrystalline films on glass. *Journal of Applied Physics*, **2009**. 105(12): p. 123702-6.

[27] Arbiol, J., et al., Effects of Nb doping on the TiO2 anatase-to-rutile phase transition. *Journal of Applied Physics*, **2002**. 92(2): p. 853-861.

[28] Štengl, V., et al., Niobium and tantalum doped titania particles. *Journal of Materials Research*, **2010**. 25(10): p. 2015-2024.

[29] Hirano, M. and Y. Ichihashi, Phase transformation and precipitation behavior of niobium component out of niobium-doped anatase-type TiO2 nanoparticles synthesized via hydrothermal crystallization. *Journal of Materials Science,* **2009**. 44(22): p. 6135-6143.

[30] Yang, Y., et al., Dopant-Induced Shape Evolution of Colloidal Nanocrystals: The Case of Zinc Oxide. *Journal of the American Chemical Society*, **2010**. 132(38): p. 13381-13394.

[31] Erwin, S.C., et al., Doping semiconductor nanocrystals. *Nature*, **2005**. 436(7047): p. 91-94.

[32] Choi, S.-I., et al., Preparation and Optical Properties of Colloidal, Monodisperse, and Highly Crystalline ITO Nanoparticles. *Chemistry of Materials*, **2008**. 20(8): p. 2609-2611.

[33] Fittipaldi, M., et al., A Multifrequency EPR Study on Organic-Capped Anatase TiO2 Nanocrystals. *The Journal of Physical Chemistry C*, **2009**. 113(15): p. 6221-6226.

[34] Howe, R.F. and M. Gratzel, EPR observation of trapped electrons in colloidal titanium dioxide. *The Journal of Physical Chemistry*, **1985**. 89(21): p. 4495-4499.

[35] Kiwi, J., J.T. Suss, and S. Szapiro, EPR spectra of niobium-doped TiO2 and imiplications for water photocleavage processes. *Chemical Physics Letters*, **1984**. 106(1–2): p. 135-138.

[36] Morris, D., et al., Photoemission and STM study of the electronic structure of Nb-doped TiO2. *Physical Review B*, **2000**. 61(20): p. 13445-13457.

[37] Orel, B., et al., In situ UV-Vis and ex situ IR spectroelectrochemical investigations of amorphous and crystalline electrochromic Nb205 films in charged/discharged states. *Journal of Solid State Electrochemistry*, **1998**. 2(4): p. 221.

[38] Pittman, R.M. and A.T. Bell, Chem Inform Abstract: Raman Studies of the Structure of Nb2O5/TiO2. *ChemInform*, **1994**. 25(9)

[39] Luca De Trizio et al., Nb-Doped Colloidal TiO2 Nanocrystals with a Tunable Localized Surface Plasmon Resonance, paper under construction, to be submitted.

Conclusions

The aim this PhD project, also called *warm white light* project, is to create a lighting device that could work as a transparent glass in off-mode and as a "lamp" in on-mode. To do so, a blue LED, made of Indium gallium nitride (InGaN) (the source of light), is coupled to a bulk polymer nanocomposite sheet where conversion and diffusion of the blue light take place. In vision of a low cost, non-toxic and highly efficient device, I worked on the development of the synthesis of all the necessary elements.

InP/ZnS Core-Shell QDs were synthesized following the "amines assisted" route that allowed for the production of yellow and orange emitting QDs with a QY as high as 50%. Unfortunately these systems were shown to be quiete weak and they couldn't sustain a bulk polymerization process. An alternative strategy for the synthesis of InP NCs was explored. At first we prepared Cu_3P nanoparticles within the 5-50 nm range. Then we tried to transform these NCs into InP through cation exchange reactions between Cu^+ and In^{3+} ions. Unfortunately no cation exchange was achieved.

We then set up a two-step synthesis that allowed the production of highly fluorescent CIZS NCs reaching a QY up to 80%. In the first step we obtained Cu-deficient CIS NCs by varying the initial relative amount of copper precursor. A partial cation exchange with Zn^{2+} led to the formation of quaternary Cu-In-Zn-S QDs. TEM, ICP and XPS analysis indicated that our procedure allowed for a good control over the stoichiometry of the quaternary CIZS NCs that would be

probably hard to achieve otherwise. The formation of CIZS NCs resulted into a blue shift of both the PL and absorption and the disappearance of the short time decay components in time-resolved PL. This leaded to more efficient systems which shown enhanced PL QY. These QDs were successfully encapsulated in bulk PMMA matrix through bulk polymerization. Bulk polymer nanocomposites with strong fluorescence were shown to be easily obtainable under inert atmosphere. The resulting systems are potentially extremely useful for the *warm white light* project and they are now under study.

Finally, we developed a new colloidal synthesis of TiO_2 anatase NCs with a tetragonal shape and 10nm size. The synthesis was optimized for the incorporation of Nb dopants up to a Nb percentage of ~18%. The effect of the doping was the generation of free carriers inside the conduction band of the TiO_2 anatase host matrix leading to a tunable surface localized Plasmon peak with its maximum in the IR region. The TiO_2 NCs will be used as inorganic scatterers inside the bulk PMMA polymer sheet for diffusing the blue LED. Nb-doped TiO_2 nanocrystals, used as a TCO electrode, in the blue LED source could theoretically improve the efficiency of the device.

In conclusion several new syntheses of "new" nanocrystals with different properties were developed to fulfil all the prerequisites for the production of a modern solid state lighting device. A PMMA-TiO_2-CIZS nanocomposite will form the "core" of this new device, while NTO NCs would lead to more efficient blue LED sources (see figure 9.1)

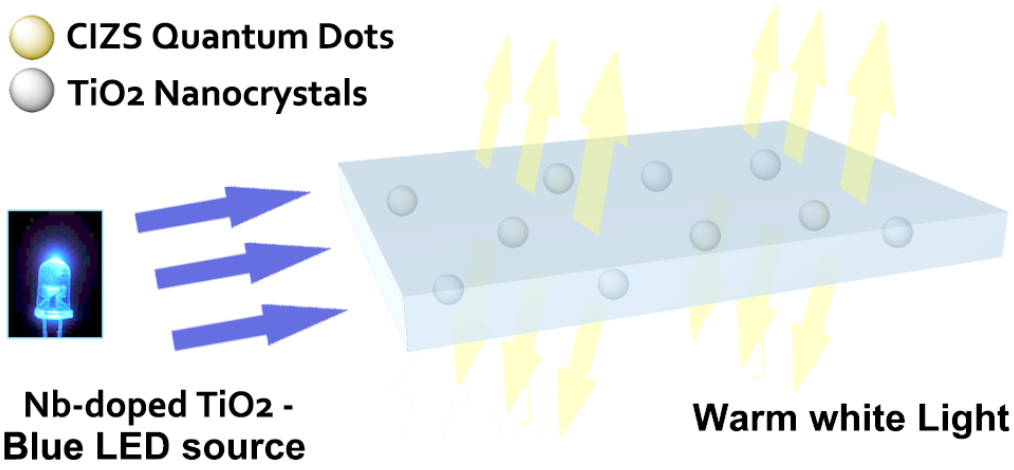

Figure 9.1 Sketch of the final lighting device realizable with the NCs developed in this work. A blue LED made of InGaN+NTO NCs would be used as light source. The light would be partially diffused by TiO2 NCs and partially converted by the CIZS QDs present in bulk polymer nanocomposite, resulting in a warm white light. In off mode the device appears as a transparent polymer.

Acknowledgement

At the end of this beautiful work I would like to thank all those people who helped me to become the scientist that I am (or that I pretend to be). These people made this project possible and an unforgettable experience for my life.

At first I pay homage to my supervisor, Dr. Roberto Simonutti that gave me the possibility of working in his group and for offering me the chance of developing such an interesting project. I am extremely grateful to Liberato Manna, Director of the Nanochemistry Department, Italian Institute of Technology (IIT), Genova, Italy. Thanks to him I could start exploring a new scientific world that is still so fascinating to me. I'm also really grateful for all friendly people I had the possibility to work with at the IIT. Special thanks go to Albert Figuerola who was the first person who shared with me his experience on the colloidal synthesis of nanocrystals. Probably my work wouldn't have been so exciting without them. Eventually I would like to thank Delia Milliron, Director of the Inorganic Nanostructures Facility, LBNL, Berkeley, California for giving me the opportunity of expanding my scientific boundaries. Even if for a short time, working in her nice group it was a very interesting experience. As regarding my American experience I'm extremely grateful to Raffaella Buonsanti who has always been a point of reference as no one else in Berkeley.

Special Acknowledgements

My special acknowledgments are addressed to all those people who make me feel alive and give me the strength for enjoying my life.

First and foremost I offer my gratitude to my family who have always trusted in me. My innermost expression of appreciation goes to my parents who have always loved and supported me, giving me the opportunity of becoming what I am. I would like to thank my brother for always enjoying my stay in Bergamo with him and for being there when I we need him. Special thanks go to my grandma Clara who, despite her age, is always caring about me. Last but not least I give thanks to my relatives in Roma that, even if mostly far from me, are always in my mind.

I would like to express my deepest gratitude to Eleonora who became an inseparable mate of my life. A big part of my enthusiasm and vitality comes from her warmth and joy.

My sincere thanks also goes to my friends in Bergamo that, after so many amazing experiences, are almost a second family to me. I hope we'll always have much fun together. I express my sincerest gratitude also to all my work friends and climbing friends in Genova that are making my present life full of wonderful emotions.